MINISTRY OF EDUCATION AND SCIENCE OF UKRAINE

KYIV NATIONAL UNIVERSITY OF TECHNOLOGIES AND DESIGN

Faculty of Chemical and Biopharmaceutical Technologies

Department of Pharmaceutical Industry

Master's thesis

on the topic **Prospects for the application of advanced oxidation technology in the treatment of pharmaceutical wastewaters**

Completed: student of the group <u>MPhch-20</u>

of the speciality <u>226 Pharmacy, industrial pharmacy</u>
<div style="text-align:center">(code and name of the specialty)</div>

<u>Chi ZHILONG</u>
<div style="text-align:center">(first name, last name)</div>

Supervisor <u>Olena SALIY</u>
<u>Jianjun Song</u>
<div style="text-align:center">(first name, last name)</div>

Reviewer <u>Olha BAULA</u>
<div style="text-align:center">(first name, last name)</div>

Kyiv 2021

KYIV NATIONAL UNIVERSITY OF TECHNOLOGIES AND DESIGN

Institute, faculty.   Chemical and Biopharmaceutical Technologies
Department   Industrial Pharmacy
Speciality   226 Pharmacy, industrial pharmacy
<div align="center">(code and title)</div>

<div align="right">

Approve

Head of Department Industrial Pharmacy,
Professor, Doctor of Pharmaceutical Science
Vladyslav STRASHNYI

_____

"14" December 2021

</div>

ASSIGNMENTS

FOR THE MASTER'S THESIS

<div align="center">

Chi Zhilong
(Full Name)

</div>

1. Thesis topic Prospects for the application of advanced oxidation technology in the treatment of pharmaceutical wastewaters   .

2. Scientific supervisor   Olena Saliy, Associate Professor, PhD
<div align="center">(first name, last name, patronymic, academic degree, academic title)</div>
approved by the order of the higher educational institution on 4th October 2021, N 286

3. Deadline for student submission of work 14th December 2021

4. Initial data for work: scientific and information sources, methodological and technological literature, scientific periodicals, international and domestic regulations and standards for the development and production of medicines

5. Content of the thesis (list of questions to be developed). *A review of the literature on removal method of pharmaceutical wastewater, the development and preparation process of catalyst, the study and detection of active species, catalytic performance of different catalysts,   characterization results*

6. Consultants of the master's thesis sections

Section	Surname, initials and position of the consultant	Signature	
		the task was issued	the task accepted
Section 1	Olena Saliy, Associate Professor, PhD	*[signature]*	*[signature]*
Section 2	Jianjun Song, Associate Professor, PhD	宋建军	宋建军
Section 3	Jianjun Song, Associate Professor, PhD	宋建军	宋建军
Section 4	Olena Saliy, Associate Professor, PhD	*[signature]*	*[signature]*

7. Date of issue of the assignment   September 20, 2021

Execution schedule

No	The name of the stages of the master's thesis	Terms of performance of stages	Note on performance
1	Introduction	20.09 –27.09.2021	*[signature]* 迟志龙
2	Section 1 *Preface*	28.09. – 11.10.2021	*[signature]* 迟志龙
3	Section 2 *The experimental method Preparation process of catalyst*	12.10 – 25.10.2021	*[signature]* 迟志龙
4	Section 3 *Catalytic performance of different catalysts*	26.10 - 08.11.2021	*[signature]* 迟志龙
5	Section 4 Conclusions	09.11.-15.11.2021	*[signature]* 迟志龙
6	Draw up a master's thesis (*final version*)	16.11.-04.12.2021	*[signature]* 迟志龙
7	Submission of master's thesis to the department for review (*14 days before the defence*)	06.12.-14.12.2021	*[signature]* 迟志龙
8	Checking the master's thesis for signs of plagiarism (*10 days before the defence*)	14.12-18.12.2021	宋建军、迟志龙
9	Submission of master's thesis to the master's department to check the implementation of the appendix to the individual curriculum (*10 days before the defence*)	16.12-18.12.2021	宋建军 迟志龙
10	Submission of master's thesis for approval by the head of the department (*from 7 days before the defence*)	18.12-21.12.2021	*[signature]* 迟志龙

Student _____迟志龙_____ Chi Zhilong
<small>(first name, last name)</small>

Scientific supervisor _____*[signature]*_____ Olena Saliy
<small>(first name. last names)</small>

Head of the scientific and methodological center
for the management of specialist training _____ Olena HRYHOREVSKA
<small>(first name and second)</small>

SUMMARY

Chi Zhilong. Prospects for the application of advanced oxidation technology in the treatment of pharmaceutical wastewaters.

Master's thesis in the specialty 226 Pharmacy, industrial pharmacy - Kyiv National University of Technologies and Design, Kyiv, 2021.

Advanced Oxidation Technology based on persulfate activation is an important part of advanced oxidation technology for water treatment, in which catalyst plays a very important role. In this master's thesis, $LaCoO_3/g-C_3N_4$ catalyst was prepared by hydrothermal method and the catalytic degradation efficiency of $LaCoO3/g-C_3N_4$ catalyst for pharmaceutical wastewater was investigated, and the relationship between catalyst structure and degradation efficiency in catalytic activation of PMS was discussed. Based on the study of catalytic activated PMS oxidative degradation kinetic characteristics, investigation of reaction influencing factors and analysis of reaction mechanism, the synergistic enhancement effect and practical application value of various $LaCoO_3/g-C_3N_4$ catalysts for PMS oxidation were discussed.

The catalyst was characterized by XRD, XPS, FTIR, Raman and BET. Tetracycline hydrochloride was used as a typical and targeted contaminant in pharmaceutical wastewater, and the degradation performance of tetracycline hydrochloride by PMS activation of different catalysts was investigated. At the same time, the effects of different reaction conditions (PMS concentration, TC concentration, reaction temperature, pH, etc.) on the TC degradation performance of $LaCoO_3/g-C_3N_4$ catalyst were studied.

Keywords: *PMS activation; Pharmaceutical wastewater; Tetracycline hydrochloride; $LaCoO_3$; g- C_3N_4*

АНОТАЦІЯ

Чі Чжилонг. Перспективи застосування передової технології окислення при очищенні фармацевтичних стічних вод.

Магістерська робота за спеціальністю 226 Фармація, промислова фармація –

Київський національний університет технологій та дизайну, Київ, 2021.

Удосконалена технологія окислення, заснована на персульфатній активації, є важливою частиною передової технології окислення для обробки води, в якій важливу роль відіграє каталізатор. У цій магістерській дисертації каталізатор $LaCoO_3/g\text{-}C_3N_4$ було виготовлено гідротермальним методом та досліджено ефективність каталітичної деградації каталізатора $LaCoO_3/g\text{-}C_3N_4$ для фармацевтичних стічних вод, а також обговорено взаємозв'язок між структурою каталізатора та ефективністю деградації при каталітичній активації PMS. На підставі вивчення кінетичних характеристик окислювальної деградації каталітично активованого ПМС, дослідження факторів впливу на реакцію та аналізу механізму реакції, обговорено синергетичний ефект посилення та практичне застосування різних каталізаторів $LaCoO_3/g\text{-} C_3N_4$ для окислення ПМС.

Каталізатор був охарактеризований XRD, XPS, FTIR, Raman і BET методами. Тетрацикліну гідрохлорид застосували як типовий та цільовий забруднювач фармацевтичних стічних вод, та було досліджено ефективність деградації тетрацикліну гідрохлориду за допомогою PMS-активації різних каталізаторів. Водночас досліджено вплив різних умов реакції (концентрація ПМС, концентрація ТК, температура реакції, pH тощо) на ефективність деградації ТС каталізатора $LaCoO_3/г\text{-}C3N4$.

Ключові слова: *активація ПМС; Фармацевтичні стічні води; тетрацикліну гідрохлорид; $LaCoO_3$; $g\text{-}C_3N_4$*

Contents

Lists of abbreviations and symbols

SBR- sequencing batch reactor activated sludge process

AAO- Anaerobic-Anoxic-Oxic

AOPs - Advanced oxidation processes

ORR － Oxygen Reduction Reaction

OER － Oxygen Reduction Reaction

TOC- Total Organic Carbon

COD － Chemical Oxygen Demand

FT-IR － Fourier transform infrared spectroscopy

BET － Brunauer–Emmett–Teller

BJH － Barret-Joyner-Halenda

PMS － Peroxymonosulfate

XRD － X-Ray Diffraction

XPS － X-ray photoelectron spectroscopy

EPR － Electron Paramagnetic Resonance

TEMP － 4-amino-2,2,6,6-tetramethylpiperidine

DMPO － 5,5-dimethyl-1-pyrroline-n-oxide

TC － Tetracycline hydrochloride

Introduction

The **relevance of the topic**. With the globalization of economic development and the continuous improvement of people's health requirements, and the variation of COVID-19 has greatly delayed the controlled time of the global epidemic. At presence, people have put forward higher requirements for the rapid development of the pharmaceutical industry, which includes the demand for fast and efficient product introduction of new pharmaceutical products. It also includes the treatment of three wastes in the process of pharmaceutical production to meet the environmental needs. In the treatment of three wastes (wastewater, waste gas and waste residue) in the pharmaceutical industry, wastewater treatment is an important aspect of environmental treatment.

The pharmaceutical industry, especially the chemical synthetic pharmaceutical industry, has the characteristics of many auxiliary materials, complex production processes, large amount of three wastes and low yield. These characteristics lead to complex composition and huge discharge of pharmaceutical wastewater. These wastewater contain toxic and harmful intermediates and by-products produced in the pharmaceutical process, as well as many pollutants such as biological inhibitors, organic solvents, sulfides and heavy metal ions. These pollutants are highly toxic and difficult to be degraded under general conditions. Therefore, this kind of wastewater will cause serious negative consequences to the ecological environment stability and safety of the receiving water body.

Research shows that even low concentration wastewater downstream of pharmaceutical wastewater production source will still have adverse physiological and

biochemical effects on wildlife in water. Firstly, a large part of the pollutants discharged into the receiving water body have strong toxicity. And it also makes the endocrine system of animals and plants in the water disordered. This will lead to the poisoning of animals and plants in the water, and then reduce the population density and even decline; Secondly, after the pharmaceutical wastewater is discharged into the water body, the organic pollutants contained in it will consume a large amount of dissolved oxygen during decomposition, resulting in the anoxic mass death of aerobic animals, plants and microorganisms in the water body. At the same time, a large number of anaerobic microorganisms in the water body will proliferate, making the self purification function of the water body invalid, resulting in the stench of the water body; Finally, because many pharmaceutical products and intermediates in the synthesis process have a certain broad-spectrum bactericidal effect, the wastewater containing these antibacterial compounds will inhibit the metabolic activities of algae and other microorganisms in the receiving water body, and then destroy the ecological balance in the water body.

The composition of pharmaceutical wastewater is complex due to the complex synthetic route of pharmaceutical products and the wide range of raw materials and auxiliary materials. At the same time, antibiotics have great inhibitory and toxic effects on microorganisms, which makes the wastewater difficult to be biologically degraded. In addition, due to the different technical routes in the drug synthesis process, there are obvious differences in the raw materials and production processes used, the water quality and quantity of pharmaceutical wastewater are also extremely unstable, and there are many kinds of organic substances, which aggravates the harm to the environment.

Medical wastewater can be divided into the following categories according to the

source of wastewater: 1) Process drainage during production; 2) Common works drainage; 3) Washing water converted from cleaning to production; 4) Domestic sewage in pharmaceutical production plant.

Pharmaceutical wastewater is different from other wastewater in: (1) complex composition; (2) Large concentration range; (3) high component toxicity . Therefore, the research and application of effective treatment technology of pharmaceutical wastewater has become one of the key and difficult points for environmental workers. Most of the traditional methods for treating organic matter in pharmaceutical wastewater are physicochemical precipitation method, chemical oxidation method, biological oxidation method and other oxidation methods.

To sum up, most of the processes for treating pharmaceutical wastewater have some problems, such as incomplete treatment, secondary pollution and high treatment cost. It is urgent to study an efficient and low-cost advanced oxidation technology to treat the wastewater containing refractory organics in the process of pharmaceutical production.

The **purpose of the study** is: Development of $LaCoO_3$/g-C3N4 catalyst by hydrothermal method, study of the efficiency of catalytic decomposition of LaCoO3/ g-C3N4 catalyst for pharmaceutical wastewater, and study of the efficiency of decomposition of tetracycline hydrochloride as a typical and target pollutant of pharmaceutical wastewater.

The **research objectives of the study:**

- to develop a process and prepare a catalyst;

- to evaluate the efficiency of catalytic decomposition of $LaCoO_3$/g-C_3N_4 catalyst for pharmaceutical wastewater treatment;

- to characterize the Catalyst using XRD, XPS, FTIR, Raman and BET methods;

- to investigate the efficiency of decomposition of tetracycline hydrochloride upon PMS activation of various catalysts.

The **object of MTh** is $LaCoO_3$ / $g-C_3N_4$ catalyst for pharmaceutical wastewater treatment.

The **subject of MTh** is the process of preparing the catalyst, evaluating its structure and the efficiency of the catalytic decomposition of the $LaCoO_3$ / g-C3N4 catalyst for the purification of pharmaceutical wastewater, study of the efficiency of decomposition of tetracycline hydrochloride upon PMS activation of various catalysts.

Research methods: The catalyst was prepared by a simple hydrothermal method; The catalyst was characterized by X-ray diffraction (XRD), X-ray photoelectron spectroscopy (XPS), scanning electron microscope (SEM) and Fourier transform infrared spectroscopy (Fourier transform infrared spectrometer, FT-IR), nitrogen adsorption desorption isothermal test, and Raman spectroscopy. The specific surface area, pore volume and pore diameter of the catalyst were analyzed by nitrogen adsorption desorption curve. The detection of free radicals is carried out by electron paramagnetic resonance (EPR) spectrometer method. The surface chemical composition and elemental chemical states of the samples were analyzed by XPS technique.

Practical value As a new wastewater treatment technology, advanced oxidation technology based on SO4•- has a good treatment effect on high concentration or refractory organics and potential application value.

Elements of scientific novelty. Advanced oxidation technology based on SO4•- is a new wastewater treatment technology that has a good treatment effect on high

concentration or refractory organics. Compared with traditional Fenton oxidation technology, it has the advantages of easy operation, low treatment cost and wide pH adaptation range.

Chapter 1 The research progress

1.1 Removal method of pharmaceutical wastewater

With the rapid development of society and economy, the problem of environmental pollution has become increasingly prominent. In view of the persistence and potential harm of pharmaceutical wastewater, people pay more and more attention to its migration, transformation and degradation in the environment [1]. At present, the treatment methods of organic pollutants include physicochemical method, biodegradation method and chemical oxidation method [2].

1) Physicochemical methods mainly include adsorption [3], membrane separation [4], etc. Adsorption method refers to the use of adsorbent to transfer target pollutants to the surface or channel of adsorbent through chemical or physical action, so as to achieve the purpose of pollutant transfer. Adsorption has the advantages of simple design, convenient operation, strong flexibility and wide application range. It can be used for the removal of heavy metals, dyes, pesticides and other pollutants. Activated carbon, a common adsorbent, has been widely used because of its excellent adsorption performance due to its large specific surface area, large micropore volume and high porosity. However, adsorption can only realize the phase transfer and enrichment of pollutants, and is not essentially removed. If the adsorbent is not properly treated, it will cause potential secondary pollution. Membrane separation method is a method of purifying water quality with non-porous or porous membrane, which is mainly divided into reverse osmosis, microfiltration, nanofiltration and ultrafiltration. These methods require specific equipment and films, which are simple to operate and have no secondary pollution. Reverse osmosis is mostly used to remove high concentration salt

in water. The research on the removal of antibiotics mostly focuses on nanofiltration and ultrafiltration. Most studies show that the removal rate of antibiotics by membrane separation method is more than 90%. However, high concentration of antibiotics is easy to lead to membrane blockage and membrane pollution, which increases the operation cost.

2) Biodegradation [5] is the main process of sewage treatment system, which consumes a certain amount of organic and inorganic substances to remove pollutants in water by relying on microbial metabolism and reproduction. Biological treatment technology has good treatment effect for traditional pollutants. Biological treatment technology is easy to control and less investment. At the same time, it also has the problems of large floor area, disposal of surplus sludge and low removal rate of refractory toxic organic pollutants. According to whether oxygen is needed for microbial decomposition of pollutants, biodegradation can be divided into anaerobic biodegradation and aerobic biodegradation. Anaerobic method is suitable for sewage with large organic pollutant load. It can hydrolyze and acidify macromolecules in sewage into small molecules, increase the biodegradability of pollutants, and is conducive to series use with aerobic method. Aerobic biodegradation includes activated sludge process and biofilm process. The aerobic method is applicable to the sewage with medium and low pollution load. Although the treatment is complete and the effluent concentration is low, it has the limiting factors such as large floor area, long operation cycle, aeration and low microbial activity. It cannot completely remove the organic matter in the medical wastewater, especially the refractory organic pollutants such as antibiotics.

3) Chemical method

① Chemical flocculation [6]

Flocculation method refers to the method of purifying wastewater through mixing, reaction, sedimentation or floating after adding flocculant to wastewater. Common flocculants include inorganic flocculant, organic flocculant, composite flocculant, etc. Synthetic organic polymer flocculant has been widely concerned because of its large molecular weight, many functional groups, good flocculation effect and wide application range. With the development of pharmaceutical industry, the drug molecules are more complex, and the decolorization of flocculation method is more difficult. It is necessary to develop more efficient flocculants.

② Traditional chemical oxidation [7]

The traditional chemical oxidation method uses the oxidizing oxidation of oxidants to decompose organic matter, so as to achieve the purpose of water purification. The commonly used oxidants include O_3, NaClO, ClO_2, H_2O_2, etc. Due to the harmful small molecular organic halogenates easily produced by NaClO and ClO_2 in the oxidation process, such as chloroform and H_2O_2, the oxidation capacity is weak when used alone. Therefore, ozone oxidation is the most widely used chemical oxidation technology at present, but it is difficult to popularize its application on a large scale due to high power consumption and high treatment cost.

③ Advanced oxidation process [8, 9]

Advanced oxidation processes (AOPs), also known as deep oxidation, refers to the oxidation method of oxidizing and decomposing organic matter by generating strong oxidizing free radicals (•OH and SO_4•- etc.) through the synergistic action of light,

electricity, catalyst and oxidant. Compared with the traditional oxidation method, advanced oxidation technology has the following advantages: I) strong oxidation ability, low selectivity and fast reaction rate, in which the reaction rate constant of •OH with most organic compounds can reach 10^6-10^9 (m•s^{-1}); II) the reaction conditions are mild, which can oxidize and decompose most refractory organic pollutants, and even mineralize into CO_2 and H_2O, with little secondary pollution; III) the technology can be used alone or in combination with other technologies, especially as the pretreatment process of biological treatment method, which increases the biodegradability of wastewater and reduces the treatment cost; IV) simple operation and easy management. Advanced oxidation technology is more and more widely used in medical wastewater treatment because of its strong oxidation. Advanced oxidation technologies mainly include Fenton process, Fenton like process, photocatalytic oxidation, electrocatalytic oxidation, ultrasonic oxidation, ozone oxidation, microwave oxidation, wet oxidation, supercritical water oxidation, etc. Among them, Fenton process and Fenton like process are the earliest and most widely studied advanced oxidation technologies.

The traditional Fenton method has some disadvantages, such as narrow pH suitable range, producing a large amount of iron sludge, and the iron ion in the effluent cannot be recovered [10]. In order to overcome the shortcomings of the traditional Fenton Method, a Fenton like technology with catalyst instead of iron ion was developed. In order to further enhance the reaction and mass transfer efficiency of Fenton and Fenton like processes, the Synergistic Technology of light, electricity, ultrasound, microwave and their coupling was further developed. With the continuous technological innovation, aiming at the problem of demanding pH conditions in the traditional Fenton system, a

new advanced oxidation technology based on SO$_4$•− was developed to degrade organic pollutants. Compared with •OH, SO$_4$•− has longer service life, stronger selectivity, higher redox potential [11], wider applicable pH range, and persulfate is more stable and easy to transport and store. Therefore, advanced oxidation technology based on SO$_4$•− has become one of the research hotspots of emerging organic pollutant control in recent years.

1.2 Advanced oxidation technology based on sulfate radical

1.2.1 Overview of persulfate advanced oxidation technology

In recent years, AOPs technology based on SO$_4$•$^-$ has developed rapidly and become another emerging technology for efficient treatment of organic pollutants. Compared with the strong oxidizing •OH in HR AOPs, SO$_4$•$^-$ has the following advantages: I) the research shows that SO$_4$•$^-$ has an oxidation potential of 2.5 ~ 3.1 V (vs. NHE), which is higher than that of •OH 1.8 -2.7 V (vs. NHE). SO$_4$•$^-$ with higher oxidation potential showed strong reaction activity. II) SO$_4$•$^-$ is more specific and efficient than •OH. The specificity of SO$_4$•$^-$ is that it tends to react with organic pollutants containing unsaturated bonds and aromatic π electrons, and has higher electron transfer efficiency than •OH. •OH reacts with pollutants of different components in the environmental background through high-speed hydrogen abstraction and electrophilic addition. III) As the main oxidation species in the reaction, SO$_4$•$^-$ can react efficiently in a wide pH range of pH= 2 - 8, which has a wider application range than •OH and significantly reduces the cost. IV) The half life of SO$_4$•$^-$ (30 ~ 40 μs) is longer than that of •OH (less than 1 μ s). In terms of half-life, the half-life of SO$_4$•$^-$ is 30 ~ 40 times that of •OH. SO$_4$•$^-$ can exist more stably in the process of pollutant

degradation and fully react with the target degradants.

1.2.2 Activation method of persulfate [11-13]

Due to the low activity of PS itself, it is necessary to break the O-O bond with the help of external energy or catalyst to produce highly active species. At present, the research of advanced oxidation technology based on PS mainly focuses on PS activation method. The common energy activation methods mainly include thermal activation, microwave radiation activation, ultrasonic activation, ultraviolet radiation activation and so on. Chemical activation methods mainly include alkali activation, transition metal ion activation (Ag^+, Co^{2+}, Mn^{2+}, Fe^{2+}, Cu^{2+}, etc.), heterogeneous catalysts (carbon materials, metal oxides, zero valent metals, metal complexes, metal organic framework materials and their derivatives, etc.).

1) Thermal activation

Thermal activation mainly provides sufficient activation energy for the reaction system by heating up. Under the action of thermal radiation, the breaking of persulfate O-O bond requires 140.2 kJ/mol activation energy to produce $SO_4{}^{\bullet-}$. The specific formula is shown in formula (1-2). For thermally activated persulfate system, temperature is an important factor, and increasing the temperature can increase the activation rate.

$$S_2O_8{}^{2-} + heat \rightarrow 2\ SO_4{}^{\bullet-} \qquad (1)$$

$$HSO_5{}^- + heat \rightarrow 2\ SO_4{}^{\bullet-} + {}^\bullet OH \qquad (2)$$
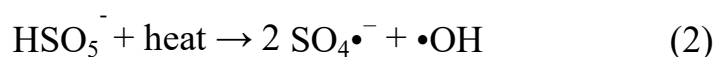
Heating method is a very effective way of catalytic activation. The research shows that PMS can be catalytically activated at room temperature (22 ^{o}C). The heating

method mainly depends on increasing the system temperature to accelerate the oxygen bond breaking reaction of PMS in aqueous solution. However, if the activation efficiency of PMS in a larger reaction system is to be significantly improved, the heat required is relatively high, and the solubility of some organic substances is also increased when the temperature increases, which is not very suitable for the advanced treatment of practical pharmaceutical wastewater. In addition, during the heating process, it is easy to cause $SO_4^{\bullet-}$ quenching, which affects the progress of organic degradation reaction.

Generally, thermal activated persulfate technology [14] has obvious degradation only when it is higher than 50 ^{o}C. In practical engineering, the water temperature will not exceed 40 ^{o}C, and high energy output has become the main factor limiting the large-scale popularization and application of thermal activated persulfate technology.

2) Ultraviolet radiation activation

Radiation catalysis mainly relies on ultrasonic, ultraviolet and γ. X-rays radiate the reaction system and use the radiation energy to promote the decomposition of PMS (reaction formula 3-4). Compared with the other two methods, ultraviolet radiation activation [15] is considered to be a more promising method for safety and economy. Ultraviolet (UV) refers to the radiation with a wavelength of 10-400 nm in the electromagnetic spectrum and an energy of 3-124 eV. Generally, it can be divided into long wave UV-A, medium wave UV-B and short wave UV-C. Water disinfection mainly uses UV-C. UV mainly destroys nucleic acids by radiation to microorganisms. The earliest use of UV to disinfect water can be traced back to the early 20th century.

Since UV can inactivate Cryptosporidium and Giardia lamblia, UV radiation began to replace chlorine as the main disinfection technology. In addition to being widely used in sterilization and disinfection, UV itself has oxidation ability and degradation ability, but the reaction time is long. It can be used to activate peroxide, open its peroxide bond and produce highly active free radicals. As shown in reaction formulas (3-4), 1 mol PMS produces 1 mol $SO_4 \bullet^-$ and 1 mol $\bullet OH$, and 1 mol PDS produces 2 mol $SO_4 \bullet^-$. The wavelength range of persulfate photolysis is 248-351 nm. When the wavelength was 254 nm, the free radical production efficiency of activated PDS increased significantly.

$$S_2O_8{}^{2-} + UV \rightarrow 2\ SO_4 \bullet^- \qquad (3)$$

$$HSO_5{}^- + UV \rightarrow SO_4 \bullet^- \qquad (4)$$

A large number of studies focused on comparing the degradation performance of UV/PDS and UV/PMS oxidation systems. Sharma [16] and other systems compared the degradation and mineralization of bisphenol A by UV/H_2O_2 and UV/PDS oxidation systems. The experimental results showed that when the UV wavelength was 254 nm, the pH was neutral, the temperature was $29 \pm 3\ ^oC$, the molar ratio of oxidant to bisphenol A was 5.7:1, and the UV/PDS oxidation system was 240 min, the removal rate of bisphenol A could reach about 95%, The pollutant removal rate of UV/H_2O_2 oxidation system is 85%, and the molar ratio of oxidant to bisphenol A is 53.4:1. The applicable pH range of UV/PDS oxidation system is 3-12, while UV/H_2O_2 oxidation system can degrade pollutants only under acidic conditions, and the former has strong resistance to the interference of bicarbonate, chloride ion and humic acid. It is inferred that $\bullet OH$ is easier to be quenched than $SO_4 \bullet -$.

UV activation does not require additional catalyst, and there is no problem of catalyst recycling. In addition, UV disinfection equipment and technology have been mature in the field of water treatment and are widely used in the field of water supply treatment. UV in sunlight accounts for about 5%. Persulfate can be activated by natural light to degrade pollutants, which can not only save cost, but also achieve the purpose of pollutant removal.

3) Ultrasonic activation [17]

PDS and water can be activated by ultrasound to produce $SO_4\bullet-$ and $\bullet OH$ (as shown in formulas (5-6)). Ultrasound is often introduced into heterogeneous catalytic system as an auxiliary to improve solid-liquid two-phase mass transfer, accelerate reaction rate and enhance pollutant removal rate. Cavitation caused by ultrasound leads to local high temperature and high pressure, and the O-O bond of PDS is cracked, resulting in $SO_4\bullet-$. Ultrasonic (US) activation has attracted much attention because it does not produce secondary pollution and toxic by-products, simple system and low energy consumption.

$$S_2O_8^{2-} + US \rightarrow 2\ SO_4\bullet^- \qquad (5)$$

$$HSO_5^- + US \rightarrow SO_4\bullet^- \qquad (6)$$

In US/PDS activation system, ultrasonic power, frequency and time will affect the activation and degradation effect. Wang [18] et al. studied the degradation of humic acid by US/PDS. 90% removal rate can be achieved after 2 h. When the ultrasonic power is 80 W, the TOC removal rate is 58.6%. With the increase of ultrasonic power to 200 W, the TOC removal rate increases to 83.1%. Increasing the ultrasonic power can improve the degradation efficiency and degradation rate, because a large number of

cavitation bubbles are generated, which provide more energy for the generation of free radicals and improve the generation rate of free radicals. Moreover, the solution turbulence caused by ultrasound can strengthen the mass transfer rate. In addition, acidic conditions and high temperature are also conducive to the degradation of humic acid. He also used the same activation method to degrade carbamoyl nitrogen grass in water. At 2 h, the pollutant removal rate was 89.4%. The degradation process of pollutants accorded with the quasi first-order kinetic model. Increasing PDS concentration and ultrasonic power was conducive to pollutant degradation. The main active species was $SO_4^{\bullet-}$. Increasing PDS concentration can increase the production of free radicals, but the proportion of free radicals remains unchanged. The temperature at the bubble water interface is about 340 K. PDS is activated locally at high temperature, and $SO_4^{\bullet-}$ hydrolysis produces $\bullet OH$, resulting in an order of magnitude higher yield of $\bullet OH$ than $SO_4^{\bullet-}$. According to the free radical quenching experiment, $SO_4^{\bullet-}$ is the dominant free radical. Li et al. [19] explored the effect of ultrasonic frequency on the degradation of trichloroethane in US/PDS oxidation system. The reaction rate increased with the increase of ultrasonic frequency. When the ultrasonic frequency is 400 kHz, the reaction rate constant is 0.0014 min^{-1}, 280 times higher than that at 50 kHz. When the ultrasonic frequency is too low, the bubble lasts for a long time, and the free radicals in the cavitation bubbles have their own quenching effect. Higher ultrasonic frequency is conducive to the generation of free radicals. Because the bubble life is shorter, the free radicals can enter the liquid from the bubbles, avoiding the free radical loss caused by self quenching.

4) Alkali activation [20-22]

Sodium hydroxide or potassium hydroxide is usually used to adjust the pH to 11 - 12 to realize alkali activation. The base catalyzes the PDS molecule to produce HO_2^-, which is used as an intermediate to carry out one electron transfer reaction with PDS to produce $SO_4\bullet-$. The research on alkali activation is less than other activation methods. Alkali activation requires high dose of PDS and strong alkali, while the alkali dose required to activate PMS is relatively small, but it is challenging to improve the performance of alkali/PMS activation system. Lou et al [23] reported that pyrophosphate and tripolyphosphate can enhance the degradation performance of alkali activated PMS system. According to the experimental results of free radical capture and quenching, superoxide radical and singlet oxygen are the dominant active species. Marchesi et al. [24] studied the performance of alkali/PDS oxidation system to degrade trichloroethane. The degradation rate increased with the increase of the ratio of OH^- to PDS. When the ratio was 8:1, the pollutants were completely removed. Qi et al. proved that the alkali/PMS system can degrade organic pollutants including lime 7, phenol and bisphenol A at room temperature. When pH > 9, the pollutant removal efficiency becomes significantly higher. The dominant active species are not $SO_4\bullet^-$, but superoxide free radicals and singlet oxygen.

5) Carbon material activation

The activation of PS based on carbon materials has its own unique characteristics: large specific surface area, high pore content, high activation rate and cost economy. The research shows that activated carbon, graphene, carbon nanotubes and biochar can efficiently activate PS. their activation mode of PS is mainly through the redox reaction of Sp^2 hybrid orbit of carbon atom and surface functional groups.

6) Transition metal ion activation

The catalytic activation of PMS by metal ions is mainly realized by electron transfer of redox reaction pairs formed by transition metal elements (reaction formula 1-8), which usually includes homogeneous metal ion catalytic activation and heterogeneous metal compound catalytic activation. At present, the commonly used transition metals mainly include iron, manganese, copper, nickel, cobalt and silver. Bouzayani [25] et al. compared the activation effects of Co, Cu, Ni and Fe plasma on PMS, and concluded that Co ions showed the best activation effect on PMS. However, when the transition metal is excessive, it will quench the generated free radicals, as shown in formula. Because iron is environmentally friendly, economical and efficient, it is most widely studied in activated PS technology. Wang and Chu used the Fe^{2+}/PMS homogeneous activation system to oxidize and decompose oxyanthracene dyes. The experimental results show that when the molar ratio of Fe^{2+}/PMS is 1:1, the pollutants can be completely removed within 90 min. There are many studies on Fe^{2+} activated PDS. Wang et al. [26] studied the degradation of acetaminophen in water by Fe^{2+}/PDS System. The optimal ratio of Fe^{2+} to PDS is 5:4. Chloride ion has a dual effect on the system. Ji et al. [27] degraded ciprofloxacin and sulfamethoxazole through $Fe^{2+/}$PDS oxidation system. They found that ciprofloxacin was easier to degrade than sulfamethoxazole because ciprofloxacin had higher electron density and could form a complex with Fe^{2+}. By comparing sulfamethoxazole and other sulfonamides, they found that heterocycles had a great impact on the degradation effect of sulfonamides. The main obstacle of iron ion activating PS is that Fe^{2+} can be converted to Fe^{3+} quickly, but the conversion rate of Fe^{3+} to Fe^{2+} is very slow. Therefore, maintaining an appropriate

concentration of Fe^{2+} is very important to improve the degradation effect. At present, there are three main methods: adding reducing agent, adding chelating agent and adding Fe^{2+} in sequence batch. These methods can maintain the cyclic regeneration and continuous activation of Fe^{2+}. Chelating agent can avoid the production of iron sludge.
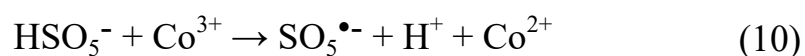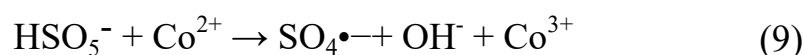
$$S_2O_8^{2-} + Me^{2+} \rightarrow SO_4\bullet^- + SO_4^{2-} + Me^{3+} \tag{7}$$

$$HSO_5^- + Me^{2+} \rightarrow SO_4\bullet^- + OH^- + Me^{3+} \tag{8}$$

1.3 Co/PMS system

As early as 1956, researchers found that Co can catalyze oxone (PMS trade name, chemical composition $2KHSO_5 \bullet KHSO_4 \bullet K_2SO_4$) to produce $SO_4\bullet^-$. The early Co/PMS system was mainly used in biochemistry and inorganic fields. It was not until 2003 that Anipsitakis et al. [28] applied this oxidation technology to the degradation of organic pollutants for the first time. Anipsitakis et al. also systematically studied the activation performance of a variety of transition metal ions on PMS. The experiment found that Co^{2+} is the metal ion with the highest activation efficiency. Compared with the widely used Fenton oxidation system, Co/PMS system effectively overcomes the inhibition effect of high pH on catalytic reaction, and has excellent oxidation activity in the range of pH=2-10; In addition, the Co/PMS system showed higher oxidation performance under the same catalyst and oxidant concentration. Therefore, Co/PMS system has been widely studied and applied.

1.3.1 Homogeneous Co/PMS system

In the homogeneous Co/PMS system, Co exists in the form of Co^{2+}, that is, Co^{2+} is directly added to the reaction solution, so the application is very convenient. The

reaction formula of Co^{2+} activating PMS to generate $SO_4\bullet-$ is as follows:

$$HSO_5^- + Co^{2+} \rightarrow SO_4\bullet- + OH^- + Co^{3+} \qquad (9)$$

$$HSO_5^- + Co^{3+} \rightarrow SO_5^{\bullet-} + H^+ + Co^{2+} \qquad (10)$$

$$SO_5^{\bullet-} + SO_5^{\bullet-} \rightarrow SO_4\bullet- + SO_4\bullet- + O_2 \qquad (11)$$

Matta et al. [29] studied the oxidation performance of Co/PMS system and traditional Fenton system for drug ritodrine. It was found that under the condition of pH= 3, the Co/PMS system with the same concentration was more efficient. The oxidation removal rate of the former against ritodrine reached 50%, while the latter was only 7%. Anipsitakis et al. [28] compared the degradation performance of 2,4-dichlorophenol between Co/PMS system and traditional Fenton system. The results showed that Co/PMS system showed higher degradation activity in a wide pH range of 2-9. Chan et al. [30] used Co/PMS system to oxidize atrazine. The results showed that the degradation rate of atrazine was as high as 95% within 1 h at room temperature. At the same time, the researchers compared the effects of different co salts ($Co(NO_3)_2$, $CoSO_4$, $CoCl_2$ and $Co(CH_3COO)_2$ on the activation performance of PMS. It was found that except for the slightly lower degradation efficiency of $CoCl_2$, other co salts showed higher activity, because $SO_4\bullet$ - would react with Cl- to form Cl•, $Cl_2\bullet-$ with lower oxidation capacity. Chen Xiaomin et al. [42] investigated the effects of various anions (H_2PO_4 -, HCO_3^-, NO_3^- and Cl^-) in pesticides on Co activated PMS. The experiments showed that high concentrations of HCO_3^- and Cl^- inhibited the reaction, H_2PO_4 - and low concentrations of HCO_3^- promoted the reaction, while NO_3^- had little effect on the overall reaction.

Although Co/PMS system can achieve efficient degradation of organic pollutants, it is often difficult to achieve high inorganic mineralization rate. In view of this defect, the researchers introduced light (including ultraviolet and visible light) to promote the complete oxidative degradation and improve the mineralization rate of the reaction. The simultaneous introduction of UV and Co is actually the combination of UV activated PMS and co activated PMS, which have a synergistic effect on the activation of PMS. Bandala et al. [31] studied the degradation of microcystin domoic acid in deionized water by UV/Co/PMS system. The research showed that the degradation rate of microcystin domoic acid reached 93% within 5 min; further, the researchers investigated the oxidation activity of the system under actual seawater conditions and found that the degradation rate could still be more than 90% within 5 minutes. Huang et al. [32] investigated the effect of ultraviolet light on the removal of Bisphenol A by Co activated PMS. The results showed that two different wavelengths of ultraviolet light (254 nm and 365 nm) promoted the catalytic system, and the inorganic mineralization rate of the reaction increased from 17% to 45% and 49% respectively. Although the Co/PMS system promoted by ultraviolet light can improve the mineralization rate of the reaction, the technology has high energy consumption and high cost of treatment equipment. Compared with ultraviolet light, visible light accounts for a larger proportion in natural light. Improving the utilization of visible light is conducive to the application of photo promoted Co/PMS system. Bandala et al. [33] used sunlight as the visible light source to investigate the effect of visible light on the degradation of herbicide 2,4-dichlorophenoxyacetic acid in Co/PMS system. The experiment showed that the degradation rate of 2,4-dichlorophenoxyacetic acid was up to 100% within 5

minutes, and the introduction of sunlight could increase the reaction kinetic constant of the system by 33 times.

Although homogeneous metal catalysts have the advantages of convenient operation, wide application range and high oxidation efficiency in the field of activating PMS, the homogeneous catalytic system shows many disadvantages, and the biggest problem is the leakage of metal ions. After the reaction, it is difficult to recover metal ions, which need to be added again, and some heavy metal ions are easy to form secondary pollution to the environment. In particular, cobalt ions have strong biological toxicity. A small amount of Co will cause lung diseases such as asthma and pneumonia, which limits the further application of the system. Therefore, developing heterogeneous Co/PMS system, immobilizing Co, realizing efficient catalysis and overcoming the shortcomings of homogeneous catalyst has become a breakthrough in the practical application of Co/PMS system.

1.3.2 Heterogeneous Co/PMS system

So far, heterogeneous Co based catalysts mainly include Co compounds and supported Co catalysts. Co compounds mainly include cobalt oxide, spinel and perovskite in different phases. Anipsitakis et al. [28] investigated the degradation of 2,4-dichlorophenol by CoO and Co_3O_4 activated PMS. It was found that only Co_3O_4 could play a catalytic role and had better activity at neutral pH; at the same time, the researchers investigated the co overflow in the two catalytic reactions. The results show that the Co overflow of Co_3O_4 is significantly lower than that of CoO, which may be due to the bonding between coo and Co_2O_3 in Co_3O_4 (composed of C_oO and Co_2O_3),

which improves the stability of CoO and reduces the co overflow. Compared with traditional particle catalysts, nano metal oxide catalysts have better catalytic activity because of the larger specific surface area and more active sites of nano materials. Chen et al. used nano-sized Co_3O_4 as catalyst to investigate the activity of activating PMS to degrade dye Acid Orange 7. It was found that Co_3O_4 nano catalyst showed efficient catalytic performance, with mineralization rate as high as 70%, and the degradation rate of Acid Orange 7 remained almost unchanged after repeated use for 6 times. Although the nano catalyst has excellent catalytic activity, it is difficult to separate and recover the catalyst by traditional precipitation filtration. In view of this defect, the researchers proposed to synthesize Co-Fe composite oxides with ferromagnetic properties as catalysts to achieve high-efficiency catalysis of Co and solid-liquid separation by using Fe magnetism. Yang et al. [34] prepared nano-sized Co-Fe oxide, $CoFe_2O_4$ by thermal oxidation method, and investigated its performance of activating PMS to degrade 2,4-dichlorophenol. The results showed that the catalytic system could degrade 80% of 2,4-dichlorophenol within 2 h.

Compared with Co oxides, supported Co catalysts are more widely studied and used. The supported Co catalyst is easy for solid-liquid separation to achieve the purpose of recovery. At the same time, Co can be effectively dispersed on the surface of the supported material, which is conducive to the increase of catalyst sites. In addition, due to the chemical bond force between the Co compound and the supporting material, Co can exist stably on the supporting material, which improves the stability of the catalyst. Among many materials, inorganic materials such as activated carbon, cationic resin, zeolite, molecular sieve, graphene, SiO_2, TiO_2 and Al_2O_3 have excellent stability and

large specific surface area, and are excellent catalyst supports. Therefore, heterogeneous Co catalysts based on these materials have been widely studied.

Yang et al. used nano-TiO_2 as the carrier of Co to investigate its catalytic activity for the degradation of 2,4-dichlorophenol by PMS. It was found that the degradation rate of 2,4-dichlorophenol was as high as 100% within 2 h, but the overflow of Co in the reaction was as high as 2.4 mg/L; The researchers further compared the catalytic activity between the system and Co_3O_4/PMS system. The results showed that the catalytic efficiency of Co/TiO_2/PMS was much higher than that of Co_3O_4/PMS system, which was caused by the existence of a large number of hydroxyl radicals on the surface of TiO_2 and the uneven distribution of small particle size Co_3O_4 (10-15 nm) on the surface of TiO_2. Chu et al. selected zeolite and cationic resin as loading materials and loaded Co on them to prepare heterogeneous Co catalyst, and investigated its activity of activating PMS to degrade herbicide Chlorsulfuron. The research showed that when the loading material was zeolite, the heterogeneous Co catalytic system could degrade 100% of Chlorsulfuron in 10 minutes, but the reusability of the catalyst was poor; When the loading material is cationic resin, the catalytic system has excellent catalytic activity and recycling performance. Shukla et al. [35] immobilized Co^{2+} on molecular sieves ZSM-5, Zeolite-A and Zeolite-X to prepare three heterogeneous Co/molecular sieve catalysts. The results show that Co-ZSM-5 has the best stability and a large amount of Co will overflow during the catalytic reaction; Compared with Co-ZSM-5, Co-zeolite-a and Co-zeolite-x have higher catalytic efficiency and can completely degrade phenol within 50 min. Yang et al. prepared heterogeneous Co catalyst with SiO_2, TiO_2 and Al_2O_3 as carriers, and investigated its activity of activating PMS to degrade

2,4-dichlorophenol. It was found that Co/SiO_2 showed the highest catalytic activity and could degrade nearly 98% of 2,4-dichlorophenol within 10 minutes, but the co overflow in the reaction process of the catalyst was as high as 1.4 mg/L; The catalytic activity of Co/TiO_2 and Co/Al_2O_3 is relatively low, but the stability is better. The overflow of Co in the catalytic process is less than 0.9 mg/L. Yao et al. [36] loaded Co nanoparticles on graphene to prepare heterogeneous catalyst, investigated its performance of activating PMS to degrade dye Acid Orange 7 in water, and found that more than 90% of Acid Orange 7 was degraded within 50 min; Kinetic and thermodynamic studies show that the catalytic reaction conforms to the pseudo first-order kinetic model, and the activation energy is 49.5 kJ/mol. Shukla et al. [37] used activated carbon as the carrier of Co_2O_3 to construct heterogeneous Co catalyst and applied it to the degradation of phenol. It was found that the TOC removal rate of phenol was as high as 80% within 60 min; In addition, the researchers recovered the catalyst by cleaning and filtration and applied it to the degradation of phenol again. It was found that the degradation efficiency of the second time was almost unchanged from that of the first time, while that of the third and fourth times decreased slightly; further study found that 1.6 mg/L Co spilled during the reaction.

Although heterogeneous Co catalysts effectively solve the defects of homogeneous Co catalysts and realize the recycling of catalysts, these catalysts still have the problem of Co overflow, which limits the further application of Co/PMS system. Appropriate supports can often bring excellent catalytic performance and practicability. Therefore, it is very important to select appropriate supports to build efficient and stable heterogeneous Co catalysts.

1.4 C$_3$N$_4$

1.4.1 g-C$_3$N$_4$ material introduction

The second periodic elements of the periodic table and their compounds have attracted extensive attention because of their special properties. Liebig discovered molecular compounds based on heptazine and triazine in 1834, melamine, melam, melem and melon. At that time, due to the lack of advanced analytical methods and technologies, these molecular compounds could not be fully characterized. In 1922, Franklin reported a method to synthesize amorphous nitrogen carbon compounds by means of cyanide Hg(CN)$_2$ and thiocyanide Hg(SCN)$_2$ pyrolyzed mercury. However, due to the lack of advanced analysis technology at that time, only the chemical composition was preliminarily analyzed. The hydrogen content in the compound was 1.1-2.0 wt%. In 1937, Pauling and Sturdivant first proposed that the coplanar tri-s-triazine unit is the basic structural unit of all polymer derivatives by using X-ray crystallography. Unfortunately, g-C$_3$N$_4$ has not been deeply studied because of its chemical inertia and poor solubility [38]. After decades of research and theoretical calculation, it is found that C$_3$N$_4$ has several different structures. Among them, α Phase, β Phase, cubic phase (C phase) and quasi cubic phase (P phase) are superhard materials, and graphite like phase (g-C$_3$N$_4$) is soft phase [10]. It is generally believed that the graphite like phase (g-C$_3$N$_4$) has two basic structural units: triazine (C$_3$N$_3$) and tri-s-triazine (C$_6$N$_7$). Among them, g-C$_3$N$_4$ with tri-s-triazine as the basic structural unit is the most stable. In triazine structure, one N atom can connect three triazine rings as a basic unit to form a 2D grid structure. The other basic structural unit tri-s-triazine is a layered grid structure formed by connecting several heptazine rings in the same way as

the above triazine rings. Similar to graphene, layers are connected by van der Waals force. Among the two possible isomers, Kroke et al. calculated by density functional first principle (DFT) that the structure of tri-s-triazine formed by heptazine ring connection has smaller binding energy and more stable.

1.4.2 Synthesis and basic properties of graphite phase carbon nitride

So far, there are many methods to prepare g-C_3N_4 with different structures and electronic properties, including thermal polymerization, chemical vapor deposition, solvothermal synthesis and plasma sputtering reactive deposition. Among them, thermal polymerization is the most commonly used synthesis method, because it is simple to operate, low cost, rich in raw materials and easy to obtain. Generally, g-C_3N_4 is easily prepared by thermal polymerization of organic monomers such as urea, melamine, dicyandiamide, cyanamide and thiourea at different temperatures (450-650 ℃).

Specifically, the formation of g-C_3N_4 is realized through different thermal condensation pathways of the above precursors [39-41]. The conversion of various precursors to g-C_3N_4 mainly includes stepwise nucleophilic addition, polycondensation and polymerization. For example, at about 234 ℃, cyanamide molecules condense to form melamine. At about 390 ℃, melamine rearranged to form a 3-s-triazine structure (melem). The structural units undergo further deamination polymerization, and finally polycondensate into a two-dimensional network polymer, g-C_3N_4, at about 530 ℃. However, g-C_3N_4 begins to decompose above 600 ℃, and the skeleton gradually collapses. When the temperature is greater than 700 ℃, g-C_3N_4 completely decomposes into small molecular substances, such as carbon dioxide and ammonia. Similarly, urea and thiourea molecules are first converted to melamine through addition and

condensation to produce g-C_3N_4, while dicyandiamide molecules can be directly condensed to melamine. It is well known that the type of precursor and preparation process will significantly affect the physical, chemical and optical properties of the product, which determines the photocatalytic performance of g-C_3N_4.

Similar to graphene, g-C_3N_4 has a two-dimensional layered structure. Its adjacent layers are stacked by van der Waals force, which comes from the weak π-π interaction between layers. In the g-C_3N_4 framework, carbon atoms and nitrogen atoms form a conjugated system through SP^2 hybridization, and then form an aromatic conjugated six membered ring structure through interphase arrangement of chemical bonds. The remaining lone pair electrons on the C and N atoms in the ring bond with each other to form a large π bond, while the six membered ring is connected with each other to form a π conjugate plane, which makes g-C_3N_4 have a unique electronic structure. In general, the band gap of g-C_3N_4 prepared by traditional thermal polymerization is about 2.7 eV, and its VB and CB potentials are +1.4V and -1.3V (vs NHE, pH = 7), respectively. It is composed of npz and CPZ orbitals, respectively. Compared with TiO_2, g-C_3N_4 can absorb visible light and ultraviolet light with a wavelength less than 460 nm in the solar spectrum, and has a higher utilization rate of solar light. At present, the mainstream view is that the basic structure of g-C_3N_4 can be divided into triazine and 3-s-triazine units. According to density functional theory (DFT), the structure based on 3-s-triazine unit has the highest thermodynamic stability among all allotropic forms of g-C_3N_4, which is about 30 kJ / mol lower than that of g-C_3N_4 composed of s-triazine motif. Therefore, in most subsequent studies, 3-s-triazine is generally considered to be the

basic skeleton of g-C$_3$N$_4$. In most charts in this paper, we also use 3-s-triazine as the basic structural unit of g-C$_3$N$_4$.

As an environment-friendly heterogeneous photocatalytic material, g-C$_3$N$_4$ has the advantages of simple synthesis, low cost, easy modulation of chemical composition and electronic structure, and shows good visible photocatalytic performance [42-44]. It has thermal and chemical stability, biocompatibility, environmental protection, acid resistance and alkali resistance under environmental conditions. These characteristics make it favored by researchers in photocatalytic advanced oxidation technology. However, bulk g-C$_3$N$_4$ usually has the disadvantages of small specific surface area, large band gap, fast photogenerated carrier recombination rate, narrow absorption range of visible light and high exciton binding rate. There are still many deficiencies in photocatalytic degradation of environmental pollutants, which greatly limits its large-scale practical application in the field of environmental purification.

1.4.3 Strategies for improving the catalytic performance of graphite carbon nitride

The core of advanced oxidation technology is to prepare efficient, stable, green and cost-effective catalysts. The physicochemical structure, photoelectric properties, morphology, specific surface area, crystallinity, type and quantity of defects, type and concentration of surface functional groups and other key physicochemical properties of catalysts affect the catalytic activity and stability. Therefore, in view of the above factors, the common methods of modifying g-C$_3$N$_4$ mainly include nanostructure design, heterojunction construction, impurity defect regulation, intrinsic defect regulation, adding electron capture agent and so on [45-48].

1) Nanostructure design

The design and construction of g-C$_3$N$_4$ with unique nanostructures by controlling the thermal polymerization conditions has been proved to be an effective strategy to obtain high-efficiency photocatalysts with various morphologies. Compared with the original g-C$_3$N$_4$, g-C$_3$N$_4$ with improved nanostructure often has larger specific surface area, appropriate energy level structure, special photoelectric properties, rapid charge separation and mass diffusion ability, so as to improve the photocatalytic degradation activity. In view of this, a lot of research work has been done to modulate g-C$_3$N$_4$ with different structures and sizes through hard template, soft template and template free methods, including zero dimensional quantum dots, one-dimensional nanorods, nanowires, nanotubes and nanofibers, two-dimensional nanosheets, three-dimensional hollow microspheres, nanoflowers and honeycomb porous structures.

Generally, the hard template method can be used to flexibly regulate the nanostructure of g-C$_3$N$_4$. In the hard template method, porous solid materials such as porous alumina, mesoporous silica and zeolite are often filled and heated together to synthesize porous g-C$_3$N$_4$ with controllable morphology and structure. Silica nanoparticles are one of the most common hard templates. In the early years, goettmann and others could control the specific surface area of g-C$_3$N$_4$ at 86 ~ 439 m^2/g by adjusting the mass percentage ratio of silica raw materials. However, the synthesis of porous g-C$_3$N$_4$ using silicon-based hard template will inevitably introduce harmful HF or NH$_4$HF$_2$ corrosive solution, and the synthesis process is relatively cumbersome and difficult to mass produce. In recent years, Chen et al. [49] obtained mesoporous carbon nitride (MPG CN) using low-cost and green CaCO$_3$ particles as hard templates. The obtained mpg CN has a large specific surface area, and its visible absorption band edge

extends from 460 nm to 800 nm. The results showed that the photocatalytic activity of mpg-C_3N_4 was 12.3 times higher than that of original g-C_3N_4.

In addition to the hard template method, the nanostructure of g-C_3N_4 can also be adjusted by the relatively green soft template method. Soft templates usually refer to non-metallic, non-ionic or ionic surfactants and amphiphilic block polymers. For example, Tahir et al. [50] synthesized high-performance multifunctional g-C_3N_4 nanofibers (GCNNF) with uniform structure by soft chemical method of pre acidification process. The results showed that under visible light, gcnnf could completely degrade RHB within 45 min, while g-C_3N_4 took 150 min. The improved photocatalytic activity is mainly due to its appropriate band gap, less structural defects, higher specific surface area and lower photogenerated carrier recombination rate. In addition, Zhao et al. [51] developed hollow mesoporous g-C_3N_4 microspheres with cyanuric acid and melamine as precursors and ionic liquid as soft template. The prepared hollow mesoporous g-C_3N_4 microspheres have high specific surface area and porosity, and their photocatalytic activity is 30 times that of the original g-C_3N_4. However, using these conventional surfactants as soft templates often requires complex post-treatment to remove the template.

Although various structures and morphologies can be obtained by hard template and soft template methods, these methods are very cumbersome and need post-treatment. As a green and simple alternative method, template free method has attracted extensive attention of researchers. For example, if the unstable substance in the precursor releases gas when heated, the autogenous chemical gas will blow out the condensed layer separately, resulting in a few or single-layer porous nano sheet. Zhang

et al. [52] synthesized a series of porous g-C$_3$N$_4$ through the thermal condensation reaction of dicyandiamide in air with the bubble template produced by urea pyrolysis as raw material. The photocatalytic activity of the optimized porous g-C$_3$N$_4$ for methylene blue and phenol was increased by 2.1 and 2.8 times, respectively. The results show that the visible light photocatalytic performance of porous g-C$_3$N$_4$ increases with the increase of urea ratio and calcination temperature. At present, researchers are exploring new non-metallic template or template free methods to regulate the microstructure and nanostructure of g-C$_3$N$_4$ based photocatalysts, which has become a current research topic.

2) Impurity defect control

Impurity defect regulation refers to introducing additional elements or impurities other than C and n into the molecular structure of g-C$_3$N$_4$, and changing the composition structure of g-C$_3$N$_4$ through displacement doping or gap doping, mainly including metal element doping and non-metal element doping. Impurity defect regulation can not only expand the absorption range and absorption capacity of g-C$_3$N$_4$ in the visible region and improve its utilization of visible light, but also greatly improve the separation efficiency of photogenerated carriers and prolong the carrier life, so as to improve the photocatalytic activity of g-C$_3$N$_4$.

Due to the strong coupling between cations in g-C$_3$N$_4$ nitrogen tank and negatively charged N atoms considered as lone pair electrons, g-C$_3$N$_4$ can easily bind and fix metal cations. Specifically, the high-density nitrogen based macrocyclic unit in the organic skeleton of g-C$_3$N$_4$ contains six lone pair electrons, which can smoothly form stable chemical coordination bonds with metal ions. Alkali metal ions (such as potassium and

sodium) and transition metals (such as iron, cobalt, copper and manganese) are coordinated into the nitrogen tank of g-C$_3$N$_4$, which can significantly improve the separation and migration speed of carriers, induce the distribution of space photogenerated electrons and holes, and improve their photocatalytic oxidation-reduction ability. For example, Zhang et al. successfully synthesized potassium doped g-C$_3$N$_4$ (k-C$_3$N$_4$) photocatalyst with dicyandiamide and potassium iodide as raw materials. Potassium doping leads to the positive shift of VB position of g-C$_3$N$_4$, which enhances the separation and migration ability of photogenerated carriers under visible light. The photocatalytic activity of optimized k-C$_3$N$_4$ for phenol and methylene blue was significantly improved, which was 3.3 times and 5.8 times higher than that of bulk g-C$_3$N$_4$, respectively. Xu et al. [53] successfully prepared iron (Fe)-doped surface alkalized g-C$_3$N$_4$ by one-step thermal polymerization. A small amount of Fe doping (0.05wt%) can accelerate the separation of photogenerated carriers and increase the generation of active species. The photocatalytic reaction rate of Fe doped g-C$_3$N$_4$ for the degradation of tetracycline under visible light is 3.0 times higher than that of bulk g-C$_3$N$_4$.

Non metallic doping is an economical and feasible method to control impurity defects, and can maintain the metal free characteristics of g-C$_3$N$_4$. The doped non-metallic elements can effectively adjust the electrical, optical properties and energy band structure of g-C$_3$N$_4$ by replacing lattice C or N atoms, so as to optimize the photocatalytic performance. Generally, due to the high ionization energy and different electronegativity of non-metallic atoms, once introduced, they can react with other compounds to obtain electrons and form covalent bonds, resulting in charge polarization,

changing the electron distribution around the doping position and accelerating the electron transfer rate. At present, various non-metallic dopants, including phosphorus, sulfur, oxygen, boron and halogen, have been used to control the impurity defects of g-C$_3$N$_4$. For example, Zhang et al. [54] prepared double oxygen doped porous g-C$_3$N$_4$ and revealed the changes of its internal electronic structure after oxygen doping in combination with theoretical calculation. After dioxygen doping, the surface charge density of g-C$_3$N$_4$ increases and the delocalized conjugate system expands, which accelerates the transfer and separation of carriers from the catalyst to organic pollutants. The results show that the photocatalytic degradation activity of bisphenol A is 9.0 times higher than that of original g-C$_3$N$_4$, and has a high removal rate of various phenols, chlorophenols and dyes. Huang et al. [55] prepared a new phosphorus oxygen Co doped g-C$_3$N$_4$ (POCN) from Hexachlorocyclotriphosphazene and polyvinylpyrrolidone. The P atom replaced the carbon atom in the g-C$_3$N$_4$ skeleton and the O atom replaced the nitrogen atom. Pocn showed significantly improved photocatalytic activity for the degradation of fluoroquinolones, such as enrofloxacin, ciprofloxacin, lomefloxacin and ofloxacin. Compared with the original g-C$_3$N$_4$, the degradation rate of enrofloxacin by pocn was increased by 5.2 times. The improvement of photocatalytic effect was attributed to its narrow band gap, effective charge separation and increased specific surface area.

3) Intrinsic defect control

So far, the widely used method for the synthesis of g-C$_3$N$_4$ is based on the solid-phase thermal polymerization of nitrogen rich precursors. The intermediate reaction in the polymerization process is incomplete, so it inevitably leads to low

crystallinity and amino defects. In addition, most common modification methods, such as thermal polymerization process optimization method, template free method, molten salt method and precursor weight adjustment method, can easily introduce intrinsic defect stiffness. Therefore, the intrinsic defect regulation strategy has been widely reported in the field of g-C_3N_4 based photocatalysis. Although g-C_3N_4 with intrinsic defects does not contain foreign impurities, its structure is still imperfect. In g-C_3N_4, intrinsic defects are mainly point defects. The research on point defects mainly focuses on vacancy defects (amino, cyano, C vacancy, n vacancy) and anti position defects (C doping, N doping). Intrinsic point defects have attracted much attention because of their simple synthesis and effective modification.

Due to the incomplete reaction of intermediates during the condensation of N-rich precursors, amino defects are inevitably generated, resulting in poor crystallinity. It is generally believed that these residual abundant in-layer amino groups lead to the high localization of radiation carriers and act as charge recombination sites in the photocatalytic reaction, which is not conducive to the photocatalytic process. The decrease of amino group is helpful to increase the crystallinity, improve the dissociation of excitons between layers, accelerate the migration of carriers in layers, expand the Wu conjugate system and increase the number of nonlocal redundant electrons to improve the conductivity. However, another view is that the surface basic sites of amino / imino can be used as chemical reaction active centers in response to the high capture degree of polluting molecules. The increase of amino group can strengthen the hydrogen bond interaction between layers and reduce the stacking distance between layers, so as to give more exposed active edges and cross plane diffusion channels, and greatly accelerate

the mass diffusion and carrier transport. It can be seen that the mechanism of amino group in g-C_3N_4 photocatalytic process is controversial, which needs to be further discussed and explained by researchers.

Antipositional defects are generated by the exchange of lattice positions between two adjacent particles of crystal constituent elements. In g-C_3N_4, inversion defects mainly refer to the defects caused by C doping and N doping. At present, the research on C doping is the most, and the research on N doping is less. Bao et al. [56] synthesized carbon doped g-C_3N_4 (C-CN) porous nanosheets with polyacrylamide as C source. Compared with g-C_3N_4, its band gap is reduced by 0.3eV and the degradation rate of active red X-3B is increased to 2.0 times, which can be attributed to the joint action of C-CN band gap reduction, visible light absorption enhancement and effective carrier separation. In addition, Li et al. [57] found that C atom can replace bridged N atom and form a large number of delocalized π bonds in the modified g-C_3N_4 (ACCN) skeleton to enhance its conductivity. C doping sites and the consequent introduction of carbon species can be used as electron sinks to promote the separation of electron hole pairs. The results showed that the degradation rate constant of Sulfamethoxazole by accn was 6.6 times that of g-C_3N_4. It is worth noting that due to the strong π - π interaction, the delocalized big Wu bond is also conducive to increase the adsorption capacity of C-CN for organic pollutants such as rhodamine B and tetracycline, and enhance the removal performance of active species on surface adsorbates in the subsequent photocatalytic process.

The atoms in the lattice leave the lattice due to the fluctuation of thermal vibration energy, leaving a vacancy in the original lattice. It is reported that the vacancy in

g-C$_3$N$_4$ can capture photogenerated electrons and transfer them to O$_2$ molecules adsorbed on the surface, so as to establish a favorable transmission path based on photogenerated electrons. At the same time, the vacancy can also greatly promote the adsorption of O$_2$ by g-C$_3$N$_4$. Zhou et al. Found that in the time-resolved fluorescence spectrum, the singlet lifetime of n-vacancy g-C$_3$N$_4$ (Nv-CN) is shortened, which means that the relaxation of excited states in NV-CN is easier to occur through non radiative inactivation. This may be due to the electron transfer to some favorable defect states, which enhances exciton dissociation and promotes the yield and transfer efficiency of hot carriers. In addition, n vacancy provides more positions for adsorbed O$_2$, accelerates the transfer of electrons from g-C$_3$N$_4$ to surface adsorbed O$_2$, and promotes the generation of O$_2 \bullet^-$. The results showed that the degradation rate of sulfamethazine by Nv CN was 12.3 times that of g-C$_3$N$_4$. The vacancy can also enhance the adsorption effect of g-C$_3$N$_4$ on organic pollutants. Liu et al. Used quantum mechanical simulation for the first time to reveal the adsorption between sulfadiazine and c-vacancy g-C$_3$N$_4$ nanosheets. The results show that C vacancy can change the planar structure of g-C$_3$N$_4$ and significantly improve the adsorption capacity of sulfadiazine

In conclusion, the introduction of different intrinsic defects changes the electronic structure of g-C$_3$N$_4$ to varying degrees, and significantly affects the positive and negative positions of VB top and CB bottom in the energy band structure. In addition to amino defects and C vacancies, other intrinsic defects will significantly reduce the band gap of g-C$_3$N$_4$ and enhance its absorption capacity of visible light. In addition, they can also introduce the defect energy level into the intrinsic band gap, so as to expand the optical absorption range and receive more photogenerated electrons. At the same time,

the introduction of defects helps to delay the recombination of photogenerated carriers, because defects play the role of electron or hole traps, and optimize the original conjugate system of g-C_3N_4. It can not be ignored that the intrinsic defects of g-C_3N_4 material can also effectively introduce the coordination unsaturated center, which provides high active sites for the chemical adsorption and activation of reactant molecules and promotes the participation of reactant molecules in surface reactions.

1.5 Perovskite catalyst

Perovskite materials are widely used in catalysis, materials and solar cells because of their special thermal stability, electronic structure, ionic conductivity, electron mobility, oxygen mobility and redox properties. According to the structure type, perovskite can be divided into simple perovskite structure, double perovskite structure and layered perovskite structure. Among them, the simple perovskite structure is the most widely studied one. In recent years, in the field of catalysis, in addition to electrochemistry (such as ORR reaction [65] and OER reaction [66]) and gas-solid heterogeneous catalysis (such as Co oxidation [67] and NO conversion [68]), perovskite materials have also appeared in persulfate advanced oxidation technology.

1.5.1 Introduction of perovskite catalyst

Perovskite [58, 59] is an ABO_3 type metal oxide, in which a can be filled with alkali metals, alkaline earth metals or other cations, and B is usually occupied by transition metals. It has attracted people's attention because of its advantages such as high stability, low cost and element substitutability. This structure can introduce various metal ions into the frame structure, and can replace the cations at sites A and B with foreign cations without damaging the matrix structure. The specific structure of

perovskite is shown in Figure 1.1. Therefore, it is possible to control the change of cation oxidation state or the generation of oxygen vacancy. Perovskite materials have been widely used in catalysis, solar cells, sensors, etc. Recently, different types of perovskite catalysts ABO_3 (A = La, Ba, Sr and Ce; B = Co, Fe, Mn, Cu, Ni) have been applied to activate PMS to degrade organic pollutants and show high activity and stability. In order to further improve the performance of perovskite catalysts, researchers studied perovskite catalysts (such as Sr_2CoFeO_6, $La0.4Sr_{0.6}MnO_{3-\delta}$), the oxygen vacancy is increased by replacing A or B with exogenous cations. In addition, high specific surface area catalysts can provide more active sites for activated PMS to catalyze the degradation of pollutants. Therefore, increasing the specific surface area of perovskite can significantly improve its catalytic activity. The specific surface area of perovskite catalyst prepared by citric acid method, sol-gel method co precipitation method is too small, most of which are less than 10 m^2/g. Therefore, it is not enough to provide enough active sites to activate PMS, so how to prepare a high specific surface area perovskite catalyst is the key to improve the activity of the catalyst.
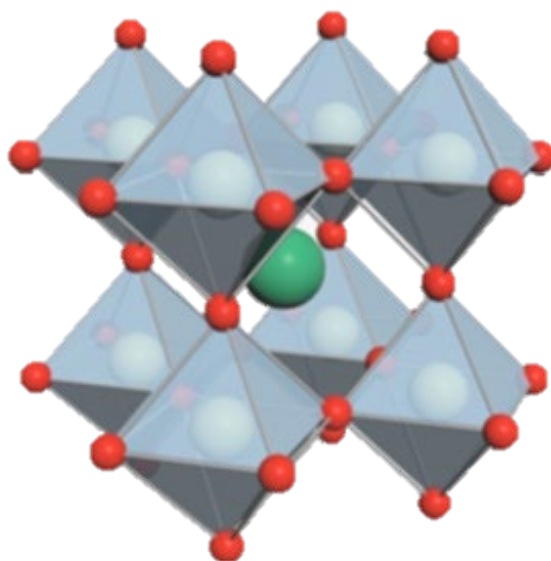
Figure 1.1 schematic diagram of perovskite structure

1.5.2 Application of perovskite catalyst in PMS activation

In recent years, perovskite materials have attracted more and more attention in the field of advanced oxidation due to their unique catalytic properties, especially Fenton reaction. However, the research on perovskite materials as heterogeneous catalysts for PMS activation is very limited. Pang et al. [8] introduced cetyltrimethylammonium bromide into $LaCoO_3$ to activate PMS to degrade sulfazole (PBSA). The results showed that PBSA was almost completely degraded within 5 minutes, which may be mainly due to the Co-O bond on the surface of $LaCoO_3$, but the amount of catalyst used was large (0.5g • L-1) and the initial concentration of PBSA was low (5 mg • L-1). Su et al. [73] used $PrBaCo_2O_{5+\delta}$ with double perovskite structure for PMS activation, the results showed that $PrBaCo_2O_{5+\delta}$/ PMS system can completely degrade phenol and methylene blue within 15 minutes, but the dissolution amount of cobalt is as high as 9.8 mg • L^{-1}. It is speculated that the valence conversion of cobalt ions and the existence of oxygen vacancies in perovskite may be $PrBaCo_2O_{5+\delta}$, whic is the key to high-efficiency catalytic degradation. The catalytic effect of perovskite studied above is limited to a single cobalt, ignoring the advantages and characteristics brought by perovskite substitution. Duan et al. [74] investigated $Ba_{0.5}Sr_{0.5}Co_{0.8}Fe_{0.2}O_{3-\delta}$ Compared with Co_3O_4 and $CoFe_2O_4$, the results showed that $Ba_{0.5}Sr_{0.5}Co_{0.8}Fe_{0.2}O_{3-\delta}$/ The degradation efficiencies of PMS, Co_3O_4/PMS and $CoFe_2O_4$/PMS for phenol were 100%, 60.7% and 19.9%, respectively. In addition, it is found that oxygen vacancy and A-site metal ions with weak electronegativity may provide high charge density for cobalt sites, which is conducive to the interaction between cobalt and PMS to produce free radicals. Although

perovskites substituted at a and B sites are used to activate PMS, there is still a lack of systematic investigation on the substituted elements and amount.

1.6 Research ideas

In recent ten years, advanced oxidation technology based on sulfate radical ($SO_4\bullet-$) has attracted extensive attention. $SO_4\bullet-$ has high redox potential (2.5-3.1 V) and long half-life, which can oxidize and degrade most organic compounds, making it popular in the field of environmental catalysis. Among many $SO_4\bullet-$ generation technologies, homogeneous Co/PMS system has been widely studied because of its convenient operation, wide application range and high oxidation efficiency. However, there are some defects in the use of the system, such as difficult recovery of Co and secondary pollution caused by biological toxicity of Co, which limit its further application. There are two ways to solve this problem: one is to use high stability cobalt based catalysts, such as perovskite catalysts; the second is to load cobalt based catalyst on high specific surface area support. However, there are still some problems in activating PMS by the above methods. For example, the heterogeneous Co catalyst prepared by the previous method has the problem of Co overflow in the catalytic process, and the stability needs to be improved; therefore, the research and development of PMS activation technology with high efficiency and no secondary pollution is still a great challenge.

Appropriate supports can often bring excellent catalytic performance and practicability. Therefore, it is very important to select appropriate supports to build efficient and stable heterogeneous Co catalysts. Carbon nitride has many excellent properties: 1) large specific surface area and excellent adsorption performance; 2) The

surface contains abundant functional groups, which is easy to be chemically modified, which is helpful to establish a stable chemical bond between the catalytic center and the carbon nitride carrier; 3) Excellent physicochemical stability is conducive to the protection of active sites in the catalytic process. Based on the above analysis, carbon nitride was selected as the catalyst carrier to construct heterogeneous Co catalyst. The catalyst not only has excellent catalytic performance, but also improves the stability of the catalytic center and solves the problem of Co overflow of heterogeneous Co catalyst.

Chapter 2 The experimental method

2.1 Preparation process of catalyst

2.1.1 Preparation of LaCoO$_3$

According to La:Co = 1: 1: stoichiometric metal nitrates La (NO$_3$)$_3$·6H$_2$O and Co(NO$_3$)$_2$·6H$_2$O were dissolved together in an appropriate amount of distilled water,then the Citric acid was added to this mixture according to molar ratio of citric acid/total cations of 2.4.

The solution was dried at 80 °C overnight.The obtained sample was calcinedd at 700 °C for 2 h in the muffle .Finally, the perovskite-type oxide LaCoO$_3$ sample was obtained and identified by XRD.

2.1.2 Preparation of g-C$_3$N$_4$

The g-C$_3$N$_4$ powders were synthesized by heating melamine in a muffle furnace. Specific operations are as follows: A certain amount of of melamine was put into an alumina crucible with a cover and heated to 550 °C at a heating rate of 2 °C·min^{-1}, then kept at this temperature for 4 h. After the reaction, the alumina crucible was naturally cooled to room temperature. The resulting yellow product (g-C$_3$N$_4$, identified by XRD) was collected and grounded into powders for further use.

2.1.3 Preparation of LaCoO$_3$/g-C$_3$N$_4$ composite catalysts

A certain amount of carbon nitride and lanthanum cobaltate are placed in a muffle furnace and heated to 500 ℃ for 2 hours according to different loads (10%,20%,30%,40%,50%), the resulting black powder (LaCoO$_3$/g-C$_3$N$_4$, identified by XRD) was collected and grounded into powders for characterizing

2.2 Catalyst characterization

In this paper, the morphology and structure of catalyst $LaCoO_3$, g-C_3N_4 and $LaCoO_3$/g-C_3N_4 samples were characterized by the following test techniques, mainly including X-ray diffraction (XRD), X-ray photoelectron spectroscopy (XPS), scanning electron microscope (SEM) and Fourier transform infrared spectroscopy (Fourier transform infrared spectrometer, FT-IR), nitrogen adsorption desorption isothermal test, and Raman spectroscopy.

2.2.1 X-ray diffraction (XRD)

The crystal structure and composition of the samples were characterized by a Bruker D8 advanced X-ray powder diffractometer. The test conditions are as follows: the X-ray is composed of copper target Kα Provided by ray source, $\lambda = 1.54$ nm, the tube voltage is 45 kV, the tube current is 40 Ma, the scanning speed is 0.026 ^{o}/s, and the scanning range is 2 $\theta = 5^{o} \sim 80^{o}$.

2.2.2 X-ray photoelectron spectroscopy (XPS)

XPS can be used to test the surface composition of the sample and the bonding relationship between elements. The test principle is that by shooting the material surface with X-rays with specific energy, photogenerated electrons will be generated in the depth range of 0.5 ~ 3 nm. These photogenerated electrons are formed by certain specific elements, so the elements contained in the material can be analyzed by analyzing these photogenerated electrons, At the same time, the content of elements and their bonding information can be obtained by further analysis of physical parameters such as peak strength. In this paper, ESCALABXi+ X-ray photoelectron spectrometer produced by Thermo Fisher company of the United States is used. X-ray from

aluminum target Kα The final characterization results were fitted by XPS peak software and corrected with C 1s peak 284.8 ev.

2.2.3 Fourier transform infrared spectroscopy (FT-IR)

The information of functional groups on the sample surface and the types of internal chemical bonds can be understood by FT-IR. The test principle is to make some molecules in the sample transition to the vibrational energy level with higher energy through the infrared radiation sample, and the functional spectrum with wave number as variable is calculated by Fourier transform. Analyze the position of the characteristic absorption band in the spectrum and identify the possible functional groups and chemical bonds in the molecule. In this paper, the IRAffinity-1 Fourier transform infrared spectrometer produced by Shimadzu company in Japan was used for testing, and the scanning range is $400 \sim 4000$ cm^{-1}.

2.2.4 Nitrogen adsorption desorption isothermal test

Nitrogen adsorption desorption analysis is to analyze the nitrogen adsorption desorption curve of sample materials by BET and BJH methods to obtain the specific surface area, pore volume and pore size distribution of porous samples. The test and analysis principle is to measure the adsorption and desorption capacity of the sample material for nitrogen under different relative pressures in the liquid nitrogen environment with a temperature of 77K, so as to obtain the adsorption desorption curve of the sample material for nitrogen, calculate the specific surface area of the material by BET method (formula 2-1), and calculate the pore size distribution in combination with bjh (Barrett Joyner halenda) model. In this paper, the multi station automatic specific surface area and microporous physical adsorption instrument asap2460 produced in the

United States is used, and the relative pressure range is 0 ~ 1.

$$V = \frac{V_m PC}{(P_0 - P)[1 - (P/P_0) + C(P/P_0)]}$$

2-1

V -- actual adsorption capacity of sample (mL);

V_m -- saturated adsorption capacity of nitrogen monolayer (mL);

P -- partial pressure of nitrogen (Pa);

P_0 -- saturated vapor pressure of nitrogen at liquid nitrogen temperature (Pa);

C -- constant.

2.3 Catalyst activity evaluation

Firstly, 100 mg/L tetracycline hydrochloride solution was prepared in a 500 mL volumetric flask and transferred to a blue-cap bottle with an outer wall shading treatment as a reserve solution for low temperature storage. When necessary, the solution was transferred to a volumetric flask and diluted to 20 mg/L for degradation experiments. 50 mL tetracycline hydrochloride solution was added into 100ml conical flask, followed by addition of a certain amount of catalyst. NaOH or H_2SO_4 were used to adjust the pH of the solution. Then the tube was transferred to a thermostatic water bath, the temperature was controlled at 25 ^{o}C. To eliminate the effects of adsorption of different catalysts, the reaction was stirred for 0.5-3 hours to ensure that the reaction reached adsorption equilibrium.

Then a certain amount of fresh PMS solution was added, and the time was immediately timed and determined to be zero. Samples were taken at 0, 5, 10, 15, 20, 25, 30 min and filtered through 0.22 μm glass fiber membrane. After filtration, 2 mL of the sample was placed in a 10 mL centrifuge tube, and 2 mL methanol was added to quench

free radicals. The quenched samples were poured into a colorimetric dish and their absorbance was measured by by a UV–Vis spectrophotometer (λ = 358 nm).. The pollutant degradation and removal rate is calculated based on Equation (2-2) :

$$RP=(C_0-C_t)/ C_0 \times 100\% \qquad 2\text{-}2$$

RP is the degradation removal rate (%), C_0 is the initial concentration of ciprofloxacin in solution (mg/L), and C_t is the concentration of ciprofloxacin at time T (mg/L).

In order to ensure the accuracy of the experiment, repeat the experiment comparison for each group of experiments to analyze whether the data error meets the requirement of difference

2.4. Detection of active species

The detection of free radicals is mainly carried out by electron paramagnetic resonance (EPR) spectrometer. EPR spectroscopy is used to detect substances with lone pair electrons. The detection principle is to place the sample containing lone pair electrons in an external magnetic field and add microwave of specific frequency in the direction perpendicular to the external magnetic field, so that the electrons at low energy level will absorb the energy of microwave and jump to the orbit of high energy level, resulting in electron resonance, Then an obvious microwave absorption signal will be formed in the spectrum. The instrument used in this paper is EMX10/12 electron paramagnetic resonance spectrometer produced by Bruker company in Germany. The magnetic induction intensity is 3380 ~ 3580 g and the magnetic field frequency is about 9.77 GHz.

In order to identify the active species that catalyze the degradation of tetracycline

hydrochloride, the reaction system was tested by EPR. Firstly, according to the literature, the mechanism of transition metal cobalt catalytic activation PMS degradation of pollutants is mainly the role of $SO_4\bullet^-$ and a small amount of $\bullet OH$ formed in the system. Therefore, this paper mainly carries out EPR test on the above two free radicals.

(1) Testing of $SO_4\bullet^-$ and $\bullet OH$

5,5-dimethyl-1-pyrroline-n-oxide (DMPO) was used as free radical capture agent by EPR in the reaction system. Firstly, several 1 ml centrifuge tubes with addition of 20μL 1 mol/L DMPO solution were prepared. The following solution is then prepared. The initial concentration of PMS is 0.5 mM, the initial concentration of tetracycline hydrochloride is 10 mg/L, the reaction temperature is 25℃, the pH of the system is about 7, and the total reaction volume is 50 mL. At this point, 180 μL sample solution was placed into the centrifugal tube with DMPO solution, and the EPR map of PMS+DMPO was obtained. Then add $LaCoO_3/C_3N_4$ catalyst and start stirring reaction. Time reaction 5 min later, at this time, take 180 μL sample solution and put it into the centrifugal tube which has been added DMPO solution. The EPR map of PMS+DMPO+ $LaCoO_3/C_3N_4$ was obtained. The sampled fluid is quickly transferred from the centrifuge tube to a capillary and placed into an electron paramagnetic resonance spectrometer for EPR testing. The magnetic induction intensity is 3380~3580 G, and the magnetic field frequency is about 9.77 GHz.

(2) Detection of singlet oxygen ($^1O_2$)

For the test of singlet oxygen, EPR was also used, and 4-amino-2,2,6,6-tetramethylpiperidine (TEMP) was used as the capture agent. The experimental process is to take 40 μ L 0.1M temp and 160 μ L mix the above reaction

sample solution, and the other steps are the same as above; In addition, the reaction system and test instruments are the same as the above free radical detection, but the magnetic induction intensity is 3430 ~ 3530 G.

Chapter 3 The experimental results and discussion

At present, advanced oxidation technology based on $SO_4^{\bullet-}$ is widely used to treat pharmaceutical wastewater containing refractory organics. Among them, $SO_4^{\bullet-}$ produced by PMS activated by transition metal ions is the most widely used method at present. Cobalt ions become the most effective metal ions by virtue of their high redox potential. However, cobalt ions in homogeneous Co/PMS system will cause harm to water and human beings, so the research on heterogeneous Co/PMS system has become a hot spot.

In this chapter, g-C_3N_4 is selected as the carrier of lanthanum cobaltate, and $LaCoO_3$ doped g-C_3N_4 is prepared by simple hydrothermal method. Compared with pure $LaCoO_3$ material, $LaCoO_3/C_3N_4$ has higher activity for PMS activation and degradation of tetracycline hydrochloride, and the system has better research value. The main research contents are to explore the effect and mechanism of the prepared catalyst activated PMS for the degradation of tetracycline hydrochloride, including: (1) structural analysis of $LaCoO_3$, C_3N_4 and $LaCoO_3/C_3N_4$; (2) Performance evaluation of $LaCoO_3/C_3N_4$ activated PMS; (3) The single factor experiment affecting the degradation of tetracycline hydrochloride includes four parameters: the initial concentration of PMS, the dosage of $LaCoO_3/C_3N_4$, the pH value and temperature of the reaction system; (4) The mechanism of $LaCoO_3/C_3N_4$ activated PMS degrading tetracycline hydrochloride was explored by free radical inhibition experiment and free radical detection analysis.

3.1 Characterization results

3.1.1 X-ray diffraction

X-ray diffraction analysis is the main method to study the phase and crystal

structure of substances. By analyzing the diffraction pattern of X-ray diffraction of the catalyst, the composition of the material and the structure or morphology of atoms or molecules in the material could be obtained. When a substance (crystalline or amorphous) is subjected to diffraction analysis, the substance is irradiated by X-rays to produce diffraction phenomena in varying degrees. The composition, crystal form, intramolecular bonding mode, molecular configuration and conformation of the substance determine the unique diffraction pattern of the substance. X-ray diffraction method has the advantages of no damage to samples, no pollution, rapidity, high measurement accuracy and a large amount of information about crystal integrity. Therefore, as a modern scientific method of material structure and composition analysis, X-ray diffraction analysis has been widely used in the characterization of catalysts.
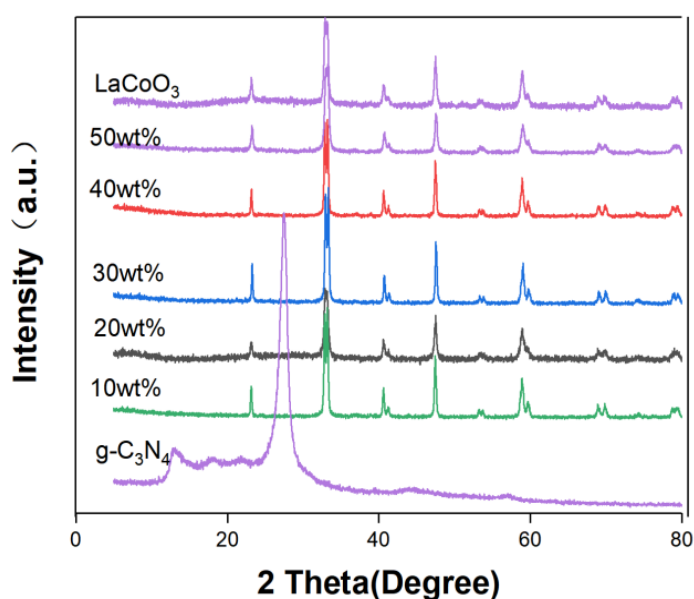

Fig. 3-1. XRD patterns of $LaCoO_3$/ C_3N_4 with different account of C_3N_4.

Figure 3-1 shows the XRD spectra of $LaCoO_3$/g-C_3N_4 composites with different g-C_3N_4 mass content, as well as the XRD spectra of pure $LaCoO_3$ and g-C_3N_4. It is

observed that each XRD diffraction peak of $LaCoO_3$ can be matched with the standard card of $LaCoO_3$ (JCPDS No. 01-084-0848). No other diffraction peaks were observed, indicating that the prepared sample $LaCoO_3$ has high purity. The characteristic peaks of g-C_3N_4 at 13.1 ° and 27.4 ° are consistent with the hexagon of g-C_3N_4 (JCPDS No. 01-087-1526) and with the diffraction planes (100) and (002) respectively. The diffraction peak at 2 θ=27.4 ° (D = 0.326 nm) is due to the interlayer stacking of graphite like structure, while the weak diffraction peak at 2 θ=13.1 ° (D = 0.676 nm) is related to the repeated triazine units in the plane [60, 61]. In addition, no characteristic peak of g-C_3N_4 was observed in $LaCoO_3$/g-C_3N_4 composites, which may be due to the low crystallinity of g-C_3N_4 [62]. It is also possible that the interaction between g-C_3N_4 and $LaCoO_3$ leads to the partial destruction of the long-range ordered crystal structures of g-C_3N_4 and the disappearance of the diffraction peak of g-C_3N_4.[63]

3.1.2 Fourier transform infrared spectroscopy (FT-IR)

Infrared spectroscopy is one of the important methods for qualitative identification of compounds and their structures. Molecules can selectively absorb the light in the infrared region of the electromagnetic spectrum, resulting in molecular vibration. This absorption specificity corresponds to the characteristic chemical bonds in the sample molecules. In the spectrum measured by the infrared spectrometer, the abscissa is the wave number (usually 4000-600 cm-1) and the ordinate is the absorption value of the sample to infrared radiation. Molecular spectroscopy, especially infrared spectroscopy, can understand the static adsorption of various molecules on the catalyst surface, and can also study the types, structures and bonding modes of adsorbed species under reaction conditions (or reaction steady state). It has become the most widely used

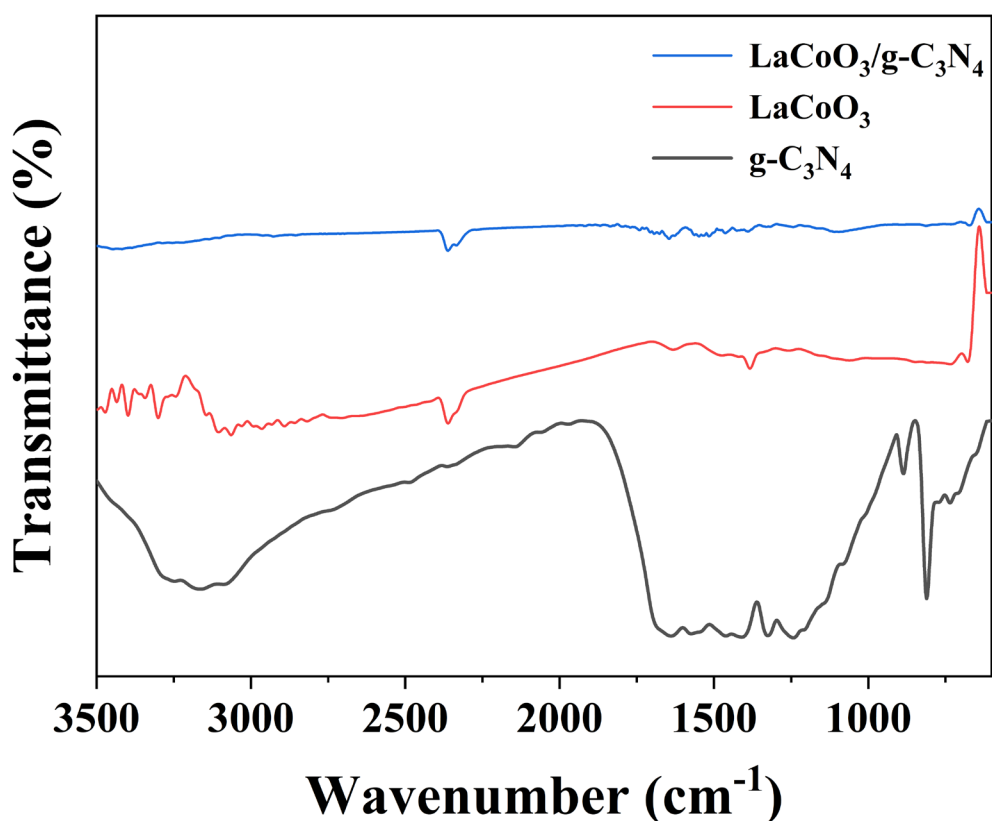characterization and identification method in catalytic research.

Fig. 3-2. FTIR of LaCoO₃/ C₃N₄ catalyst.

The composition and structure of LaCoO$_3$, g-C$_3$N$_4$ and LaCoO$_3$/g-C$_3$N$_4$ composites were determined by FT-IR, and the formation of heterostructure was further described. The results are shown in Fig. 3-2. For pure LaCoO$_3$, the IR bands observed near 562 cm^{-1} and 598 cm^{-1} are the characteristic stretching vibration of CoO bond in coo6 octahedron in LaCoO$_3$. The infrared band in the range of 1374 cm^{-1}-1645 cm^{-1} can be attributed to LaCoO$_3$ lattice vibration. In the FT-IR spectrum of pure g-c3n4, the peaks at 807 cm^{-1} and 1641 cm^{-1} are attributed to the bending vibration mode and C=N stretching vibration mode of s-triazine ring unit, respectively. The peaks at 1238 cm^{-1}, 1322 cm^{-1}, 1412 cm^{-1} and 1564 cm^{-1} correspond to the C-N stretching vibration in the carbon nitrogen heterocycle. The broad absorption peak near 3100 cm^{-1} is related to the characteristic stretching vibration of -NH and -NH$_2$ functional groups, which belongs to

the broken CN aromatic ring in g-C_3N_4. (6,7) in the case of FT-IR spectra of LaCoO$_3$/g-C_3N_4 composites, it can be easily seen that all characteristic peaks of LaCoO$_3$ and g-C_3N_4 are observed, and no new chemical bond or solvent residual absorption peaks are detected.

3.1.3 Raman spectroscopy

Raman spectroscopy has the characteristics of fast, simple and repeatable, and has no damage to the sample. The diameter of the laser beam is usually only 0.2-2 mm at its focusing position, and the sample demand is small, which is a major advantage over infrared. Therefore, Raman spectroscopy can analyze the micro region of the sample, which is especially suitable for the identification and research of single fluid inclusions with the size of 1um in the material and various solid mineral inclusions. Raman detection belongs to micro region detection, it has great advantages for the detection of filled samples. In addition, Raman can cover the range of 50-4000 wave numbers at one time, and can analyze organic and inorganic substances at the same time. If the infrared spectrum covers the same range, the grating, beam splitter, filter and detector must be changed; the detection of functional group region has no requirements for the light transmittance of the sample. Because Raman technology has many advantages above, it has become a widely used characterization and identification method in catalytic research.
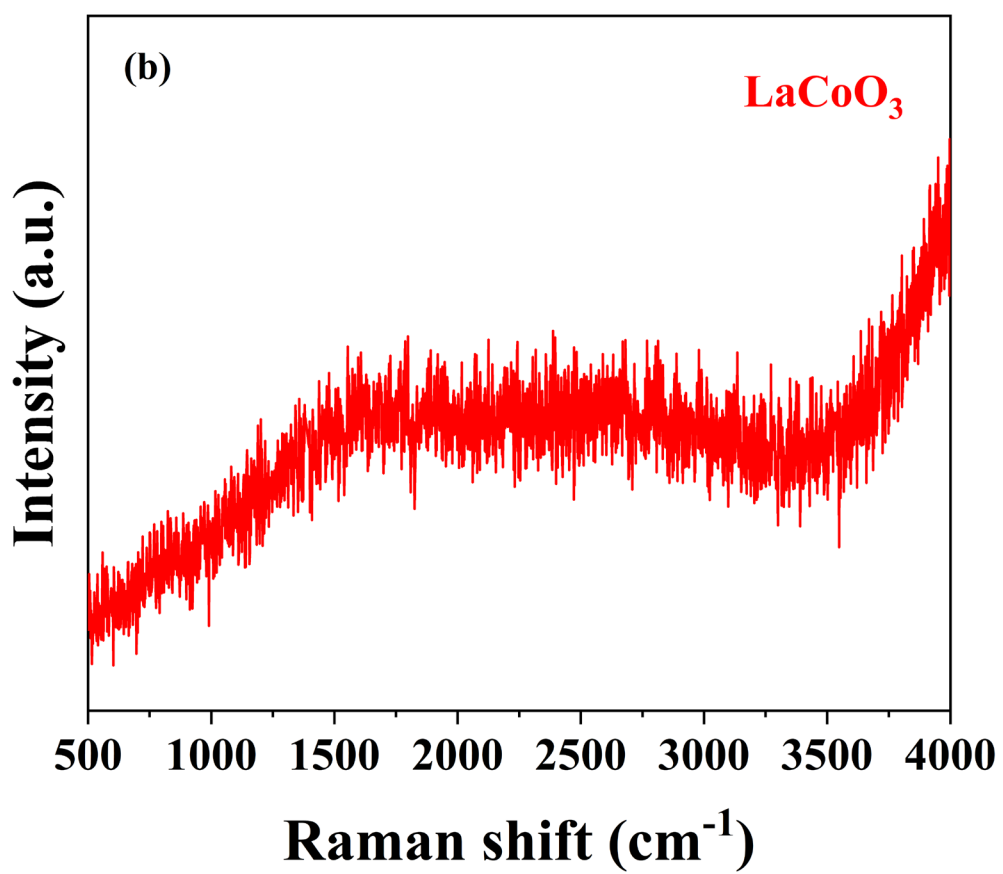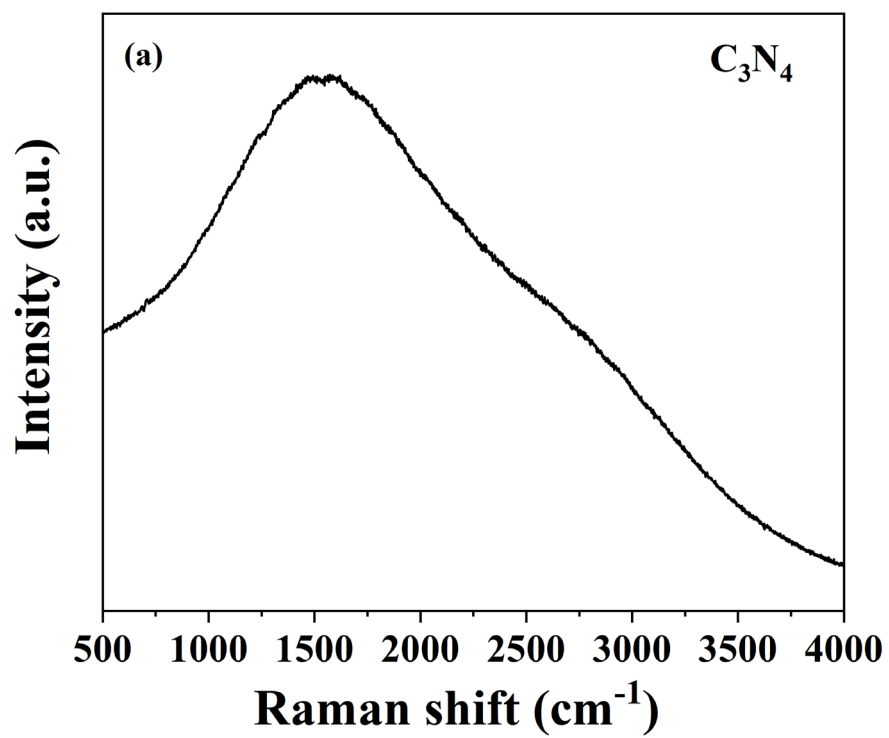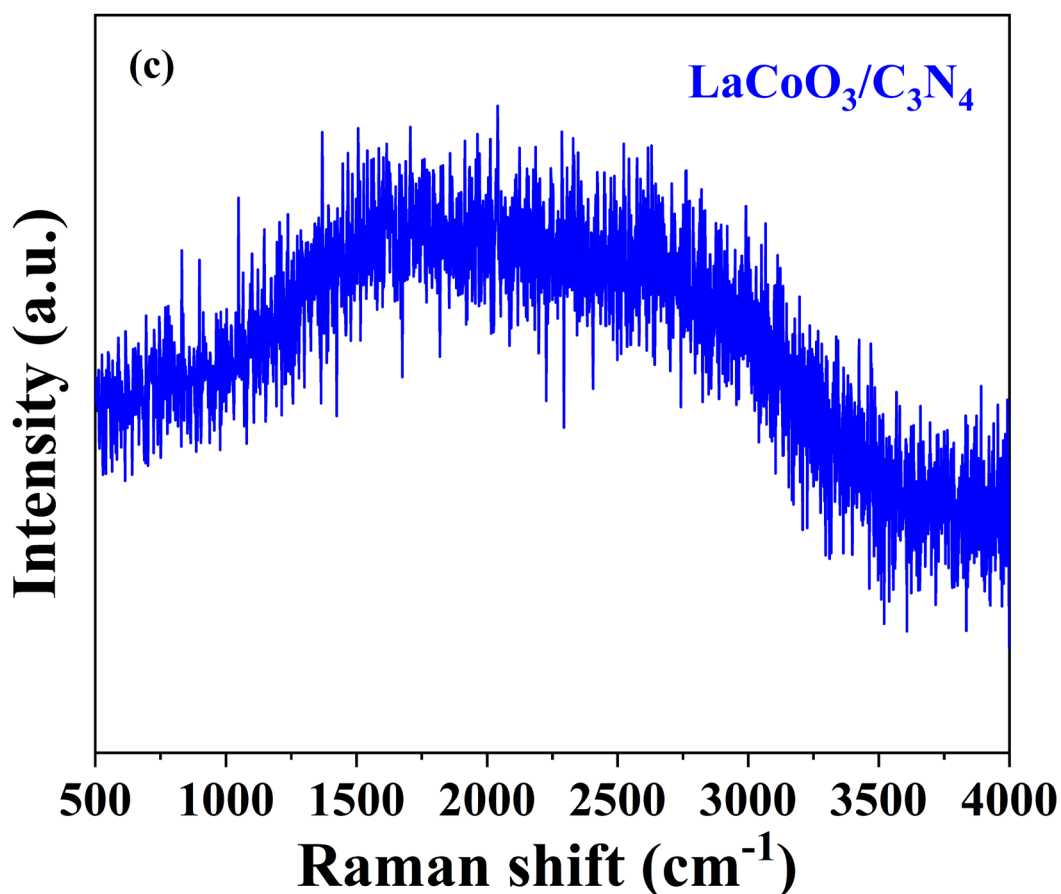
Fig. 3-3. Raman spectra of LaCoO$_3$/ C$_3$N$_4$ catalyst.

As shown in Fig. 3-3 (a) (b) (c), the Raman signal of g-C$_3$N$_4$ can be obviously observed in LaCoO$_3$/C$_3$N$_4$. Compared with the signal strength of the original g-C$_3$N$_4$, the signal strength of g-C$_3$N$_4$ is slightly stronger. This may be attributed to the contact LaCoO$_3$ surface enhanced Raman scattering (SERS) effect. A similar enhancement effect was previously reported in Ag/g-C$_3$N$_4$ heterojunction.

3.1.4 BET

The principle of physical adsorption technology is to use nitrogen as adsorbent and helium or hydrogen as carrier gas. The two gases are mixed in a certain proportion to reach the specified relative pressure, and then flow through solid substances. When the sample tube is put into liquid nitrogen for insulation, the sample physically adsorbs the nitrogen in the mixed gas, while the carrier gas is not adsorbed. At this time, the

adsorption peak appears on the screen. When the liquid nitrogen is removed, the sample tube is at room temperature again, and the adsorbed nitrogen is desorbed, and the desorption peak appears on the screen. Finally, a corrected peak is obtained by injecting a known volume of pure nitrogen into the mixture. According to the peak areas of the correction peak and desorption peak, the adsorption capacity of the sample under this relative pressure can be calculated. By changing the mixing ratio of nitrogen and carrier gas, the adsorption capacity of several nitrogen under relative pressure can be measured, so the specific surface area can be calculated according to bet formula. A solid has a certain geometric shape, and its surface area can be obtained by means of common instruments and calculations. However, it is difficult to determine the surface area of powder or porous materials. They not only have irregular outer surfaces, but also complex inner surfaces. The measurement of specific surface area is of great significance in both scientific research and industrial production.

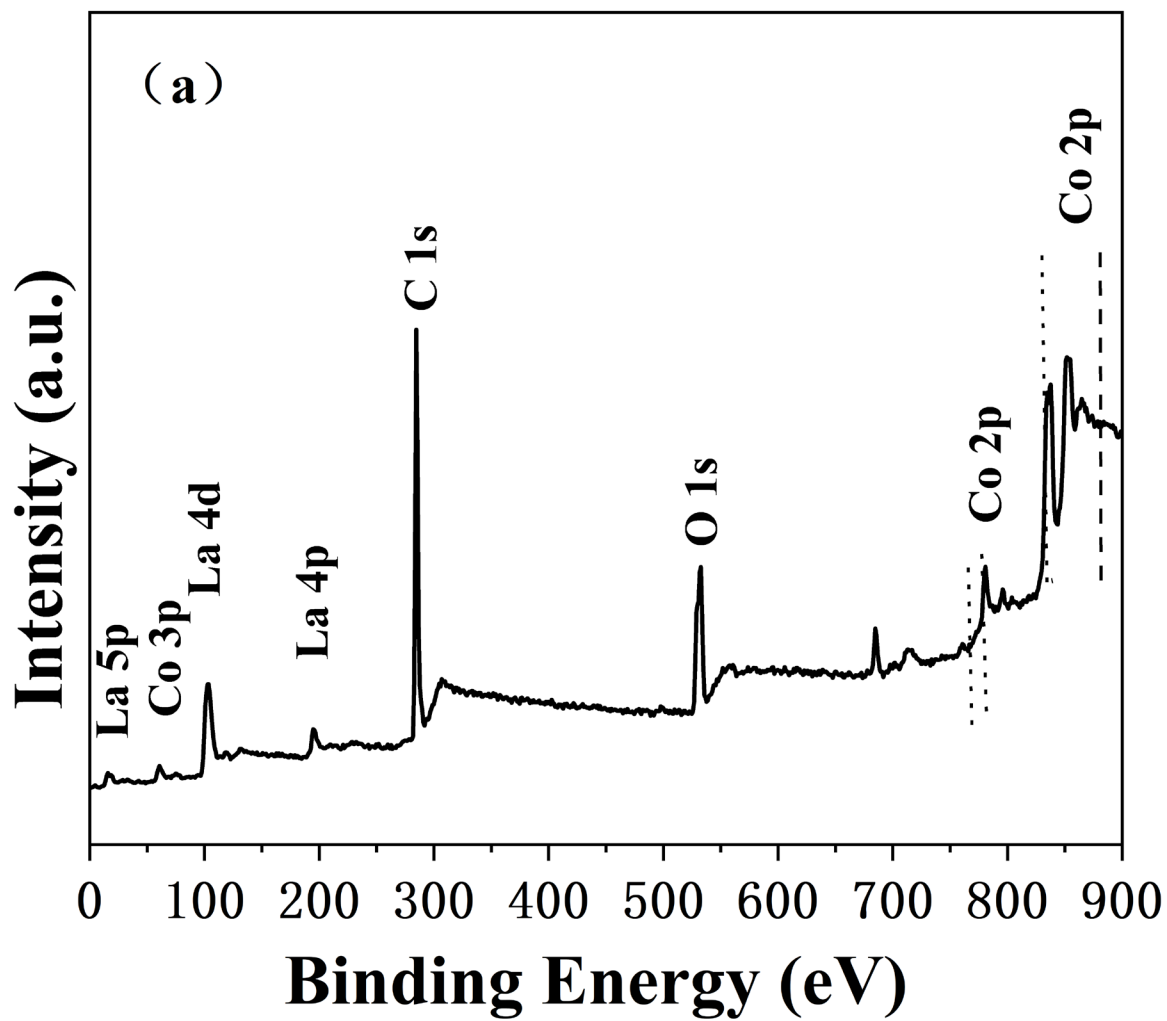The BET specifific surface (S_{BET}) of g-C_3N_4, LaCoO$_3$, and LaCoO$_3$/ g-C_3N_4,

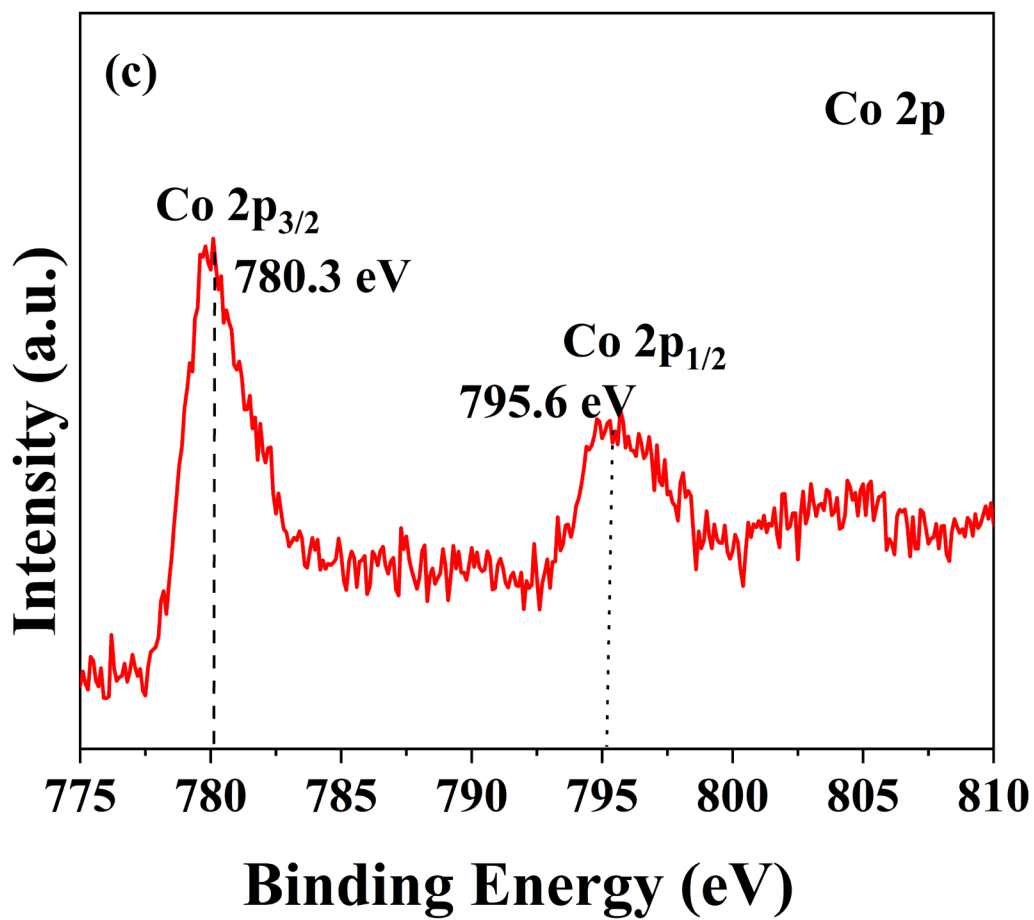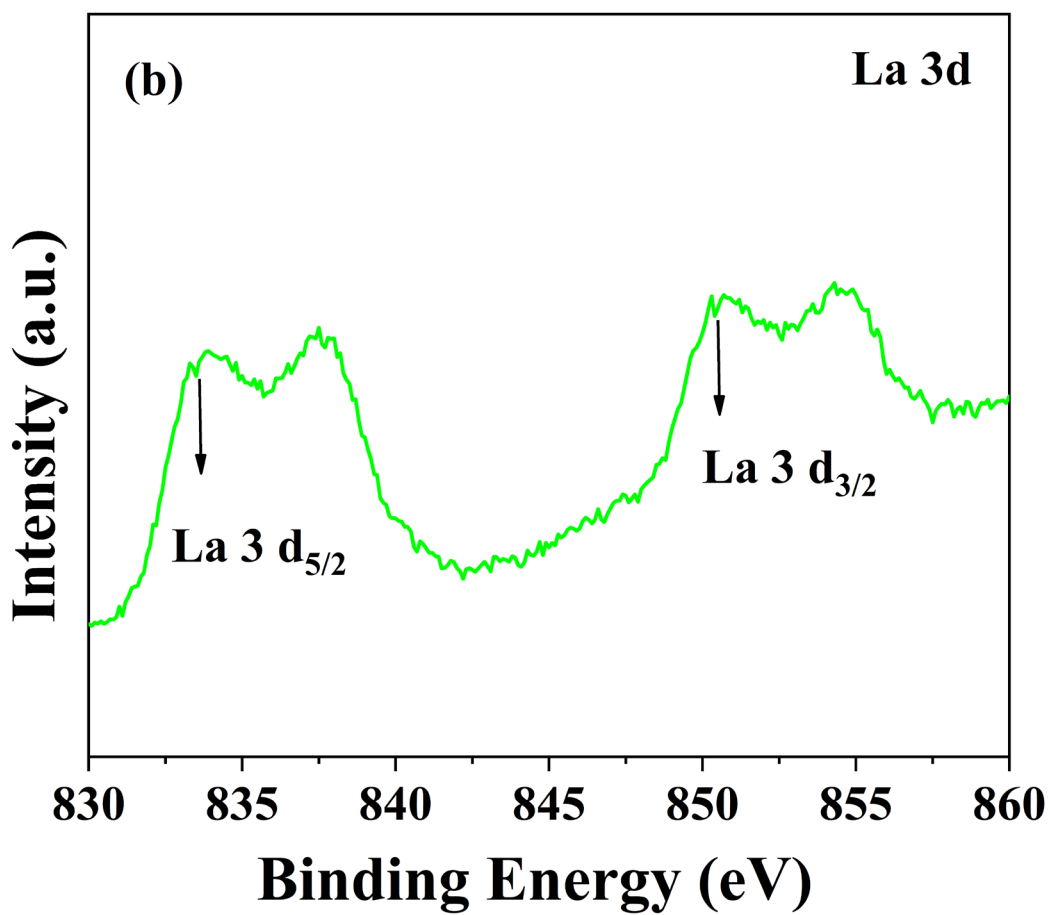| Sample	$S_{BET(m^2/g)}$
g-C_3N_4	40.3794
LaCoO$_3$	3.2839
LaCoO$_3$/ g-C_3N_4	5.8048

As shown in Table 1, the specific surface area of LaCoO$_3$/C_3N_4 is slightly higher than that of pure LaCoO$_3$. This means that when adding PMS solution, there will be more active sites to participate in the reaction. At the same time, the rate of $SO_4^{•-}$, $^1O_2$ and OH• will be faster and the degradation rate will be greatly improved. Generally speaking, increasing the specific surface area, pore volume and pore diameter of the
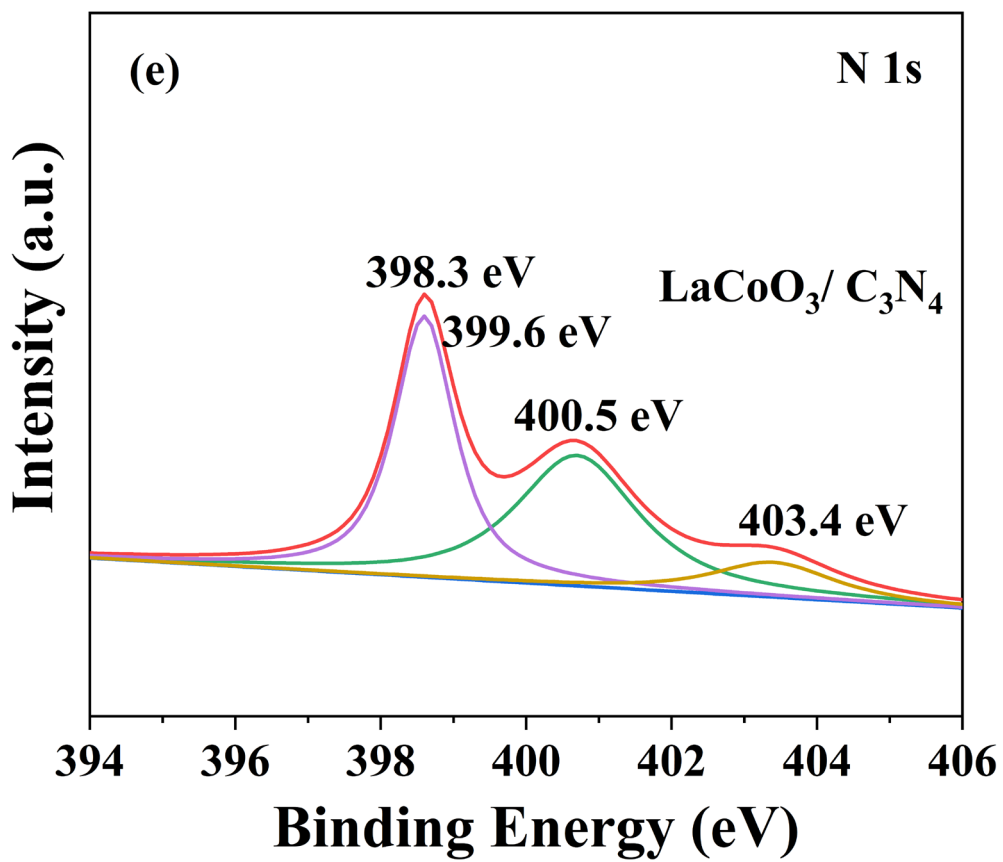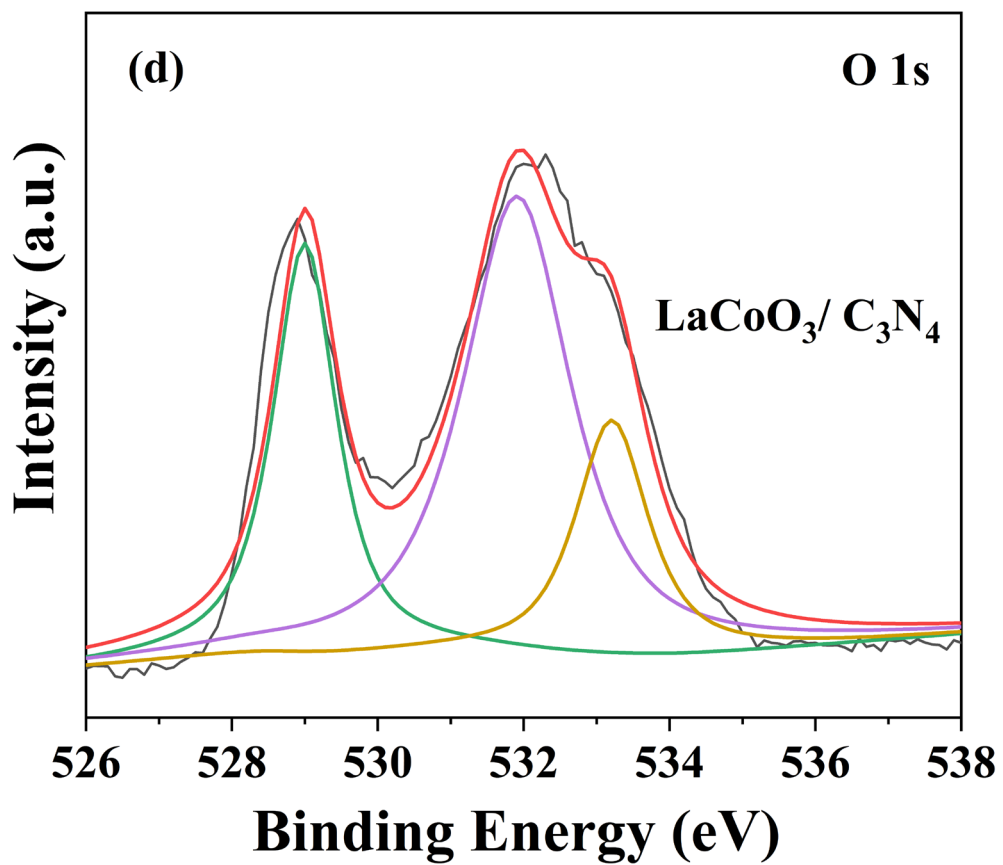
catalyst is conducive to improving the catalytic performance of the material.

3.1.5 X-ray photoelectron spectroscopy

XPS, fully known as X-ray photoelectron spectroscopy, was also known as ESCA (electron spectroscopy for chemical analysis) in the early stage. It is a method to measure the energy distribution of photoelectrons and Auger electrons emitted from the sample surface when X-ray photons are irradiated by an electron spectrometer. The principle of XPS is to radiate the sample with X-rays to excite the inner electrons or valence electrons of atoms or molecules. Electrons excited by photons are called photoelectrons. The photoelectron energy can be measured. The photoelectron spectrum can be made with the photoelectron kinetic energy/binding energy as the abscissa and the relative intensity as the ordinate. In order to obtain information about the sample, XPS can be used for qualitative analysis and semi quantitative analysis. Generally, the information of sample surface element composition, chemical state and molecular structure can be obtained from the peak position and peak shape of XPS spectrum, and the content or concentration of sample surface element can be obtained from the intensity of peak. X-ray photoelectron spectroscopy (XPS) is a conventional surface composition analysis technology. It can not only characterize the composition of materials, but also characterize the chemical state of each component, and quantitatively characterize the relative content of each component; Therefore, XPS is widely used in various fields of material research.
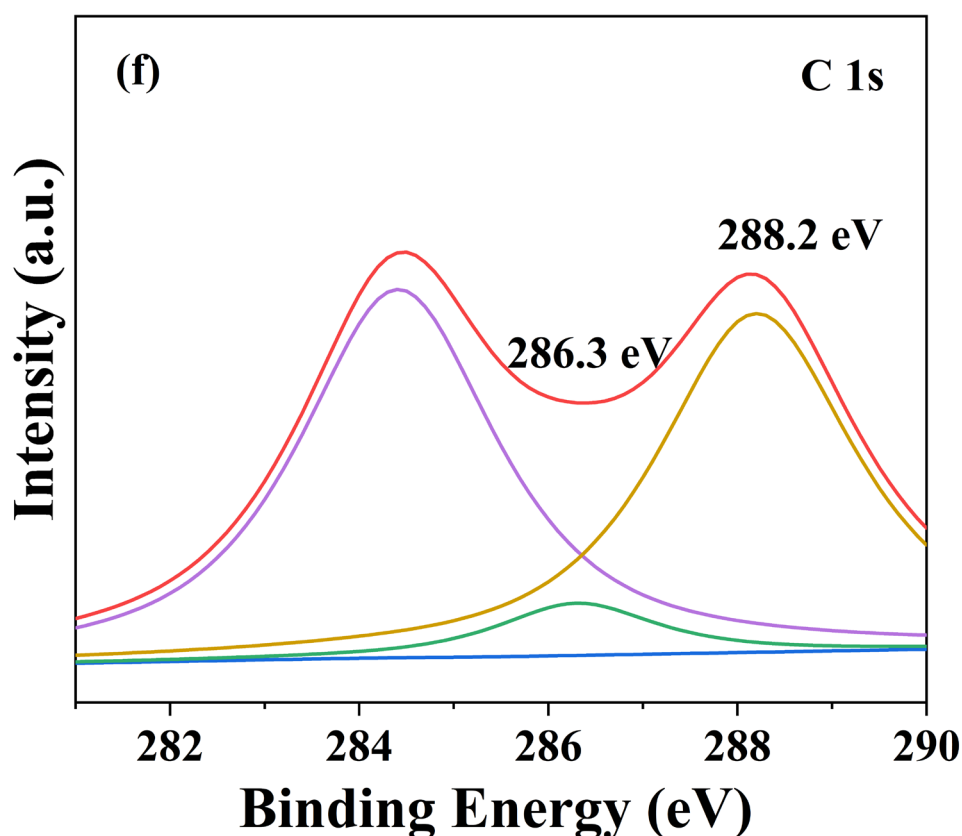
(a)

Intensity (a.u.)

Binding Energy (eV)

La 5p
Co 3p
La 4d
La 4p
C 1s
O 1s
Co 2p
Co 2p

(d) O 1s

LaCoO$_3$/ C$_3$N$_4$

(e) N 1s

398.3 eV
399.6 eV
400.5 eV
403.4 eV

LaCoO$_3$/ C$_3$N$_4$

Fig. 3-4.(a) XPS survey spectra of LaCoO$_3$/ g-C$_3$N$_4$, High resolution XPS spectraof (b) La 3d, (c) Co 2p, (d) O 1s, (e) N 1s, (f) C 1s in corresponding sample

The surface chemical composition and elemental chemical states of the samples were analyzed by XPS technique. Figure 3-4 (a) shows the XPS measurement spectrum of LaCoO$_3$/g-C$_3$N$_4$ composite material. The LaCoO$_3$/g-C$_3$N$_4$ composite was composed of La, Co, O, C and N elements, and the typical high-resolution XPS spectra of La 3D showed satellite peaks. Figure 3-4(b) The peaks of La 3d$_{5/2}$ and La 3d$_{3/2}$ are split into two components by about 4 eV, due to the transfer of electrons from the oxygen valence band to an empty La 4f orbital accompanied by ionization. In addition, the XPS spectrum of lanthanum confirms that all lanthanum ions exist in the form of La^{3+}. The high resolution XPS spectra of Co 2p in Figure 3-4(c) show two main peaks corresponding to Co 2p$_{3/2}$ (779.8 eV) and Co 2p$_{1/2}$ (795.2 eV) levels respectively, which

are close to the values reported in the literature indicating that all cobalt ions exist in the form of Co^{3+}. In addition, O1s XPS spectra (Figure 3-4(d)) show two main features at 529.0 eV and 531.3 eV. The lower peak (about 529.0 eV) is the attribution of surface lattice oxygen atoms, the second peak (about 531.2 eV) is the attribution of hydroxyl oxygen, and the third peak (about 533.1 eV) is the attribution of surface adsorbed oxygen. The presence of hydroxyl oxygen and the adsorbed oxygen will produce a large number of hydroxyl radicals, which will contribute to increased activity. As shown in Figure 3-4(e), peak N 1s at 398.6 eV belongs to CN single bond, and peak g at 399.6 eV belongs to sp^2 CN double bond. The peak at 400.5eV belongs to the amorphous CN network surrounded by three carbons ($N-(C)_3$). The weak peak at 404.3 eV may be caused by π excitation. The peak at 284.6eV belongs to the C-C bond of CN structure in the turbulent layer, the peak at 286.4eV belongs to the sp^2 CN bond, and the peak at 288.1eV is attached to the sp^3 CN bond. Therefore, XPS results showed that $LaCoO_3$ coexisted with $g-C_3N_4$.
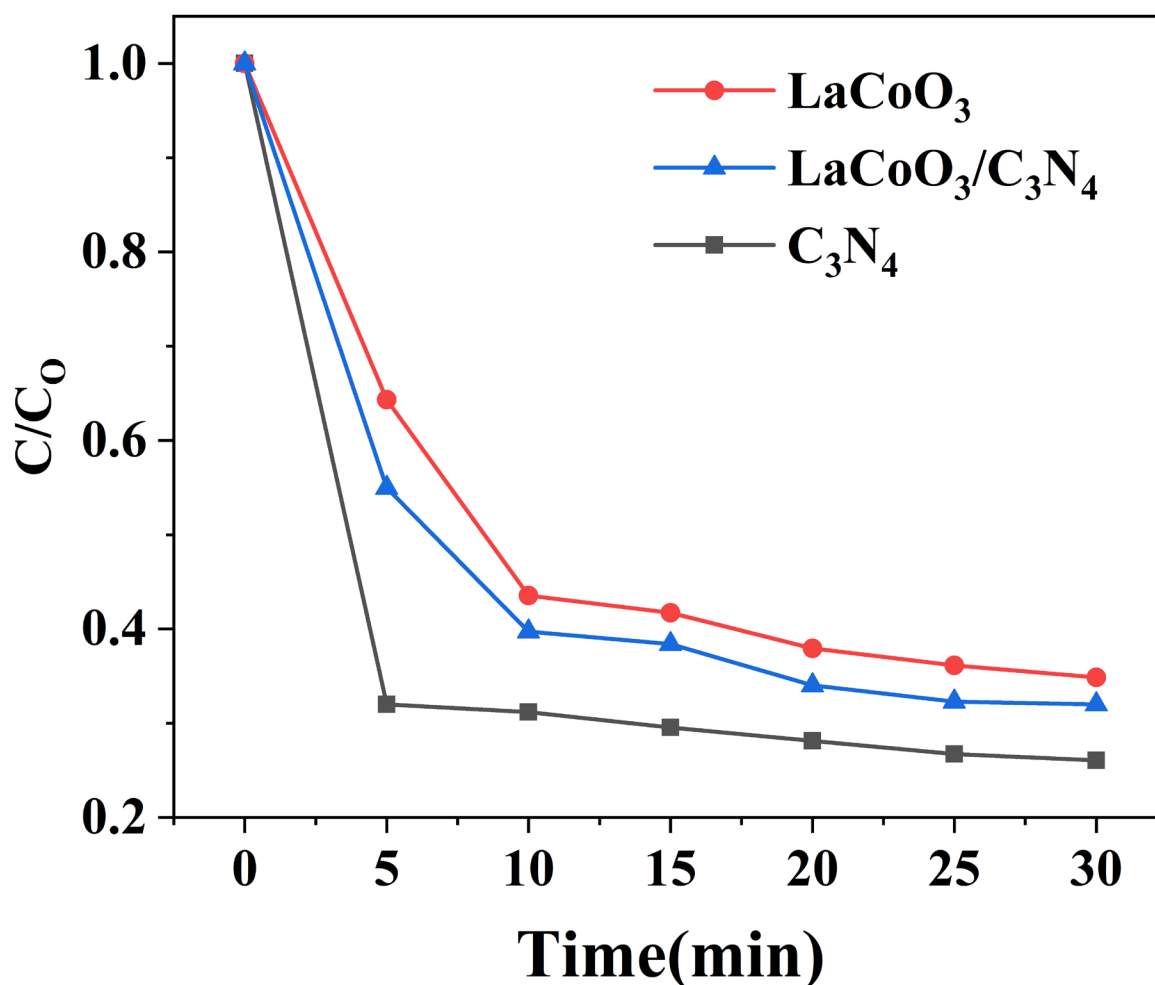
3.2 Catalytic performance of different catalysts

Fig. 3-5. Catalytic degradation of TC using different catalysts.

Reaction conditions: $[TC]_0 = 20$ mg·L^{-1}, $[PMS]_0 = 0.1$ g/L, $[catalyst]_0 = 0.2$ g·L^{-1}, pH = 7.0, and T = 25 °C

Figure 3-5 shows the degradation rate of tetracycline hydrochloride at different times in different catalyst systems. It can be seen from the Figure 1 that the degradation efficiency of TC by $LaCoO_3/C_3N_4$ activated PMS is higher than that of pure $LaCoO_3$. There may be two reasons. One is that the specific surface area of $LaCoO_3/C_3N_4$ is slightly larger than $LaCoO_3$. When PMS activation occurs, $LaCoO_3/C_3N_4$ can provide more active sites to participate in free radical activation reaction at the same time. Secondly, $LaCoO_3$ and C_3N_4 may have synergistic effect or form Z-shaped

heterojunction, which improves the PMS activation to degrade TC. C_3N_4 shows high degradation effect because the specific surface area of C_3N_4 is much larger than $LaCoO_3$ and $LaCoO_3/C_3N_4$, and the number of PMS activation sites provided by C_3N_4 is much larger than $LaCoO_3$ and $LaCoO_3/C_3N_4$ at the same time. Therefore, pure C_3N_4 has the best effect on TC degradation.
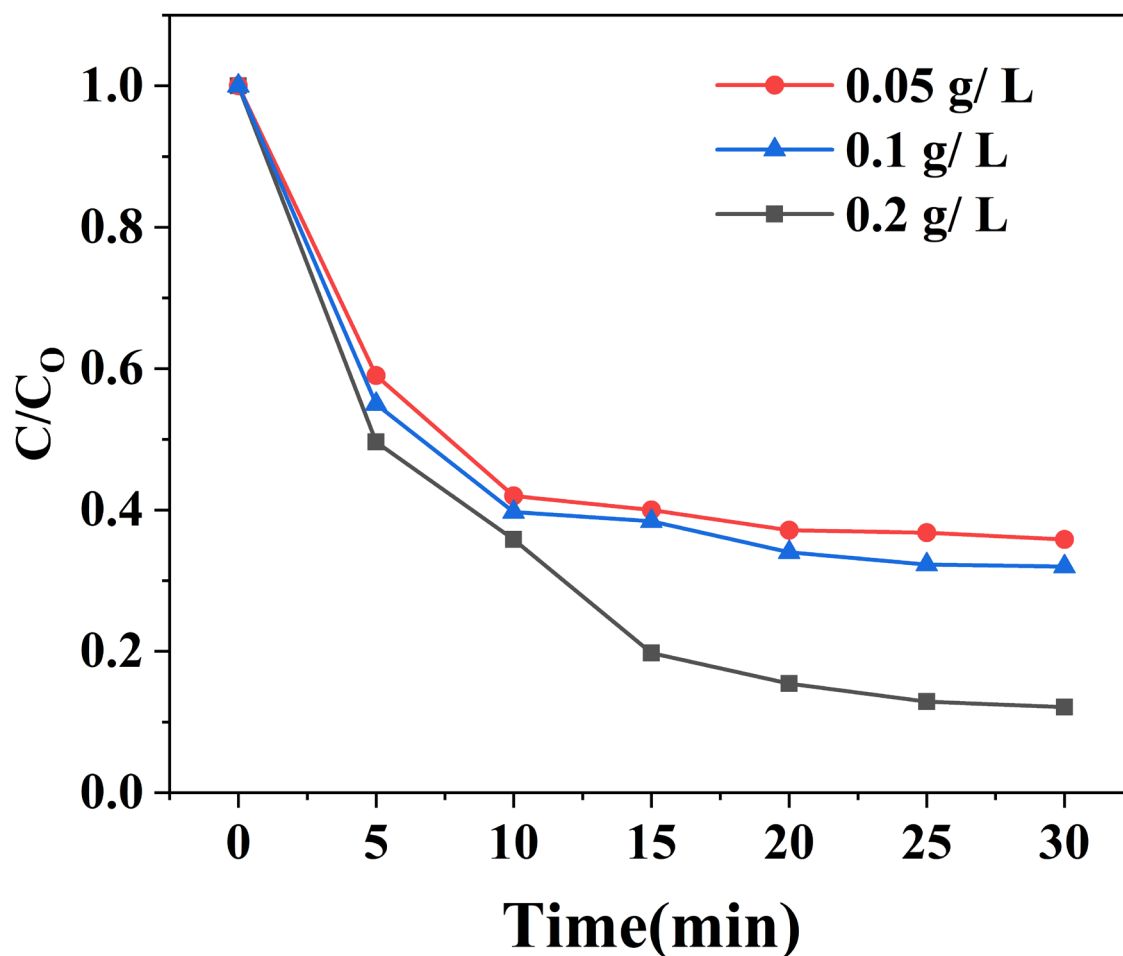
Fig. 3-6. Effect of PMS concentration on TC degradation in $LaCoO_3/C_3N_4$/PMS system: Reaction conditions: $[TC]_0 = 20$ mg·L^{-1}, $[catalyst]_0 = 0.2$ g·L^{-1}, pH = 7.0, and T = 25 °C

Fig. 3-6 shows the effects of different PMS concentrations on the degradation of tetracycline hydrochloride in $LaCoO_3/C_3N_4$/PMS system. With the increase of PMS concentration in the reaction system, the degradation rate of tetracycline hydrochloride increased gradually. When the concentration of PMS in the reaction system increased to 0.2 g/L^{-1}, 89% of TC could be removed within 30 minutes. The reason for this

phenomenon may be that more and more active species are activated with the increase of PMS concentration. When the PMS concentration increased to 0.2 g/L^{-1}, the excess PMS produced SO$_5$•$^-$ with lower activity, thereby reducing the production of SO$_4$•$^-$. At the same time, when more and more PMS in the reaction system are activated to produce excessive SO$_4$•$^-$, the self quenching reaction will occur [64], see formulas 1 and 2.

$$HSO_5^- + SO_4\bullet^- \rightarrow HSO_4^- + SO_5^{\bullet-} \qquad 3\text{-}1$$

$$SO_4\bullet^- + SO_4\bullet^- \rightarrow S_2O_8^{2-} \qquad 3\text{-}2$$
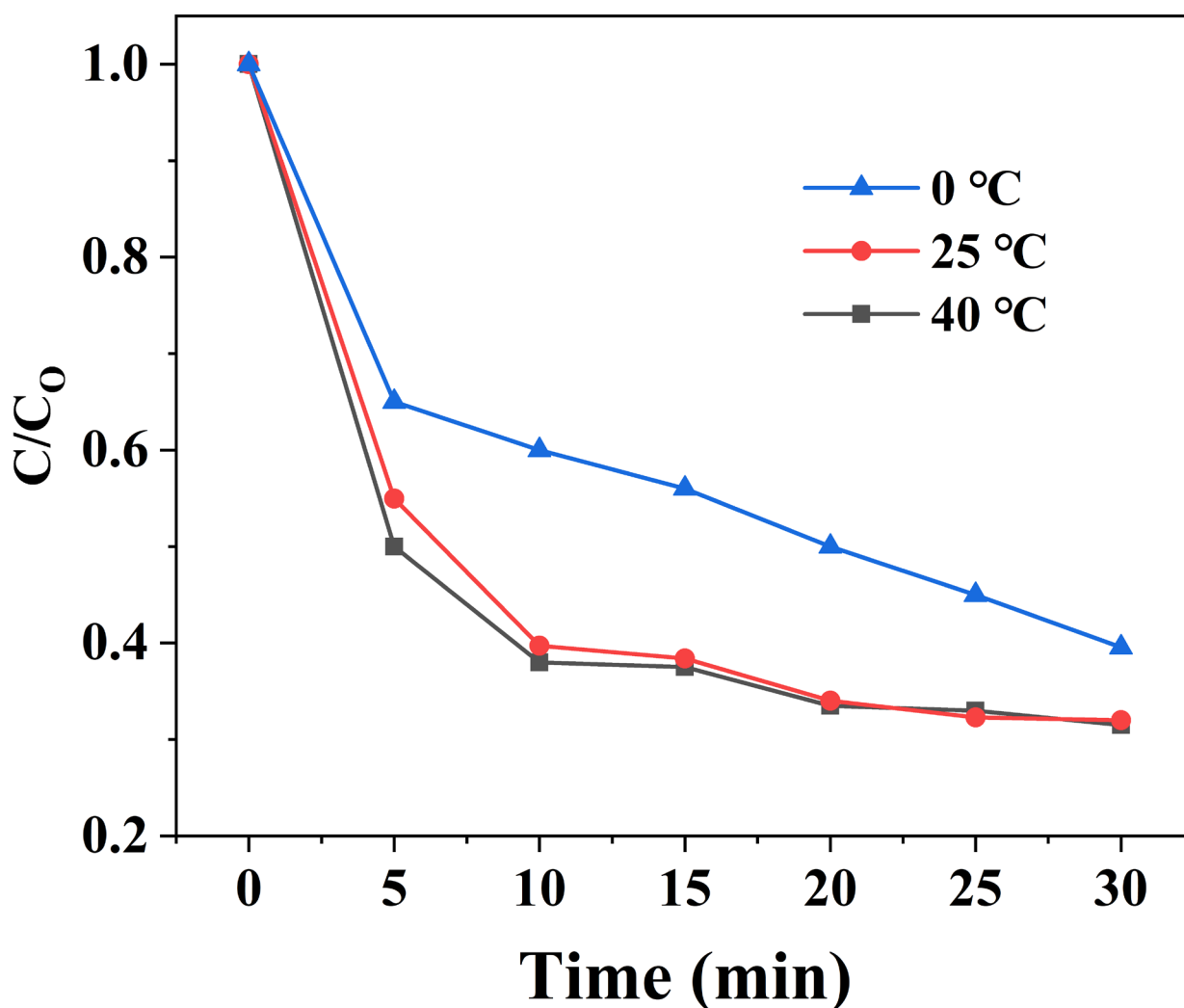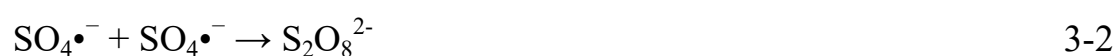
Fig. 3-7. Effect of reaction temperature on TC degradation in LaCoO$_3$/C$_3$N$_4$/PMS system Reaction conditions: [TC$_0$ = 20 mg·L^{-1}, [PMS]$_0$ = 0.1 g/L, [catalyst]$_0$ = 0.2 g·L^{-1}, and pH = 7.0

Temperature is the key factor affecting the degradation of TC by activated PMS. Fig. 3-7 is a schematic diagram of the degradation rate of TC with temperature. It can be seen from the figure that $LaCoO_3/C_3N_4$ catalyst can effectively remove TC in a wide temperature range, and has a very good catalytic degradation effect even at 0 ^{o}C. The activation of PMS is endothermic reaction. With the increase of temperature from 25 ^{o}C to 40 ^{o}C, the reaction rate constant K also increases gradually, which improves the reaction rate. At the same time, the reaction temperature increased, the internal motion of the molecule intensified, and the reaction between $LaCoO_3/C_3N_4$ and PMS accelerated. Moreover, the increase of temperature can also promote cation leaching, so as to activate more $SO_4^{•-}$. High temperature can promote the activation of PMS, but high temperature will also increase the solubility of organic matter, which is not conducive to the separation of organic matter.
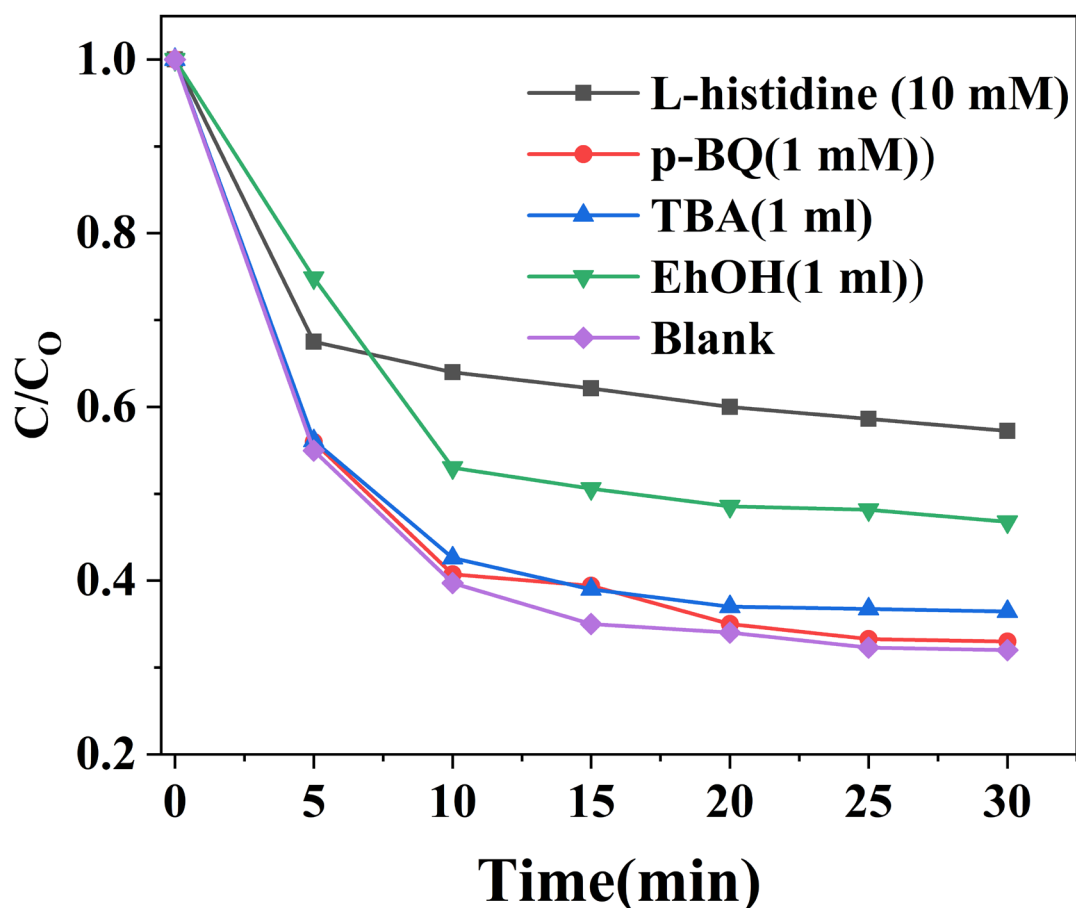
Fig. 3-8. Effect of radical scavengers addition on TC degradation in LaCoO$_3$/C$_3$N$_4$/PMS system. Reaction conditions: $[TC]_0 = 20$ mg·L^{-1}, $[PMS]_0 = 0.1$ g/L, $[catalyst]_0 = 0.2$ g·L^{-1}, pH = 7.0, and T = 25 °C

LaCoO$_3$/C$_3$N$_4$ catalyst shows good performance in PMS activation and degradation of tetracycline hydrochloride, hence it is very necessary to study the PMS activation mechanism of LaCoO$_3$/C$_3$N$_4$ catalyst. In order to explore the main active substances in the reaction process, as shown in Figure 3-8, we carried out free radical quenching experiment. Ethanol can quench SO$_4$•$^-$ and •OH, and tert butanol and L-histidine can be used as free radical scavengers of •OH and ^{1}O$_2$, respectively. When 10 mm TBA, 10 mm L-histidine and 10 mM ethanol were added to the reaction system, the TC degradation rate decreased to 64%, 43% and 54% within 30 min. It is obvious that ethanol and histidine have more obvious inhibitory effects on TC degradation than the

effect of TBA, indicating that free radical pathway ($SO_4 \cdot^-$) and non free radical pathway ($^1O_2$) play a very important role in the degradation of TC.
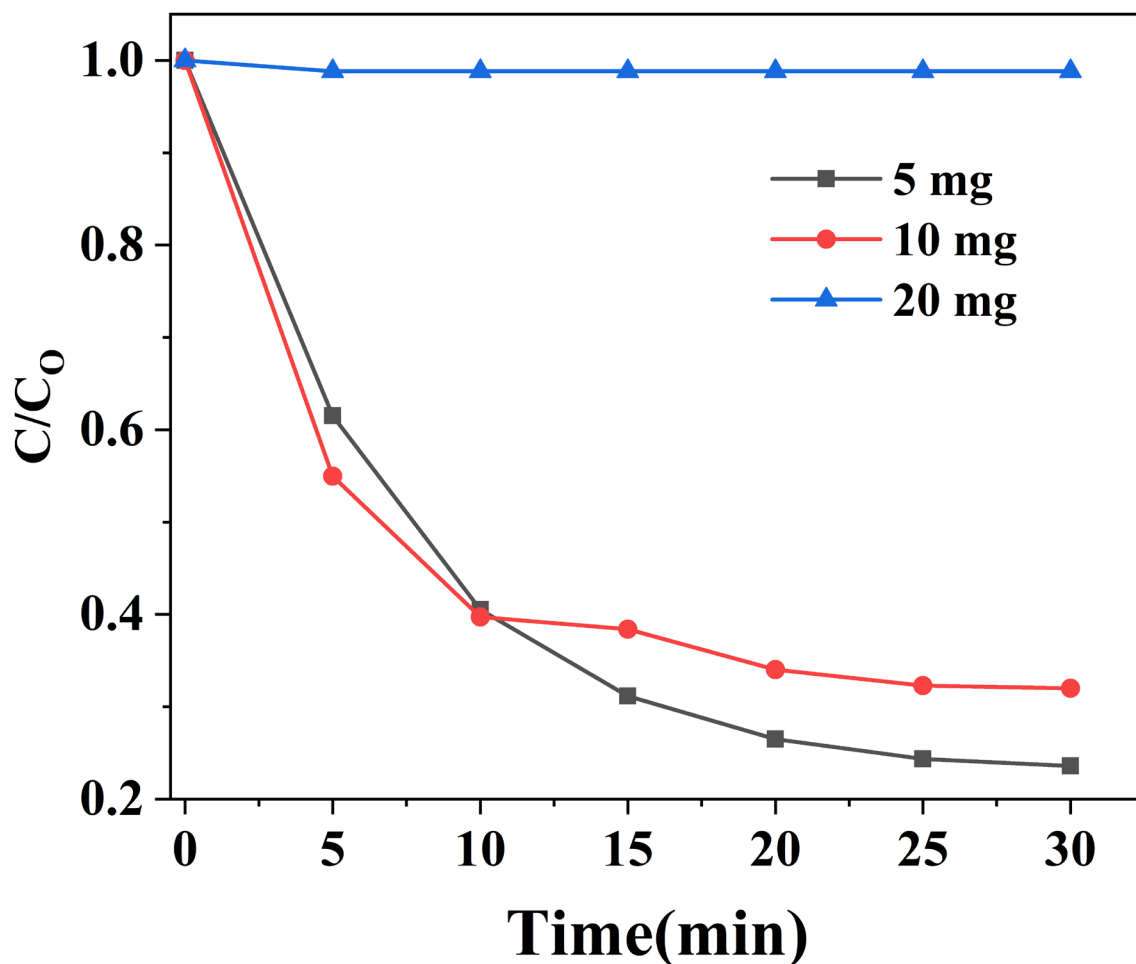
Fig. 3-9. Effect of catalyst concentration on TC degradation in $LaCoO_3/C3N_4/PMS$ system: $[PMS]_0 = 0.1$ g/L, $[catalyst]_0 = 0.2$ g·L^{-1}, pH = 7.0, and T = 25 °C

Fig. 3-9 shows the effect of catalyst $LaCoO_3/C_3N_4$ dosage on the degradation rate of tetracycline hydrochloride. The dosage of $LaCoO_3/C_3N_4$ can affect the degradation rate of TC. When the dosage in the reaction system is 10 mg, after 30 min, the removal rate of TC reaches more than 69%, while when the dosage in the reaction system is 5 mg, the removal rate of TC reaches more than 78%. However, when the dosage in the reaction system was 20 mg, it was difficult to drive the degradation of TC after 30 min.

Therefore, the excess catalyst LaCoO$_3$/C$_3$N$_4$ inhibited the activation of PMS and the degradation of TC. Therefore, we only need a small amount of catalyst to effectively remove organic pollutants from water. This result is obviously attributed to the increase of active sites on the surface of LaCoO$_3$/C$_3$N$_4$, which produces more free radicals to overcome some functional groups of pollutants and degrade pollutants.
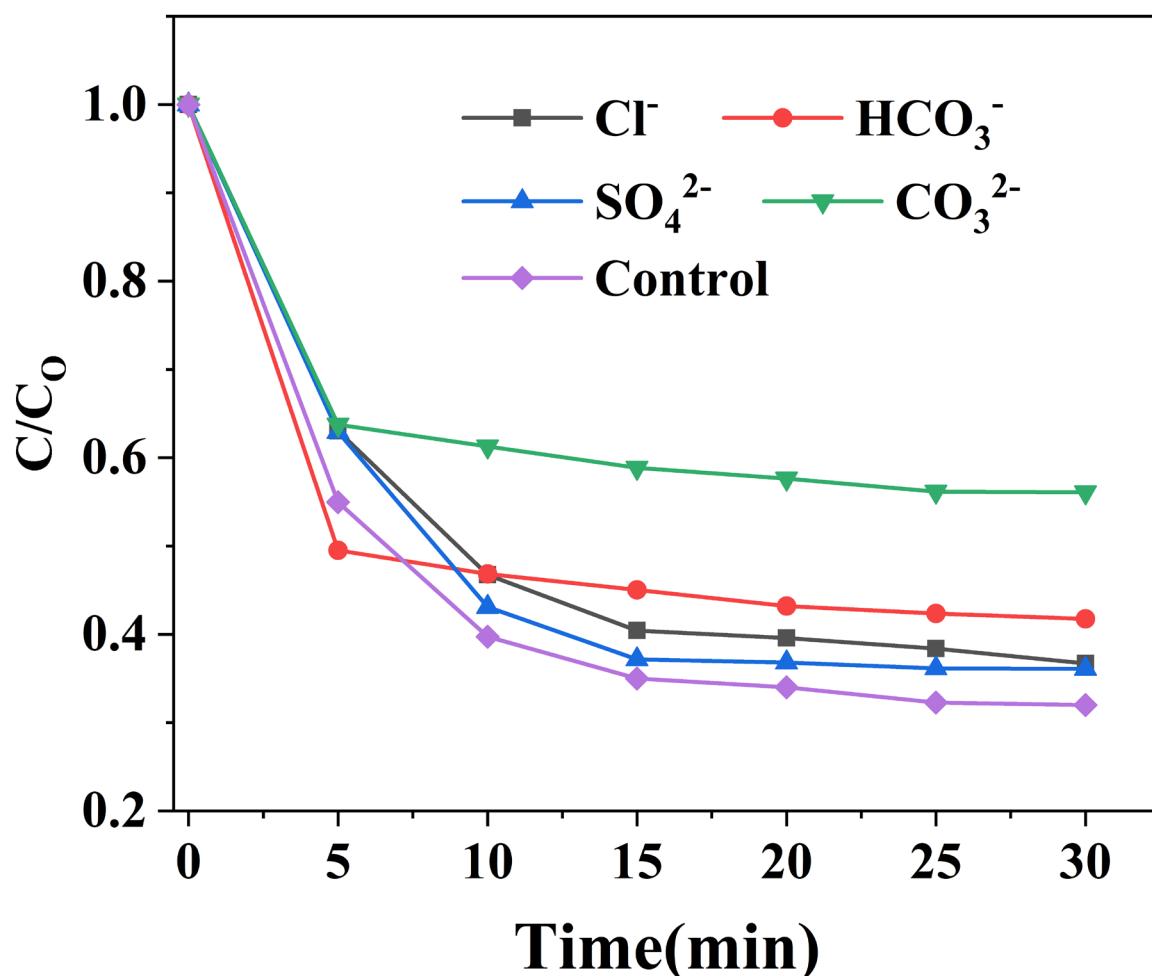
Fig. 3-10. Effect of reaction conditions on TC degradation in LaCoO$_3$/C$_3$N$_4$/PMS system: at inorganic anions (10 mm)

Reaction conditions: [TC]$_0$ = 20 mg·L^{-1}, [PMS]$_0$ = 0.1 g/L, [catalyst]$_0$ = 0.2 g·L^{-1}, pH = 7.0, and T = 25 °C

In order to evaluate the effects of different inorganic anions on the catalytic degradation of organic pollutants, several inorganic salts were dissolved in LaCoO$_3$/C$_3$N$_4$/PMS system. As shown in Figure 3-10, after adding 10 mm Na$_2$SO$_4$, 10

mM NaCl, 10 mm NaHCO$_3$ and 10 mm Na$_2$CO$_3$, the removal rate of TC in LaCoO$_3$/C$_3$N$_4$/PMS system decreased from 68% to 64%, 63%, 59% and 44%. It can be seen from formulas 3-3 and 3-4 that the presence of Cl$^-$ will react with SO$_4$•$^-$ to form Cl• and Cl$_2$•$^-$ (E^0 (Cl•/Cl$^-$) = 2.4 V; E^0 (Cl$_2$•/2Cl$^-$) = 2.1 V), resulting in a slight decrease in catalytic performance. CO$_3$$^{2-}$ and HCO$_3$$^-$ have a great inhibitory effect on the removal efficiency of TC. This is because CO$_3$$^{2-}$ and HCO$_3$$^-$ can react with •OH and SO$_4$•$^-$ to produce other active substances with low redox potential (see formulas 3-5 to 3-8).

$$Cl^- + SO_4\bullet^- \rightarrow Cl\bullet + SO_4^{2-} \qquad\qquad 3\text{-}3$$

$$Cl^- + Cl\bullet \rightarrow Cl_2\bullet^- \qquad\qquad 3\text{-}4$$

$$SO_4\bullet^- + CO_3^{2-} \rightarrow SO_4^{2-} + CO_3\bullet^- \qquad\qquad 3\text{-}5$$

$$\bullet OH + CO_3^{2-} \rightarrow OH^- + CO_3\bullet^- \qquad\qquad 3\text{-}6$$

$$SO_4\bullet^- + HCO_3^- \rightarrow SO_4^{2-} + HCO_3\bullet \qquad\qquad 3\text{-}7$$

$$\bullet OH + HCO_3^- \rightarrow CO_3\bullet^- + H_2O \qquad\qquad 3\text{-}8$$
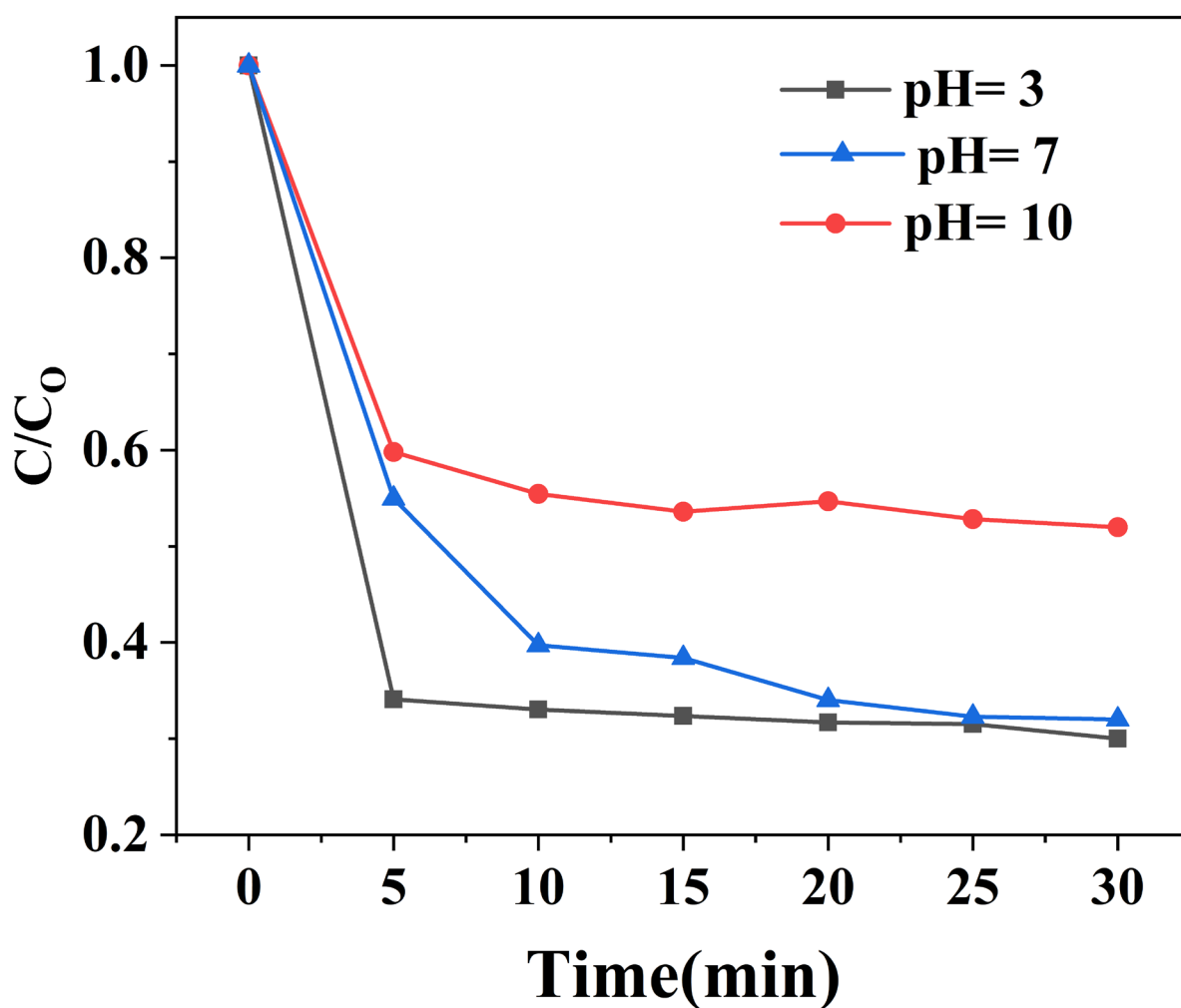
Fig. 3-11. Effect of pH on TC degradation in $LaCoO_3/C_3N_4/PMS$ system: at pHs

Reaction conditions: $[TC]_0 = 20$ mg·L^{-1}, $[PMS]_0 = 0.1$ g/L, $[catalyst]_0 = 0.2$ g·L^{-1}, and T = 25 °C

In the process of catalytic degradation, the pH of the solution plays an important role in the formation of free radicals and the degradation of pollutants. As shown in Figure 3-11, the effect of initial pH on TC degradation was explored in the range of pH = 3 ~ 10. Under the reaction conditions of initial pH 3, 7 and 10, the removal rates of TC by $LaCoO_3/C_3N_4$ catalyst were 69%, 68% and 48%, respectively. The experimental results show that $LaCoO_3/C_3N_4$ has the best removal effect on TC under acidic conditions. In addition, pH value can affect the decomposition of PMS to produce free radicals. When pH increases, the oxidation ability of Co^{2+} is inhibited, resulting in the reduction of the kinetic constant of TC degradation. In addition, when the pH value

increases to 9, the PMS becomes unstable. It can be decomposed into SO_5^{2-}, which can react with PMS to produce singlet oxygen. As shown in formula 3-9, the reactivity of singlet oxygen with TC is low. When pH = 10, the alkalinity of TC solution is strong, so it can be seen that alkaline conditions have a great influence on the degradation rate of TC. The reason may be that under alkaline conditions, OH^- will be oxidized to $\cdot OH$ by $SO_4\cdot^-$ produced in $LaCoO_3/C_3N_4$ system. However, the lifetime of $\cdot OH$ (< 1 μ s) is much shorter than the lifetime of $SO_4\cdot^-$ radical (30 ~ 40 μ s). And the redox potential of $\cdot OH$ (1.8 ~ 2.7 V vs NHE) is lower than that of $SO_4\cdot^-$ (2.5 ~ 3.1 vs NHE), so the degradation rate of TC is reduced, as shown in formula 3-10.

$$SO_5^{2-} + HSO_5^- \rightarrow {}^1O_2 + SO_4^{2-} + H^+ \hspace{4cm} \text{3-9}$$

$$SO_4\cdot^- + OH^- (\text{or } H_2O) \rightarrow SO_4^{2-} + \cdot OH (H^+) \hspace{2.5cm} \text{3-10}$$
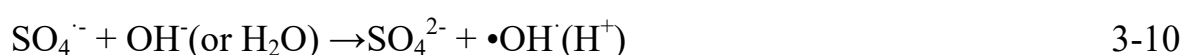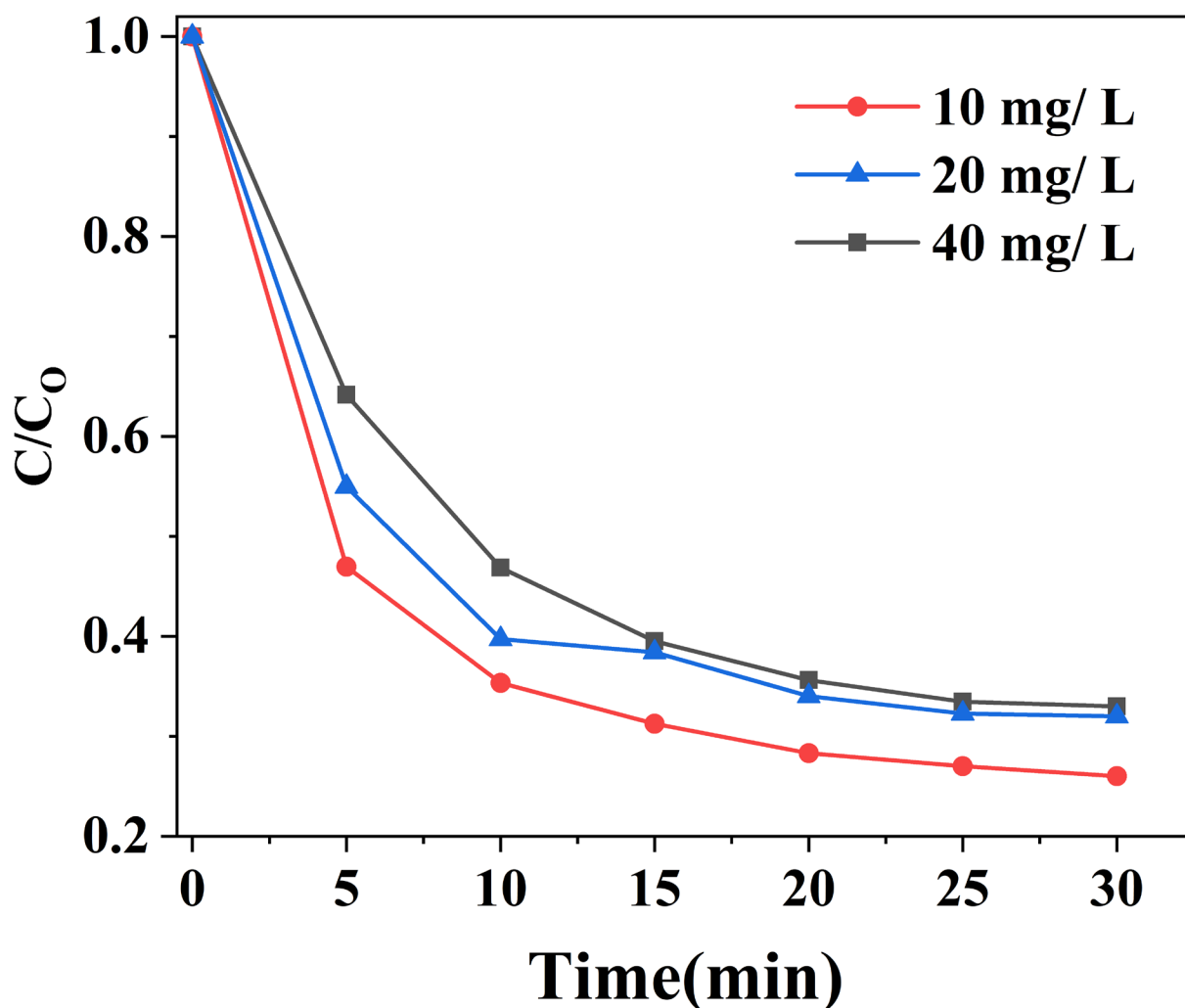
Fig. 3-12. Effect of TC concentration on TC degradation in LaCoO$_3$/C$_3$N$_4$/PMS system. Reaction conditions: [TC]$_0$ = 20 mg·L^{-1}, [PMS]$_0$ = 0.1 g/L, [catalyst]$_0$ = 0.2 g·L^{-1}, pH = 7.0, and T = 25 °C

As shown in Figure 3-12, the effect of different concentrations of tetracycline hydrochloride on the degradation effect was explored. The data show that the degradation efficiency of LaCoO$_3$/C$_3$N$_4$/PMS is 68% within 30 min of 40 mg/L tetracycline hydrochloride, that of LaCoO$_3$/C$_3$N$_4$/PMS is 69% within 30 min of 20 mg/L tetracycline hydrochloride, and that of LaCoO$_3$/C$_3$N$_4$/PMS is 74% within 30 min of 20 mg/L tetracycline hydrochloride, indicating that the degradation efficiency decreases with the increase of the concentration of tetracycline hydrochloride, The concentration of pollutants increases because the ability of PMS to activate the catalyst is limited and the number of active sites provided by the catalyst is certain, that is, the degradation of

some specific functional groups in organic pollutants is limited at the same time. Therefore, the higher the concentration of tetracycline hydrochloride, the worse the PMS activation for TC degradation.

3.3 The reaction mechanism

Electron paramagnetic resonance (EPR) is a magnetic resonance technology originated from the magnetic moment of unpaired electrons. It can be used to detect the unpaired electrons contained in material atoms or molecules qualitatively and quantitatively, and explore the structural characteristics of their surrounding environment. There are two main detection objects: 1) substances with unpaired electrons (or single electrons) in molecular orbitals. For example, free radicals (molecules containing one single electron), double radicals and multi radicals (molecules containing two or more single electrons), triplet molecules (molecules also have two single electrons in the molecular orbital, but they are very close to each other and have strong magnetic interaction, which is different from double radicals). 2) substances with one electron in the atomic orbital, such as alkali metal atoms Transition metal ions (including iron group, palladium group and platinum group ions, which successively have unfilled 3D, 4D and 5D shells) and rare earth metal ions (with unfilled 4f shells). The vast majority of instruments work in the microwave region, usually using a fixed microwave frequency and changing the magnetic field strength H to achieve the resonance condition. In addition, EPR is the only research method that can directly track unpaired electrons. Therefore, EPR technology is widely used in the field of catalysis.
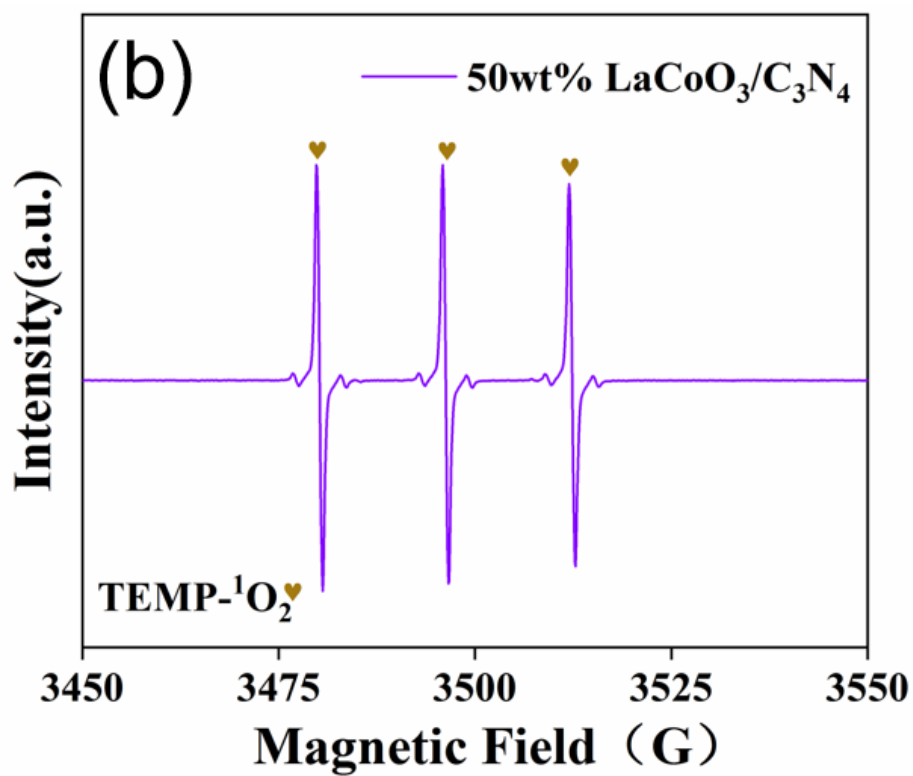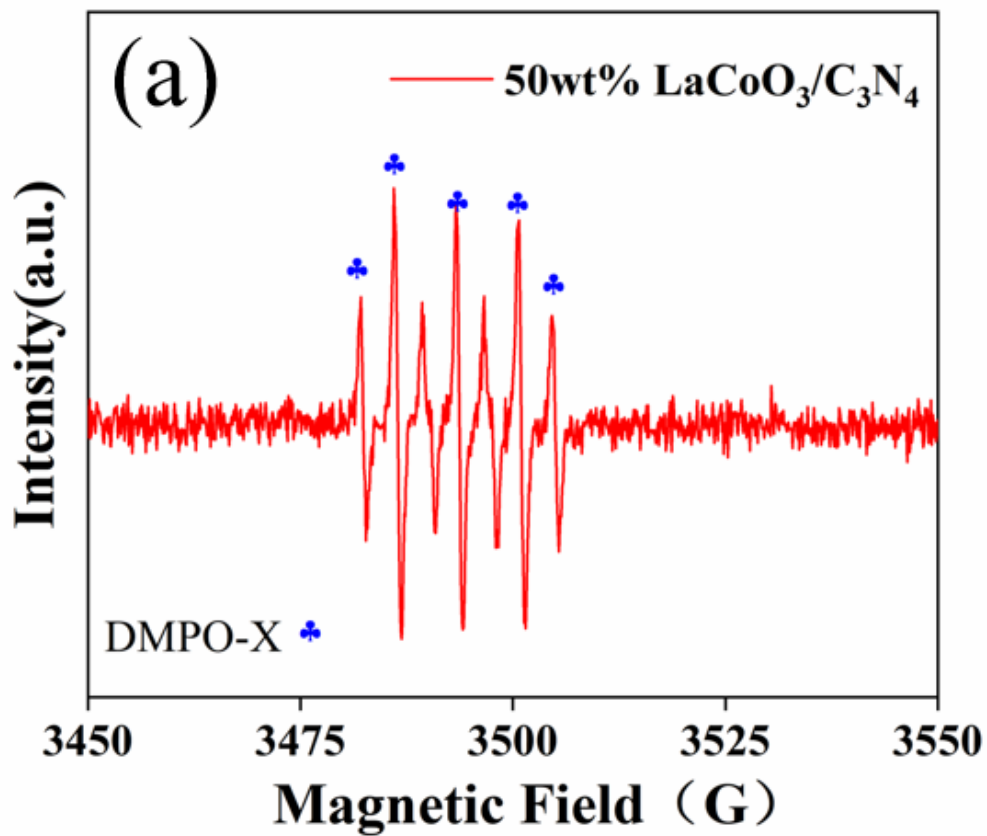
Fig. 3-13. (a)EPR spectra of PMS activation in DMPO solutions by PMS and LaCoO$_3$/C$_3$N$_4$+ PMS

(b)EPR spectra of PMS activation in TEMP solutions by PMS and LaCoO$_3$/C$_3$N$_4$+ PMS

Reaction conditions: [TC]$_0$ = 20 mg·L^{-1}, [PMS]$_0$ = 0.1 g/L, [catalyst]$_0$ = 0.2 g·L^{-1}, pH = 7.0, and T = 25 °C

In order to further prove the types of reactions involved, we also carried out electron paramagnetic resonance (EPR) experiments using spin trapping agents DMPO and temp. EPR signals of DMPO-X and TEMP-^{1}O$_2$ adducts can be detected in LaCoO$_3$/g-C$_3$N$_4$/PMS/TC system, indicating that SO$_4$•$^-$. And ^{1}O$_2$ are the main reaction species in LaCoO$_3$/g-C$_3$N$_4$/PMS system. As shown in Figure 3-13 (a), seven representative peaks can be observed in LaCoO$_3$/g-C$_3$N$_4$/PMS/TC system, which can be attributed to DMPO-X, indicating that PMS can produce free radical species with strong oxidation ability (including SO$_4$•$^-$ and OH•) by activating LaCoO$_3$/g-C$_3$N$_4$ catalyst. The appearance of DMPO-X usually confirms the species of free radicals, resulting in the rapid oxidation of DMPO. Using TEMP as the spin trapping agent of ^{1}O$_2$, a representative signal with an intensity ratio of 1:1:1 was observed in the figure. The presence of ^{1}O$_2$ is confirmed in Fig. 3-13(b). In conclusion, SO$_4$•$^-$, ^{1}O$_2$ and OH• are involved in the oxidation of TC, and SO$_4$•$^-$, ^{1}O$_2$ are the main active species.

Chapter 4 Conclusion and Prospect

4.1 Conclusion

In this master's thesis, advanced oxidation technology based on $SO_4^{•-}$ is used to treat refractory pharmaceutical wastewater. Tetracycline hydrochloride wastewater is used to simulate pharmaceutical wastewater. $LaCoO_3$ doped $g\text{-}C_3N_4$ is prepared to activate PMS to degrade tetracycline hydrochloride. The study on the catalytic activation performance of the catalyst, the factors affecting the degradation effect and the reaction mechanism of activating PMS to degrade tetracycline hydrochloride not only provides research ideas for the treatment of dye wastewater, but also promotes the development of heterogeneous advanced oxidation technology based on $SO_4^{•-}$, which has potential application value.

$LaCoO_3$ doped $g\text{-}C_3N_4$ heterogeneous catalyst ($LaCoO_3/C_3N_4$) was prepared by a simple hydrothermal method. The catalysts were characterized by XRD, FT-IR, Raman and BET. The specific surface area, pore volume and pore diameter of the catalyst were analyzed by nitrogen adsorption desorption curve, which showed that the addition of C_3N_4 was beneficial to improve the specific surface area of $LaCoO_3$.
In this paper, the catalytic activity, reaction conditions and reaction mechanism of $LaCoO_3/C_3N_4$ catalyst were deeply explored:

The degradation of tetracycline hydrochloride by $LaCoO_3/C_3N_4$ activated PMS showed that the degradation rate of $LaCoO_3/C_3N_4$ was higher than that of pure $LaCoO_3$. The optimal experimental parameters for the degradation of tetracycline hydrochloride by $LaCoO_3/C_3N_4/PMS$ system are as follows: the initial concentration of PMS is 0.2 g/L, the dosage of $LaCoO_3/C_3N_4$ is 0.3 g/L, the initial concentration of tetracycline

hydrochloride is 10 mg/L, the pH of the reaction system is about 3, the reaction temperature is 25 ℃, and the removal rate of tetracycline hydrochloride is 89% within 30 minutes. The effect of $LaCoO_3/C_3N_4/PMS$ system on the degradation of tetracycline hydrochloride was confirmed by inhibition experiment and active radical detection and analysis, mainly due to the oxidative degradation of pollutants by $SO_4^{\bullet-}$ and $^1O_2$ produced in the system.

4.2 Expectation

As a new wastewater treatment technology, advanced oxidation technology based on $SO_4^{\bullet-}$ has a good treatment effect on high concentration or refractory organics. Compared with traditional Fenton oxidation technology, it has the advantages of easy operation, low treatment cost and wide pH adaptation range.

In this master's thesis, the advanced oxidation technology based on $SO_4^{\bullet-}$ is applied to the treatment of pharmaceutical wastewater, and some results have been achieved, which provides a certain theoretical basis for the practical application of this technology, but there are still some deficiencies, and there is still a lot of work to be studied:

(1) The research of this subject is still under the laboratory simulation conditions. In order to apply the degradation system to practice, a large number of experiments need to be carried out to find the optimal degradation system parameters in the process of treating actual industrial wastewater.

(2) It is necessary to evaluate the stability of the catalyst, so as to increase the practical application of the catalyst.

(3) As an important index affecting advanced oxidation technology, pH value will affect the effect of wastewater treatment and the mechanism of producing $SO_4^{\bullet-}$ degrading

organic pollutants. Therefore, it is necessary to further study the impact of pH.

Reference

[1] J.A. Melero, F. Martinez, J.A. Botas, R. Molina, M.I. Pariente, Heterogeneous catalytic wet peroxide oxidation systems for the treatment of an industrial pharmaceutical wastewater, WATER RESEARCH, 43 (2009) 4010-4018.

[2] S.W. da Silva, J.B. Welter, L.L. Albornoz, A.N. Arenhart Heberle, J.Z. Ferreira, A.M. Bernardes, Advanced Electrochemical Oxidation Processes in the Treatment of Pharmaceutical Containing Water and Wastewater: a Review, CURRENT POLLUTION REPORTS, 7 (2021) 146-159.

[3] J. Ouyang, L. Zhou, Z. Liu, J.Y.Y. Heng, W. Chen, Biomass-derived activated carbons for the removal of pharmaceutical mircopollutants from wastewater: A review, SEPARATION AND PURIFICATION TECHNOLOGY, 253 (2020).

[4] N. Rosman, W.N.W. Salleh, M.A. Mohamed, J. Jaafar, A.F. Ismail, Z. Harun, Hybrid membrane filtration-advanced oxidation processes for removal of pharmaceutical residue, JOURNAL OF COLLOID AND INTERFACE SCIENCE, 532 (2018) 236-260.

[5] K.M. Onesios, J.T. Yu, E.J. Bouwer, Biodegradation and removal of pharmaceuticals and personal care products in treatment systems: a review, BIODEGRADATION, 20 (2009) 441-466.

[6] K.H. Chu, Y.A.J. Al-Hamadani, C.M. Park, G. Lee, M. Jang, A. Jang, N. Her, A. Son, Y. Yoon, Ultrasonic treatment of endocrine disrupting compounds, pharmaceuticals, and personal care products in water: A review, CHEMICAL ENGINEERING JOURNAL, 327 (2017) 629-647.

[7] V. Karayannis, K. Moustakas, A. Vatalis, P. Sapalidis, A. Domopoulou, Advanced oxidation of industrial effluents under microwave irradiation: state of the art,

DESALINATION AND WATER TREATMENT, 91 (2017) 138-145.

[8] M.S. Lucas, J.A. Peres, G. Li Puma, Advanced Oxidation Processes for Water and Wastewater Treatment, WATER, 13 (2021).

[9] D. Kanakaraju, B.D. Glass, M. Oelgemoeller, Advanced oxidation process-mediated removal of pharmaceuticals from water: A review, JOURNAL OF ENVIRONMENTAL MANAGEMENT, 219 (2018) 189-207.

[10] L. Zhang, X. Zhao, C. Niu, N. Tang, H. Guo, X. Wen, C. Liang, G. Zeng, Enhanced activation of peroxymonosulfate by magnetic Co3MnFeO6 nanoparticles for removal of carbamazepine: Efficiency, synergetic mechanism and stability, Chemical Engineering Journal, 362 (2019) 851-864.

[11] S. Giannakis, K.-Y.A. Lin, F. Ghanbari, A review of the recent advances on the treatment of industrial wastewaters by Sulfate Radical-based Advanced Oxidation Processes (SR-AOPs), CHEMICAL ENGINEERING JOURNAL, 406 (2021).

[12] P.D. Hu, M.C. Long, Cobalt-catalyzed sulfate radical-based advanced oxidation: A review on heterogeneous catalysts and applications, Applied Catalysis B-Environmental, 181 (2016) 103-117.

[13] M. Kohantorabi, G. Moussavi, S. Giannakis, A review of the innovations in metal- and carbon-based catalysts explored for heterogeneous peroxymonosulfate (PMS) activation, with focus on radical vs . non-radical degradation pathways of organic contaminants, CHEMICAL ENGINEERING JOURNAL, 411 (2021).

[14] W. Han, L. Dong, Activation Methods of Advanced Oxidation Processes Based on Sulfate Radical and Their Applications in The Degradation of Organic Pollutants, PROGRESS IN CHEMISTRY, 33 (2021) 1426-1439.

[15] H.C. Yap, Y.L. Pang, S. Lim, A.Z. Abdullah, H.C. Ong, C.H. Wu, A comprehensive review on state-of-the-art photo-, sono-, and sonophotocatalytic treatments to degrade emerging contaminants, INTERNATIONAL JOURNAL OF ENVIRONMENTAL SCIENCE AND TECHNOLOGY, 16 (2019) 601-628.

[16] J. Sharma, I.M. Mishra, V. Kumar, Degradation and mineralization of Bisphenol A (BPA) in aqueous solution using advanced oxidation processes: UV/H_2O_2 and $UV/S_2O_8^{2-}$ oxidation systems, Journal of Environmental Management, 156 (2015) 266-275.

[17] Z.-H. Diao, Z.-Y. Lin, X.-Z. Chen, L. Yan, F.-X. Dong, W. Qian, L.-J. Kong, J.-J. Du, W. Chu, Ultrasound-assisted heterogeneous activation of peroxymonosulphate by natural pyrite for 2,4-diclorophenol degradation in water: Synergistic effects, pathway and mechanism, Chemical Engineering Journal, 389 (2020) 123771.

[18] S. Wang, N. Zhou, S. Wu, Q. Zhang, Z. Yang, Modeling the oxidation kinetics of sono-activated persulfate's process on the degradation of humic acid, Ultrasonics Sonochemistry, 23 (2015) 128-134.

[19] B. Li, L. Li, K. Lin, W. Zhang, S. Lu, Q. Luo, Removal of 1,1,1-trichloroethane from aqueous solution by a sono-activated persulfate process, Ultrasonics Sonochemistry, 20 (2013) 855-863.

[20] M. Cui, K. Cui, X. Liu, X. Chen, Y. Chen, Z. Guo, Roles of alkali metal dopants and surface defects on polymeric carbon nitride in photocatalytic peroxymonosulfate activation towards water decontamination, JOURNAL OF HAZARDOUS MATERIALS, 424 (2022).

[21] F. Yang, Y. Huang, C.L. Fang, Y. Xue, L.Y. Ai, J.S. Liu, Z.H. Wang,

Peroxymonosulfate/base process in saline wastewater treatment: The fight between alkalinity and chloride ions, Chemosphere, 199 (2018) 84-88.

[22] B.T. Zhang, W.X. Xiang, X.M. Jiang, Y. Zhang, Y.G. Teng, Oxidation of Dyes by Alkaline-Activated Peroxymonosulfate, Journal of Environmental Engineering, 142 (2016).

[23] X. Lou, C. Fang, Z. Geng, Y. Jin, D. Xiao, Z. Wang, J. Liu, Y. Guo, Significantly enhanced base activation of peroxymonosulfate by polyphosphates: Kinetics and mechanism, Chemosphere, 173 (2017) 529-534.

[24] M. Marchesi, N.R. Thomson, R. Aravena, K.S. Sra, N. Otero, A. Soler, Carbon isotope fractionation of 1,1,1-trichloroethane during base-catalyzed persulfate treatment, Journal of Hazardous Materials, 260 (2013) 61-66.

[25] B. Bouzayani, E. Rosales, M. Pazos, S.C. Elaoud, M.A. Sanromán, Homogeneous and heterogeneous peroxymonosulfate activation by transition metals for the degradation of industrial leather dye, Journal of Cleaner Production, 228 (2019) 222-230.

[26] S. Wang, J. Wu, X. Lu, W. Xu, Q. Gong, J. Ding, B. Dan, P. Xie, Removal of acetaminophen in the Fe2+/persulfate system: Kinetic model and degradation pathways, Chemical Engineering Journal, 358 (2019) 1091-1100.

[27] Y. Ji, C. Ferronato, A. Salvador, X. Yang, J.-M. Chovelon, Degradation of ciprofloxacin and sulfamethoxazole by ferrous-activated persulfate: Implications for remediation of groundwater contaminated by antibiotics, Science of The Total Environment, 472 (2014) 800-808.

[28] G.P. Anipsitakis, D.D. Dionysiou, Degradation of Organic Contaminants in Water

with Sulfate Radicals Generated by the Conjunction of Peroxymonosulfate with Cobalt, Environmental Science & Technology, 37 (2003) 4790-4797.

[29] R. Matta, S. Tlili, S. Chiron, S. Barbati, Removal of carbamazepine from urban wastewater by sulfate radical oxidation, ENVIRONMENTAL CHEMISTRY LETTERS, 9 (2011) 347-353.

[30] K.H. Chan, W. Chu, Degradation of atrazine by cobalt-mediated activation of peroxymonosulfate: Different cobalt counteranions in homogenous process and cobalt oxide catalysts in photolytic heterogeneous process, Water Research, 43 (2009) 2513-2521.

[31] E.R. Bandala, L. Brito, M. Pelaez, Degradation of domoic acid toxin by UV-promoted Fenton-like processes in seawater, Desalination, 245 (2009) 135-145.

[32] Y.-F. Huang, Y.-H. Huang, Behavioral evidence of the dominant radicals and intermediates involved in Bisphenol A degradation using an efficient Co2+/PMS oxidation process, Journal of Hazardous Materials, 167 (2009) 418-426.

[33] E.R. Bandala, M.A. Peláez, D.D. Dionysiou, S. Gelover, J. Garcia, D. Macías, Degradation of 2,4-dichlorophenoxyacetic acid (2,4-D) using cobalt-peroxymonosulfate in Fenton-like process, Journal of Photochemistry and Photobiology A: Chemistry, 186 (2007) 357-363.

[34] Z. Yang, Y. Li, X. Zhang, X. Cui, S. He, H. Liang, A. Ding, Sludge activated carbon-based CoFe2O4-SAC nanocomposites used as heterogeneous catalysts for degrading antibiotic norfloxacin through activating peroxymonosulfate, Chemical Engineering Journal, 384 (2020) 123319.

[35] P. Shukla, S. Wang, K. Singh, H.M. Ang, M.O. Tadé, Cobalt exchanged zeolites for

heterogeneous catalytic oxidation of phenol in the presence of peroxymonosulphate, Applied Catalysis B: Environmental, 99 (2010) 163-169.

[36] Y. Yao, C. Xu, J. Qin, F. Wei, M. Rao, S. Wang, Synthesis of Magnetic Cobalt Nanoparticles Anchored on Graphene Nanosheets and Catalytic Decomposition of Orange II, Industrial & Engineering Chemistry Research, 52 (2013) 17341-17350.

[37] P. Shukla, Combined adsorption and oxidation technique for waste water treatment: potential application in permeable reactive barrier, Curtin University, 2010.

[38] A. Safikhani, V. Vatanpour, S. Habibzadeh, M.R. Saeb, Application of graphitic carbon nitrides in developing polymeric membranes: A review, Chemical Engineering Research & Design, 173 (2021) 234-252.

[39] Y.-P. Sun, W. Ha, J. Chen, H.-Y. Qi, Y.-P. Shi, Advances and applications of graphitic carbon nitride as sorbent in analytical chemistry for sample pretreatment: A review, Trac-Trends in Analytical Chemistry, 84 (2016) 12-21.

[40] H.B. Truong, S. Bae, J. Cho, J. Hur, Advances in application of g-C3N4-based materials for treatment of polluted water and wastewater via activation of oxidants and photoelectrocatalysis: A comprehensive review, Chemosphere, 286 (2022).

[41] H. Ehtesabi, Carbon nanomaterials for salivary-based biosensors: a review, Materials Today Chemistry, 17 (2020).

[42] W. Wang, C. Zhou, Y. Yang, G. Zeng, C. Zhang, Y. Zhou, J. Yang, D. Huang, H. Wang, W. Xiong, X. Li, Y. Fu, Z. Wang, Q. He, M. Jia, H. Luo, Carbon nitride based photocatalysts for solar photocatalytic disinfection, can we go further?, Chemical Engineering Journal, 404 (2021).

[43] L. Cheng, H. Zhang, X. Li, J. Fan, Q. Xiang, Carbon-Graphitic Carbon Nitride

Hybrids for Heterogeneous Photocatalysis, Small, 17 (2021).

[44] Y.L. Pang, Z.X. Law, S. Lim, Y.Y. Chan, S.H. Shuit, W.C. Chong, C.W. Lai, Enhanced photocatalytic degradation of methyl orange by coconut shell-derived biochar composites under visible LED light irradiation, Environmental Science and Pollution Research.

[45] Z. Zhao, Y. Sun, F. Dong, Graphitic carbon nitride based nanocomposites: a review, Nanoscale, 7 (2015) 15-37.

[46] C. Jia, L. Yang, Y. Zhang, X. Zhang, K. Xiao, J. Xu, J. Liu, Graphitic Carbon Nitride Films: Emerging Paradigm for Versatile Applications, Acs Applied Materials & Interfaces, 12 (2020) 53571-53591.

[47] K. Qi, S.-y. Liu, A. Zada, Graphitic carbon nitride, a polymer photocatalyst, Journal of the Taiwan Institute of Chemical Engineers, 109 (2020) 111-123.

[48] X. Kong, X. Liu, Y. Zheng, P.K. Chu, Y. Zhang, S. Wu, Graphitic carbon nitride-based materials for photocatalytic antibacterial application, Materials Science & Engineering R-Reports, 145 (2021).

[49] D. Chen, J. Yang, H. Ding, Synthesis of nanoporous carbon nitride using calcium carbonate as templates with enhanced visible-light photocatalytic activity, Applied Surface Science, 391 (2017) 384-391.

[50] M. Tahir, C. Cao, N. Mahmood, F.K. Butt, A. Mahmood, F. Idrees, S. Hussain, M. Tanveer, Z. Ali, I. Aslam, Multifunctional g-C3N4 nanofibers: a template-free fabrication and enhanced optical, electrochemical, and photocatalyst properties, ACS applied materials & interfaces, 6 (2014) 1258-1265.

[51] S. Zhao, Y. Zhang, Y. Zhou, Y. Wang, K. Qiu, C. Zhang, J. Fang, X. Sheng, Facile

one-step synthesis of hollow mesoporous g-C3N4 spheres with ultrathin nanosheets for photoredox water splitting, Carbon, 126 (2018) 247-256.

[52] M. Zhang, J. Xu, R. Zong, Y. Zhu, Enhancement of visible light photocatalytic activities via porous structure of g-C3N4, Applied Catalysis B: Environmental, 147 (2014) 229-235.

[53] Y. Xu, F. Ge, Z. Chen, S. Huang, W. Wei, M. Xie, H. Xu, H. Li, One-step synthesis of Fe-doped surface-alkalinized g-C3N4 and their improved visible-light photocatalytic performance, Applied Surface Science, 469 (2019) 739-746.

[54] Y. Zhang, J. Yuan, L. Zhao, B. Wu, B. Zhang, P. Zhang, S. Zhang, C. Dong, Boosting exciton dissociation and charge transfer in P-doped 2D porous g-C3N4 for enhanced H2 production and molecular oxygen activation, Ceramics International, (2021).

[55] J. Huang, D. Li, R. Li, P. Chen, Q. Zhang, H. Liu, W. Lv, G. Liu, Y. Feng, One-step synthesis of phosphorus/oxygen co-doped g-C3N4/anatase TiO2 Z-scheme photocatalyst for significantly enhanced visible-light photocatalysis degradation of enrofloxacin, Journal of Hazardous Materials, 386 (2020) 121634.

[56] N. Bao, X. Hu, Q. Zhang, X. Miao, X. Jie, S. Zhou, Synthesis of porous carbon-doped g-C3N4 nanosheets with enhanced visible-light photocatalytic activity, Applied Surface Science, 403 (2017) 682-690.

[57] Z. Li, D. Huang, C. Zhou, W. Xue, L. Lei, R. Deng, Y. Yang, S. Chen, W. Wang, Z. Wang, Metal-free carbon nitride with boosting photo-redox ability realized by the controlled carbon dopants, Chemical Engineering Journal, 382 (2020) 122657.

[58] H. Chen, Y. Xu, K. Zhu, H. Zhang, Understanding oxygen-deficient

La2CuO4-delta perovskite activated peroxymonosulfate for bisphenol A degradation: The role of localized electron within oxygen vacancy, APPLIED CATALYSIS B-ENVIRONMENTAL, 284 (2021).

[59] F.J. Beltran, P. Pocostales, P. Alvarez, J.F. Garcia-Araya, O. Gimeno, Perovskite Catalytic Ozonation of Some Pharmaceutical Compounds in Water, OZONE-SCIENCE & ENGINEERING, 32 (2010) 230-237.

[60] Y. Chen, W. Huang, D. He, S. Yue, H. Hong, Construction of Heterostructured g-C3N4/Ag/TiO2 Microspheres with Enhanced Photocatalysis Performance under Visible-Light Irradiation, Acs Applied Materials & Interfaces, 6 (2014).

[61] Z. Cui, Y. Hua, X. Zhao, Enhanced photocatalytic performance of g-C 3 N 4 /Bi 4 Ti 3 O 12 heterojunction nanocomposites, Materials Science and Engineering: B, 229 (2018) 160-172.

[62] D. Ding, S. Yang, L. Chen, T. Cai, Degradation of norfloxacin by CoFe alloy nanoparticles encapsulated in nitrogen doped graphitic carbon (CoFe@N-GC) activated peroxymonosulfate, Chemical Engineering Journal, 392 (2020).

[63] R. Du D Ric, A. Vladescu, V. Rednic, M. Neumann, I.G. Deac, R. Tetean, XPS study on La0.67Ca0.33Mn1xCoxO3 compounds, Journal of Molecular Structure, 1073 (2014) 66-70.

[64] W.D. Oh, Z. Dong, T.T.J.A.C.B.E. Lim, Generation of sulfate radical through heterogeneous catalysis for organic contaminants removal: Current development, challenges and prospects, (2016) 169-201.

Water Science & Technology

Application of CoMn/CoFe layered double hydroxide based on metal–organic frameworks template to activate peroxymonosulfate for 2,4-dichlorophenol degradation

Chenyu Liu[a], Haitong Wei[a], Yanhui Gao [a], Ning Wang[a], Xiaoying Yuan[a], Zhilong Chi[b,c], Guangli Zhao[b,c], Shuguang Song[d], Jianjun Song [a,*] and Xinghui Jin[a]

[a] Shandong Provincial Key Laboratory of Molecular Engineering, School of Chemistry and Chemical Engineering, Qilu University of Technology (Shandong Academy of Sciences), Jinan 250353, China
[b] Kyiv College at Qilu University of Technology, Qilu University of Technology (Shandong Academy of Sciences), Jinan 250353, China
[c] Kyiv National University of Technologies and Design, Kyiv 01011, Ukraine
[d] School of Transportation Engineering, Shandong Jianzhu University, Jinan 250101, China
*Corresponding author. E-mail: qlusong@163.com

YG, 0000-0002-6562-6149; ZC, 0000-0002-0134-4230; JS, 0000-0002-5496-9111

ABSTRACT

Metal–organic frameworks (MOFs) have unique properties and stable structures, which have been widely used as templates/precursors to prepare well developed pore structure and high specific surface area materials. In this article, an innovative and facile method of crystal reorganization was designed by using MOFs as sacrificial templates to prepare a layered double hydroxide (LDH) nano-layer sheet structure through a pseudomorphic conversion process under alkaline conditions. The obtained CoMn-LDH and CoFe-LDH catalysts broke the ligand of MOFs and reorganized the structure on the basis of retaining a high specific surface area and a large number of pores, which had higher specific surface area and well developed pore structure compared with LDH catalysts prepared by traditional methods, and thus provide more active sites to activate peroxymonosulfate (PMS). Due to the unique framework structure of MOFs, the MOF-derived CoMn-LDH and CoFe-LDH catalysts could provide more active sites to activate PMS, and achieve a 2,4-dichlorophenol degradation of 99.3% and 99.2% within 20 minutes, respectively. In addition the two LDH catalysts displayed excellent degradation performance for bisphenol A, ciprofloxacin and 2,4-dichlorophenoxyacetic acid (2,4-D). X-ray photoelectron spectroscopy indicated that the valence state transformation of metal elements participated in PMS activation. Electron paramagnetic resonance manifested that sulfate radical (SO_4^{-}) and singlet oxygen ($^1O_2$) were the main species for degrading pollutants. In addition, after the three-cycle experiment, the CoMn-LDH and CoFe-LDH catalysts also showed long-term stability with a slight activity decrease in the third cycle. The phytotoxicity assessment determined by the germination of mung beans proved that PMS activation by MOF-derived LDH catalysts can basically eliminate the phytotoxicity of a 2,4-D solution. This research not only developed high-activity LDH catalysts for PMS activation, but also expanded the environmental applications of MOF derivants.

Key words: catalysis, degradation, layered double hydroxide (LDH), MOF derived, peroxymonosulfate

HIGHLIGHTS

- LDH derived from MOFs through a pseudomorphic conversion process.
- LDH showed excellent activity to activate PMS to degrade 2,4-DCP and other pollutants.
- CoMn-LDH and CoFe-LDH exhibited high stability and reusability.
- High specific surface area and well developed pore structure of LDH provide more active sites.
- Phytotoxicity assessment displayed the practical application value of LDH.

GRAPHICAL ABSTRACT
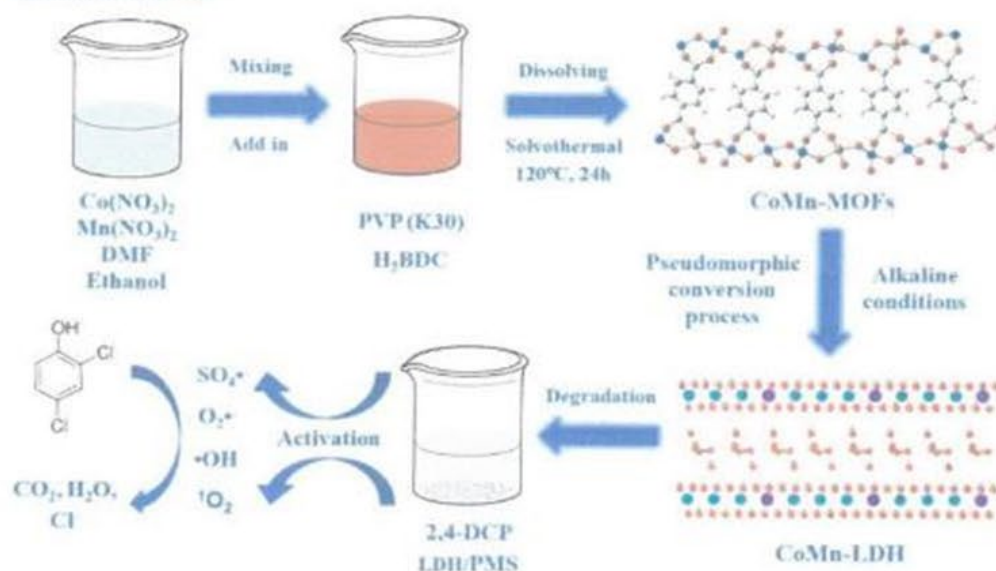
1. INTRODUCTION

Chlorophenol organics are widely used in oil refining, coking, papermaking, plastics, printing and dyeing industries (Yu et al. 2018; Xie et al. 2020). Because of their carcinogenic, teratogenic, mutagenic potential toxicity and refractory properties, they are listed as priority pollutants. 2,4-Dichlorophenol (2,4-DCP), as a typical chlorophenol pollutant, widely exists in industrial wastewater (Yuan et al. 2017; Tian et al. 2019) and shows significant impact on the water environment and human health. Therefore, it is urgent to solve the problem of water pollution caused by chlorophenols. At present, various methods have been used to remove 2,4-DCP and multiple organic pollutants, including membrane separation (Yin et al. 2021), electrochemistry (Ma et al. 2021), adsorption (Liu et al. 2009), and photodegradation (Hou et al. 2021a, 2021b). However, these methods often have shortcomings such as low efficiency, secondary pollution, or complicated operation (Olmez-Hanci et al. 2013). Therefore, it is urgent to seek the more efficient ways to eliminate the hazards of 2,4-DCP.

In recent years, the advanced oxidation techniques (SR-AOPs) based on sulfate radicals ($SO_4^{\bullet-}$) has attracted extensive research due to their higher standard reduction potential (2.5–3.1 V) compared with hydroxyl radicals ($^{\bullet}HO$) (1.8–2.7 V), which have been widely used for degradation of various organic substances. $SO_4^{\bullet-}$ can be produced by activation of peroxymonosulfate (PMS) and peroxydisulfate (PS) through ultraviolet light (Wang et al. 2017), heat (Pan et al. 2018), electrocatalysis (Ahsan et al. 2021), transition metal catalysts (Wang & Wang 2018) and other ways (Ahsan et al. 2020b, 2020c). Among different methods, the transition metal catalysts, such as Ag(I), Co(II), Fe(II/III), Ce(IV), Mn(IV), etc., which were widely used activate PMS for degradation of organic compounds, and theoretically most refractory organics could be degraded through PMS activation (Yang et al. 2009; Ji et al. 2014; Huang et al. 2017). Among transition metals, Co(II)/PMS homogeneous system has received extensive attention from researchers due to the advantages of high activity and low cost (Hu & Long 2016; Xiao et al. 2018). In previous studies, it was found that homogeneous transition metal catalysts are difficult to recycle and thus cause secondary pollution. Compared with homogeneous Co(II) catalysts, heterogeneous catalysts have the advantages of easy separation and recycling, which shows more potential for PMS activation. Therefore, to design a stable, low-loss heterogeneous transition metal catalyst with high catalytic performance is the key to improve catalyst performance and promote industrialization of PMS activation.

Transition metal catalysts are generally used for PMS activation and other catalytic reaction in the form of oxides (Wang et al. 2022), sulfides (Li et al. 2021), hydroxides (Yang et al. 2021a), supported catalysts (Ahsan et al. 2020a), perovskite (Geng et al. 2020), and so on. As a typical anion layer material, layered double hydroxides (LDHs) are often referred to as hydrotalcite-like compounds, consisting of a body laminate with metal hydroxide and an interlayer region containing compensating anions and solvated molecules (Daud et al. 2016). At present, transition metal-based LDHs are widely used for PMS activation because of their unique structure and relatively simple synthesis method (Chen et al. 2019; Cao et al. 2020a). Generally, LDH was mainly prepared by hydrothermal methods (Huang et al. 2021), precipitation methods (Xiao et al. 2019) and other traditional methods, but the specific surface area, morphology and structure of the LDH samples obtained by these methods are difficult to accurately control. Seeking a facile method to prepare LDH with controlled specific surface area and specific structure is the key to study the structure–activity relationship between the catalyst structure and catalytic performance, thus further improving the activity of the LDH catalyst.

Metal–organic frameworks (MOFs) are crystalline porous materials with periodic network structure formed by self-assembly of metal ions and organic bridging ligands (Yaghi et al. 1995; Liu et al. 2017). MOFs have the advantages of large specific surface area, metal center variability, organic ligand diversity, large pore volume, high stability, and these special properties make MOFs an ideal sacrificial template or precursor for preparation of nanomaterials with specific structure, such as porous carbon (Zhang et al. 2014; Lai et al. 2016), metal oxides (Yu et al. 2016; Yuan et al. 2017) and metal sulfides (Li et al. 2016; Jin et al. 2017). Furthermore, MOFs can also be used as sacrificial precursors to synthesize LDH samples with good pore structure and high specific surface area. Existing research showed that MOF-derived LDH has been widely used as a catalyst (Yang et al. 2021b; Yusuf et al. 2021), supercapacitors (Xiao et al. 2019; Liu et al. 2022), sensors (Qin et al. 2021; Shen et al. 2021) and so on. Xiao and colleagues (Xiao et al. 2019) prepared LDH samples by replacement of the organic ligands in MOFs with OH$^-$ under alkaline conditions, which obtained a larger surface area and high porosity and exhibited excellent electrochemical performance. Based on the above research, MOFs can be used as precursors to prepare high-performance LDH catalysts by etching under alkaline conditions, applicable in the field of PMS activation for pollutants elimination.

In this article, CoMn-LDH and CoFe-LDH catalysts with high specific surface area and well developed pore structure were prepared though a pseudomorphic conversion process by using CoMn-MOF and CoFe-MOF as precursors through replacing the organic ligands by OH$^-$. The MOF-derived LDH catalysts were used to activate PMS for degradation of 2,4-DCP and other pollutants. Different factors (temperature, pressure, PMS and catalyst dosage) affecting PMS activation were systematically studied. In addition, the stability and reusability of two LDH samples were tested. Radical scavenger test, electron paramagnetic resonance (EPR) experiments and X-ray photoelectron spectroscopy (XPS) characterization were also performed to elucidate the types of reaction species and PMS activation mechanism. Moreover, total organic carbon (TOC) test and phytotoxicity assessment were conducted in order to determine the mineralization of the organic pollutant and the toxicity of the degraded organic pollutant. This study provides a promising insight for the precise design of PMS activation catalysts with specific structures, and further broadens the application of MOF derivatives.

2. MATERIALS AND METHODS

2.1. Chemical reagents

All chemical reagents were used without further purification. Ferric nitrate nonahydrate (Fe(NO$_3$)$_3$·9H$_2$O, ≥99.99%), cobalt nitrate hexahydrate (Co(NO$_3$)$_2$·6H$_2$O, ≥99.99%), manganese nitrate solution (Mn(NO$_3$)$_2$, 50 wt% solution), polyvinylpyrrolidone (PVP, K29-32), potassium peroxomonosulfate (PMS, ≥42.8%), l-histidine (≥99%), p-benzoquinone (≥99%), 2,4-DCP, ≥98%), 2,4-dichlorophenoxyacetic acid (2,4-D, ≥98%), ciprofloxacin (CIP, ≥98%), bisphenol A (BPA, ≥99%), hydrogen peroxide solution (H$_2$O$_2$, 3 wt% in water), 5,5-dimethylpyrroline-oxide (DMPO, ≥97%), 4-amino-2,2,6,6-tetramethylpiperidine (TEMP, ≥98%) and 1,4-benzenedicarboxylic acid (H$_2$BDC, ≥99%) were purchased from Aladdin Industrial Corporation. Sodium hydroxide (NaOH, ≥98%), N,N dimethylformamide (DMF, ≥99.5%), tert-butyl alcohol (TBA, ≥99%), ethanol (≥99.7%), formic acid (1% w/v), acetic acid (99.8%), high-performance liquid chromatography (HPLC) grade acetonitrile (≥99.9%) and HPLC grade methanol (≥99.9%) were purchased from Sinopharm Chemical Regent Co. Ltd. Mung beans were purchased from a local store.

2.2. Synthesis of MOF-derived LDH catalysts

CoMn-MOF was prepared by the solvothermal method: 2 mmol Mn(NO$_3$)$_2$·6H$_2$O, 4 mmol Co(NO$_3$)$_2$·6H$_2$O, 1.2 g PVP (K29-32) and 0.6645 g H$_2$BDC were added in the solution containing 30 mL DMF and 20 mL ethanol, and then stirred for 1 hour at

room temperature. After that, the mixture was sealed in a 100 mL Teflon-lined stainless steel autoclave and kept at 120 °C for 24 h. After cooling to room temperature, the product was centrifuged, then repeatedly washed with ethanol and then dried at 70 °C overnight. The obtained CoMn-MOF precipitate was immersed in 50 mL 2 M NaOH aqueous solution and stirred at room temperature for 3 h to prepare CoMn-LDH. After that, the product was washed with deionized water to remove excess NaOH. Finally, the MOF-derived LDH sample was obtained after drying at 70 °C overnight.

The CoFe-LDH catalyst was prepared using the same methods but by using 2 mmol $Fe(NO_3)_3·9H_2O$ instead of $Mn(NO_3)_2·6H_2O$.

2.3. Characterization

The X-ray diffraction (XRD) pattern of the sample was measured on a Bruker D8 advanced X-ray powder diffractometer with Cu $K\alpha$ radiation ($\lambda = 1.5418$ Å). The morphology and structure of LDHs were observed by using an Hitachi S-4800 field emission scanning electron microscope (SEM). The transmission electron microscopy (TEM) was tested by using a JEOL JEM-2100 instrument to further observe the nanostructures. The specific surface area was measured by using Micromeritics ASAP 2020 equipment to perform nitrogen adsorption–desorption measurements at 77 K (Micromeritics, USA) and the sample was determined according to Brunauer–Emmett–Teller (BET) (Benselka-Hadj Abdelkader et al.) analysis. Through Thermo Fisher ESCALABXi+ XPS and Al-K (1,486.6 eV) as the X-ray source, the surface composition and electronic state of Co, Fe, Mg, O and other elements were recorded then analyzed. The FT-IR spectrum was measured at 4,000–400 cm^{-1} using a PerkinElmer Frontier FT-IR spectrometer. EPR (Bruker EMX/plus) was used to detect reaction species generated by the reaction through DMPO and TEMP as spin-trapping agents. The concentrations of cobalt, manganese and iron were determined by the solution and used inductively coupled plasma mass spectroscopy (ICP-MS) (Scientific iCAP RQ). Thermogravimetric analysis (TGA) and differential scanning calorimetry (DSC) were tested on a Mettler Toledo TGA-1 thermal analyzer in a dynamic N_2 atmosphere and the heating rate was 10 °C/minute.

2.4. Catalytic degradation experiments

In a typical degradation experiment unless otherwise specified, 10 mg of catalyst (0.2 g/L) was dispersed into 50 mL of 2,4-DCP solution (20 mg/L), and then stirred for 30 minutes to eliminate the effect of adsorption. After reaching adsorption–desorption equilibrium, a 1.0 mL of PMS solution (10 mg/mL) was added into above solution to start the PMS activation reaction. After that, a 1.0 mL sample was taken into a centrifuge tube every 5 minutes, and immediately mixed with 1.0 mL methanol to stop the catalytic reaction. Then, the collected sample was filtered through a 0.22-μm filter membrane into an HPLC vial. Unless otherwise stated, the catalytic performance of all catalysts was evaluated in a beaker at room temperature (25 ± 1 °C), and all tests were conducted in deionized water with an initial pH (pH_0) of 6.5. The effects of different influence factors (catalyst dosage, PMS dosage, temperature) on the PMS activation and the stability and reusability of the catalysts were also tested. In order to study the reusability of the catalyst, the catalyst was collected by centrifugation, washed several times with ethanol and deionized water and dried for the next cycle. The concentrations of 2,4-DCP and other pollutants were measured by HPLC (LC-20A) on an instrument equipped with a Phenomenex C18 column under a UV detector and the specific test conditions for these are shown in Table 1. TOC was measured by using a TOC analyzer (TOC-L, CPH, Shimadzu).

Table 1 | The analytical conditions of multiple organic pollutants

Organic pollutants	Mobile phase (v/v)	Flow rate (mL/min)	Detection wavelength (nm)	References
2,4-Dichlorophenol (2,4-DCP)	Methanol/Water = 70/30	1	285	Wang et al. (2021)
2,4-Dichlorophenoxyacetic acid (2,4-D)	Acetonitrile/0.2% Formic acid = 40/60	1	284	Li et al. (2020a)
Ibuprofen (IBP)	Methanol/0.1% Acetic acid = 60/40	1	210	Nawaz et al. (2020)
Ciprofloxacin (CIP)	Acetonitrile/0.1% Formic acid = 20/80	1	278	Mukherjee et al. (2021)

2.5. Phytotoxicity assessment

The toxicity test was based on the germination rate and radicle length of mung beans (Peng et al. 2020). At the first, mung bean seeds were sterilized with 3% H_2O_2, and rinsed with ultrapure water several times. Then 100 cleaned mung beans were taken and placed on the filter paper as a carrier. The seeds were cultured by using the undegraded 2,4-D solution (20 mg/L), the 2,4-DCP solution degraded by CoMn-LDH, the 2,4-DCP solution degraded by CoFe-LDH and ultrapure water. An appropriate amount of the solution was replenished into a Petri dish twice a day during the culture process. Mung beans were incubated in the dark (25 ± 1 °C, 24 h) for 7 days. The germination rate of mung bean seeds was recorded every 24 hours, and 20 seedlings were randomly selected from each Petri dish after 7 days to count the radicle length.

2.6. Statistical analysis

All the measured experimental results were expressed as the mean ± SD (standard deviation) of repeated experiments. The physicochemical parameters adopted one-way ANOVA. Tukey's *post-hoc* and SPSS (version 19.0) were used to compare significant differences. When the hypothesis did not satisfy homogeneity of variance and normality, the Kruskal–Wallis test was used for data analysis, and then the Dunn multiple comparison test was adopted. The R language was used to perform Levene's test to confirm the homogeneity of variance, and Kolmogorov–Smirnov test was adopted to confirm normality (p-value > 0.05). If the p-value was <0.05, the experimental data were considered to be statistically significant.

3. RESULTS AND DISCUSSION

3.1. Characterization of MOF-derived LDH catalysts

The samples obtained were initially characterized and analyzed by SEM, TEM XRD and TG. The CoMn-LDH and CoFe-LDH samples were obtained by in-situ etching under alkaline conditions, and the hydroxyl groups were used to replace the organic ligands in MOFs. During the etching process for the ligands, crystal structures with special shapes were formed, which also created complex and hierarchical structures. As shown in Figure 1(a) and 1(b), the surface of CoMn-LDH became rough and porous, which inferred that a large number of pores were produced in the process of replacing organic ligands with hydroxyl groups. The high magnification SEM image of CoMn-LDH (Figure 1(c)) further showed that there were large numbers of porous structures on the surface and arranged at layered forms. Compared to the CoMn-LDH sample, the CoFe-LDH exhibited different morphological features. The low magnification SEM images (Figure 1(d) and 1(e)) manifested the formation of the porous stacked sheet structures. The high magnification image in Figure 1(e) further revealed that there were irregular flake nanostructures with a width of about 500 nm on the surface. For comparison, the SEM images of used CoMn-LDH and CoFe-LDH were also taken. As shown in Supplementary Material, Figure S1, the two used LDH catalysts still maintained stable layered morphology, indicating the high structural stability of two LDH catalysts. TEM (Supplementary Material, Figure S2) pictures also showed that the two fresh LDH catalysts were stacked in layered forms, which conforms to the traditional structure of LDHs. Combining SEM images with TEM images, it could be manifested that the LDH structure with layered structure has been successfully prepared.

In the XRD spectrum of CoMn-LDH (Figure 2(a)), it can be seen that the peak of the crystal appeared obvious and the characteristic peaks can be matched with $Co(OH)_2$ (JCPDS: 51-1731) and $Mn(OH)_2$ (JCPDS: 18-0787). Similarly, the XRD spectra of CoFe-LDH (Figure 2(b)) peaks were obvious and the characteristic peaks of $Co(OH)_2$ (JCPDS: 74-1057) and $Fe(OH)_2$ (JCPDS: 13-0089) could be better matched. Combined with the analysis of SEM and XRD patterns, it can be concluded that the organic ligands in MOFs were replaced by hydroxyl groups and the layered amorphous hydrotalcite-like structures were successfully synthesized, in which the reconstruction and deconstruction of the structure occurred simultaneously (Zhang et al. 2018).

As shown in the FT-IR spectra (Figure 3(a)), CoMn-LDH had a broad adsorption peak from 2,500 to 3,600 cm^{-1}, which was related to the absorption of the -OH group (Shakeel et al. 2019). The characteristic peak of CoMn-LDH appeared at about 1,650 cm^{-1} and was associated with -COO- (He et al. 2016). The bands between 900 and 1,500 cm^{-1} should be a strong absorption band of terephthalic acid ligands, but there was almost no absorption in the spectrum, which meant the organic ligands had been basically removed. Thereby, the band at 1,650 cm^{-1} can be attributed to the CO_3^{2-} ions existing in the LDH interlayer. For CoFe-LDH, there was a strong absorption peak at 3,631 cm^{-1}, which could be associated to the stretching vibration of -OH. The absorption of 3,396 cm^{-1} was also due to the absorption of the -OH group. The existence of the absorption peak from 1,350 to 1,650 cm^{-1} indicated that the terephthalic acid ligand had been basically removed and the existence of the -COO- group. This also confirmed the presence of CO_3^{2-} ions. For CoMn-LDH and CoFe-LDH, the strong absorption

100
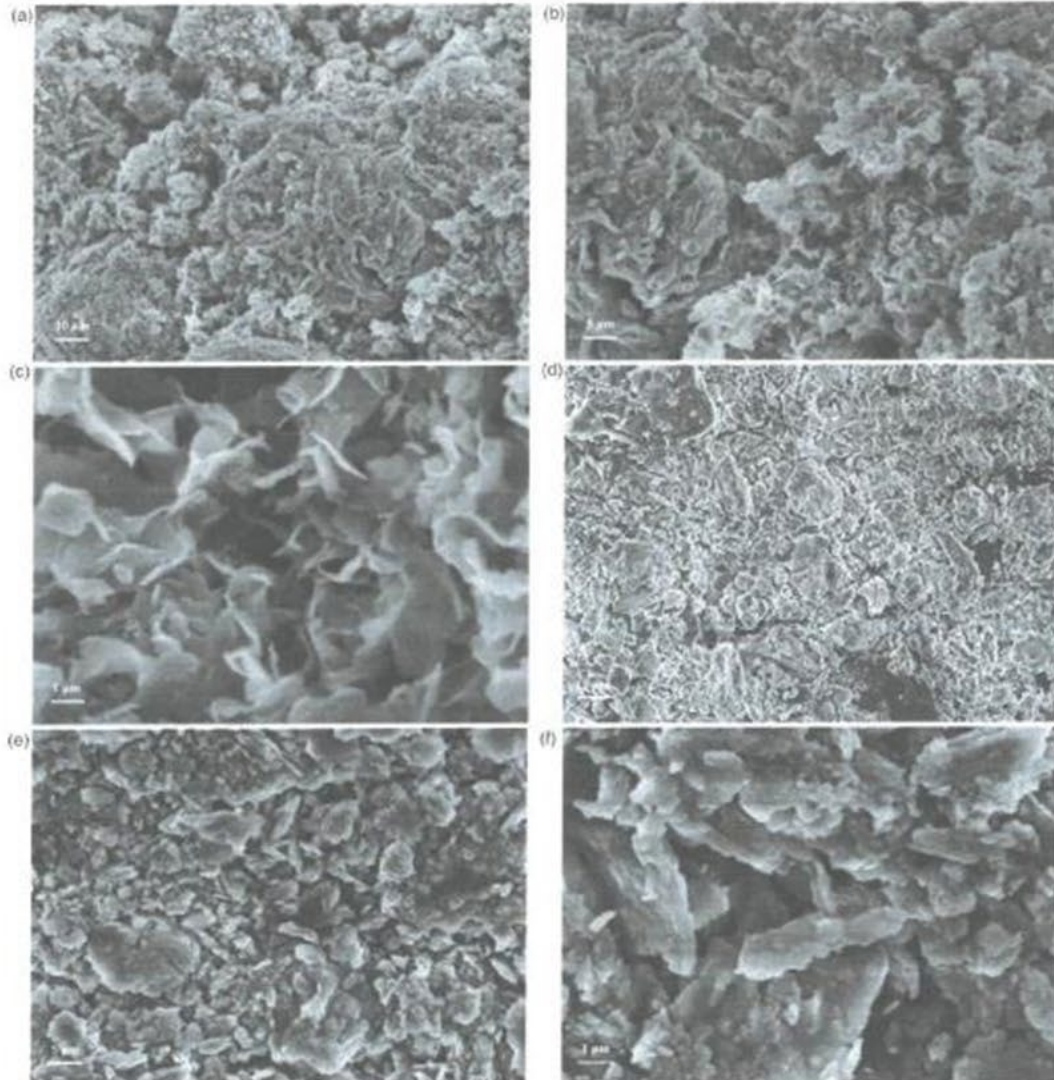
Figure 1 | SEM images of CoMn-LDH (a, b, c) and CoFe-LDH (d, e, f).

around 600 cm^{-1} could be attributed to the M-O and O-M-O stretching vibrations in LDHs (M = Co & Mn & Fe). The FT-IR results proved that the hydrotalcite structure had been synthesized and there were inorganic anions that could be exchanged between layers and externally.

The specific surface area and pore structure of CoMn-LDH and CoFe-LDH samples were evaluated by N_2 adsorption-desorption isotherm and the results are shown in Figure 3(b). The specific surface area, average pore diameter and pore volume of CoMn-LDH were 43.1 m^2/g, 33.9 nm and 0.37 cm^2/g, respectively. Almost all pores existed in the form of meso-pores. In comparison, CoFe-LDH had a higher specific surface area of 169.9 m^2/g, a smaller average pore size of 2.9 nm,

Figure 2 | XRD patterns of CoMn-LDH (a) and CoFe-LDH (b).

and a pore volume of 0.25 cm²/g. In particular, the BET specific surface area of CoFe-LDH with MOFs as the precursor is much higher than that with other traditional synthesis methods (Table 2). The increased surface area of CoFe-LDH made PMS and organic pollutant molecules easier to diffuse and interact with the reaction sites, thereby increasing the reaction rate.

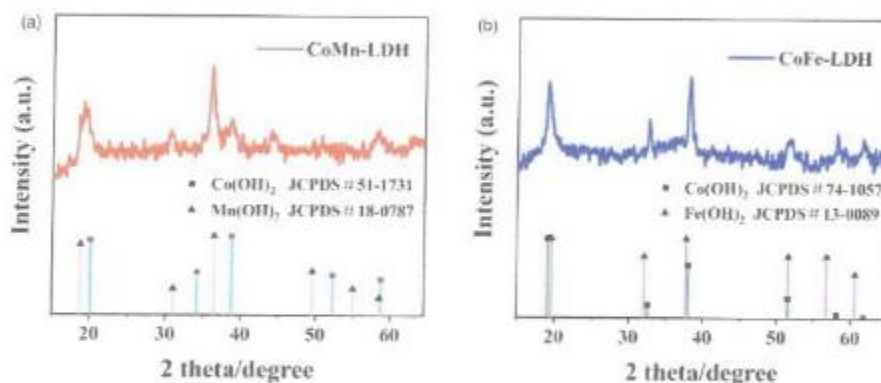TGA is an effective way to assess thermostability of materials, which is shown in Supplementary Material, Figure S3. Due to the dihydroxylation of the hydroxide in LDHs (Benselka-Hadj Abdelkader et al. 2011), the total weight loss of CoMn-LDH and CoFe-LDH were 15.1% and 21.2% respectively, and reached stable states at 460 and 710 °C. After that, the further increase in temperature did not cause continued quality loss.

The surface element composition and metal valence of CoMn-LDH and CoFe-LDH were obtained by XPS. As shown in Figure 3(c), the peaks of CoMn-LDH were mainly attributed to the C 1s, N 1s, O 1s, Mn 2p and Co 2p regions. The spectrum of Co 2p shown in Figure 3(d) was made up of two main peaks, Co $2p_{3/2}$ (779.4 eV) and Co $2p_{1/2}$ (794.3 eV). The main peak with a binding energy of 779.4 eV can be decomposed into two peaks, Co^{3+} at the peak of 779.2 eV and Co^{2+} at the peak of 780.2 eV. As shown in Figure 3(e), the Mn 2p spectrum was composed of Mn $2p_{3/2}$ (641.6 eV) and Mn $2p_{1/2}$ (653.2 eV), and the two main peaks can be divided into four peaks in total. The peaks at 642.8 eV and 653.9 eV were attributed to the Mn^{4+} species, and the peaks at 641.0 eV and 652.5 eV can be attributed to the Mn^{2+}/Mn^{3+} species. According to the peak area of different species, it can be found that Co^{3+}/Co^{2+} was 1.1, indicating that both Co^{3+} and Co^{2+} existed and the composition was basically the same. Furthermore, the proportion of Mn^{2+}/Mn^{3+} to Mn^{4+} was 2.1, indicating that Mn species was mainly in the form of Mn^{2+}/Mn^{3+}. The atomic ratio of Mn to Co was 1:2.6. The XPS results conformed to the basic characteristics of LDH and the distribution of element valence states, and matched well with the XRD result. Figure 3(f) shows the valence and composition of the elements in CoFe-LDH. It can be seen that the peaks were mainly composed of C 1s, N 1s, O 1s, Fe 2p and Co 2p. As shown in Figure 3(g), Co 2p mainly consisted of two main peaks and two larger satellite peaks. The main peak of Co $2p_{3/2}$ at 780.2 eV can be divided into 779.8 eV and 781.2 eV. At the same time, the positions of the two satellite peak bands appeared at 785.4 eV and 802.3 eV. These values matched well with the reported $Co(OH)_2$ data, which meant that the Co species in the compound presented a high-spin Co^{2+} state (Ma et al. 2011), which further confirmed the existence of $Co(OH)_2$. The XPS spectrum of Fe 2p is shown in Figure 3(h), where the Fe 2p orbital peaks were asymmetrical and there were splits and overlaps, therefore it was difficult to determine the specific composition of Fe (Biesinger et al. 2011). Generally, the appearance of satellite peaks beside the main peak meant the presence of Fe^{3+} in the compound. Peak splitting could prove that Fe^{2+} existed in the compound at the same time, which was consistent with formed $Fe(OH)_2$ detect by XRD results. The atomic ratio of Fe to Co is 1:3.4. These results showed that Co^{2+}, Fe^{2+} and Fe^{3+} are simultaneously present in the prepared CoFe-LDH, which also conformed the existence of hydrotalcite-like structures. The XPS graphs of used CoMn-LDH and CoFe-LDH are shown in Figure S4. after activating PMS to degrade organic pollutants, the valence state of LDHs has changed significantly, which showed that the transition of element valence states in the reaction process was inseparable from the PMS activation process.
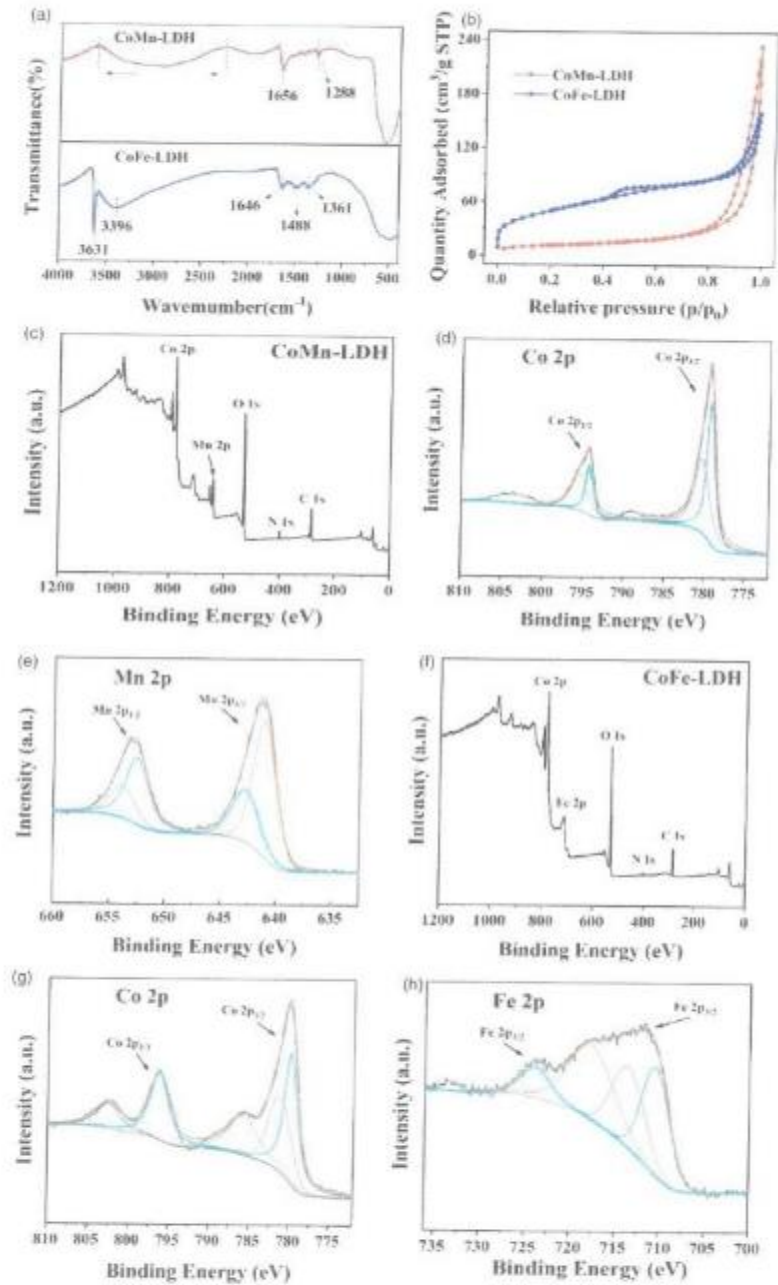
Figure 3 | FT-IR spectra (a) and N_2 adsorption–desorption isotherms (b) of CoMn-LDH and CoFe-LDH. XPS spectrum of CoMn-LDH; (c) survey spectra; Co 2p (d) and Mn 2p (e); XPS spectrum of CoFe-LDH; (f) survey spectra; Co 2p (g) and Fe 2p (h).

Table 2 | The BET specific surface area of CoMn-LDH and CoFe-LDH derived from MOFs and by other traditional methods

Samples	Specific surface area (m²/g)	References
MOF-derived CoMn-LDH	43.2	(This work)
MOF-derived CoFe-LDH	169.9	(This work)
CoMn-LDH	41.6	Zhang et al. (2021)
Zn-Co-LDHs	4.9	Jiehu et al. (2020)
Ni/Fe-LDH (3:1)	20.1	Sun et al. (2018)
$Ni_{50}Co_{50}$-LDH	48	Soltani et al. (2021)
Mn_4Al_1-500	23.4	Wu et al. (2019)
Mg-Fe-OH-LDH	42.8	Cao et al. (2020b)

3.2. Catalytic performance

The following section describes the 2,4-DCP degradation via PMS activated by CoMn-LDH and CoFe-LDH catalysts under different conditions. In order to ensure the accuracy of the experimental results, each experiment was tested three times without special requirements and the average value has been taken.

After mixing CoMn-LDH and CoFe-LDH catalysts and 2,4-DCP solution, the 2,4-DCP concentration in the adsorption process was monitored. It could noted from Figure 4(a) that the adsorption equilibrium was reached within 15 minutes, and the
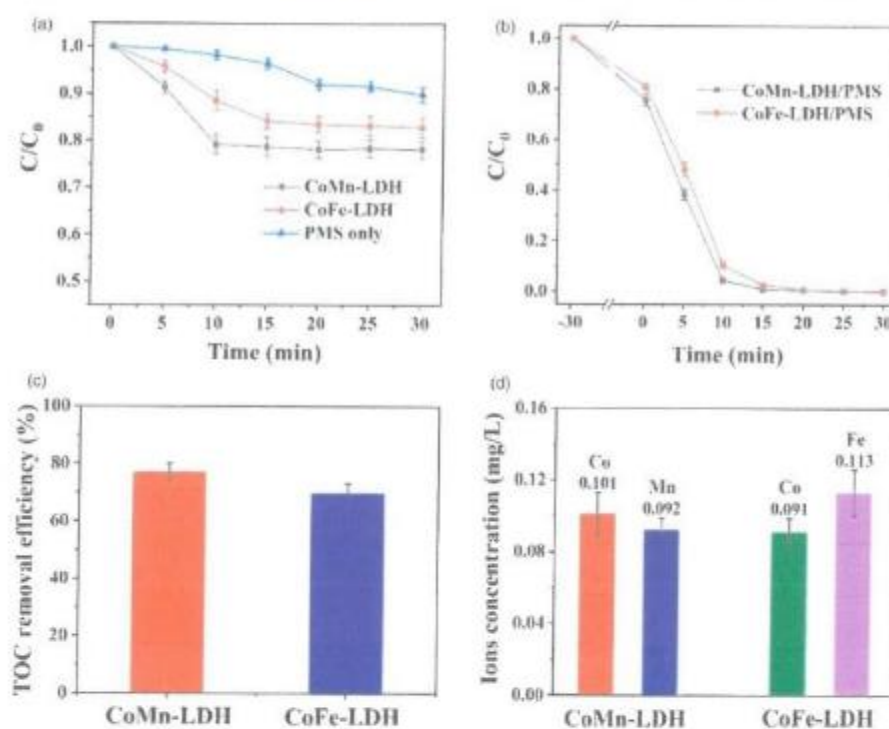
Figure 4 | Adsorption–desorption balance of CoMn-LDH and CoFe-LDH (a); catalytic degradation of 2,4-DCP using different catalysts (b); TOC removal of 2,4-DCP of CoMn-LDH and CoFe-LDH (c); The concentration of cobalt ions, manganese ions and iron ions in solution (d). The diagram is the average value of the triplicate and the error bars represent SD. Reaction conditions: [2,4-DCP]₀ = 20 mg/L, [PMS]₀ = 0.2 g/L, [catalyst]₀ = 0.2 g/L, pH₀ = 6.5 and T₀ = 25 °C.

adsorption rates of 2,4-DCP by CoMn-LDH and CoFe-LDH were stable at 24.2% and 19.1%, respectively. In order to eliminate the interference of adsorption on the catalytic performance, the mixture of LDH catalysts and 2,4-DCP solution were stirred for 30 minutes before PMS addition. In addition, only 10.2% of 2,4-DCP was degraded by PMS self-activation without addition of LDH catalysts, which indicated that PMS had a weak self-activation ability to degrade pollutants.

The ability of CoMn-LDH and CoFe-LDH to adsorb dyes was weak in the absence of PMS, so catalyst adsorption effect can be excluded. In Figure 4(b), after PMS and catalyst were added simultaneously, 2,4-DCP degradation reached 95.4% and 89.4% within 10 minutes and reached 99.3% and 99.2% within 20 minutes by CoMn-LDH and CoFe-LDH catalysts, respectively. The results showed that CoMn-LDH and CoFe-LDH exhibited excellent performance to activate PMS for 2,4-DCP degradation. In addition, MOF-derived LDHs were more prominent in terms of pollutant removal rate compared with other LDH catalysts (Table 3).

In order to study the mineralization degree of the reaction, the TOC of the 2,4-DCP solution was detected after 30 minutes of reaction. The removal rate of TOC reached 77.1% and 69.6% in systems of CoMn-LDH/PMS and CoFe-LDH/PMS, respectively (Figure 4(c)). The results indicated that the PMS activated by LDH catalysts had high removal rates of TOC, and 2,4-DCP was degraded into small molecules and then mineralized.

During the degradation reaction, transition metals in LDH catalysts may enter the solution in the form of ions. In order to determine the degree of loss of metal ions during the catalysis process and the influence of the homogeneous catalysis of metal ions on the experimental results, the concentrations of Co ions, Mn ions and Fe ions in the reaction system were determined by ICP-MS. As shown in Figure 4(d), only 0.10 mg/L of Co ions and 0.092 mg/L Mn ions were detected in the CoMn-LDH/PMS system after 30 minutes of reaction and only 0.091 mg/L Co ions and 0.11 mg/L Fe ions were detected in the CoFe-LDH catalytic system. Such a low metal ion concentration had a negligible effect on the catalytic activity. The results proved that the MOF-derived LDH catalysts with stable structure and excellent performance were successfully synthesized.

3.3. Influence of 2,4-DCP degradation parameters

In order to further research PMS activation performance of CoMn-LDH and CoFe-LDH, a series of 2,4-DCP degradation experiments was carried out under different conditions (PMS concentration, catalyst dose, reaction temperature). 2, 4-DCP degradation by CoMn-LDH/PMS and CoFe-LDH/PMS at different PMS concentrations is shown in Figure 5(a) and 5(b). As the PMS concentration increased from 0.1 g/L to 0.2 g/L (catalyst concentration: 0.2 g/L), the removal rate of 2,4-DCP increased gradually. However, when the PMS concentration was further increased to 0.4 g/L, no significant improvement in 2,4-DCP degradation was observed. It can be concluded that at the PMS concentration of 0.2 g/L, LDHs achieved the highest catalytic efficiency. Too high PMS concentration would produce excess reaction species, which may undergo a self-scavenging reaction, resulting in no significant improvement for 2,4-DCP degradation (Oh et al. 2016). As shown in Equations (1) and (2):

$$HSO_5^- + SO_4^{\bullet-} \rightarrow HSO_4^- + SO_5^{\bullet-} \tag{1}$$

$$SO_4^{\bullet-} + SO_4^{\bullet-} \rightarrow S_2O_8^{2-} \tag{2}$$

The amount of catalyst could determine the number of active sites for PMS activation. Figure 5(c) and 5(d) shows the effect of catalyst concentration on the PMS activation to degrade 2,4-DCP. After addition of the catalyst, the removal rate of 2,4-

Table 3 | The PMS activation performance by MOF-derived CoMn-LDH and MOF-derived CoFe-LDH and other LDH catalysts

| Catalyst	Catalyst dosage	PMS concern.	Organic pollutant	Removal efficiency	Ref.
MOF-derived CoMn-LDH	0.2 g/L	0.2 g/L	2,4-DCP (20 mg/L)	99.3% (20 min)	This work
MOF-derived CoFe-LDH	0.2 g/L	0.2 g/L	2,4-DCP (20 mg/L)	89.2% (10 min)	This work
AlCo-LDH	0.2 g/L	0.4 g/L	TC (30 mg/L)	49.1% (30 min)	Cao et al. (2020a)
DOM-LDH	0.2 g/L	0.2 g/L	BPA (20 mg/L)	93% (60 min)	Ye et al. (2020)
Fe-Mn-LDH	0.4 g/L	0.4 g/L	ODA (10 mg/L)	85.5% (5 min)	Chen et al. (2019)
AC@CoFe-LDH	0.2 g/L	1.0 g/L	LMF (5 mg/L)	92.0% (60 min)	Ma et al. (2020)
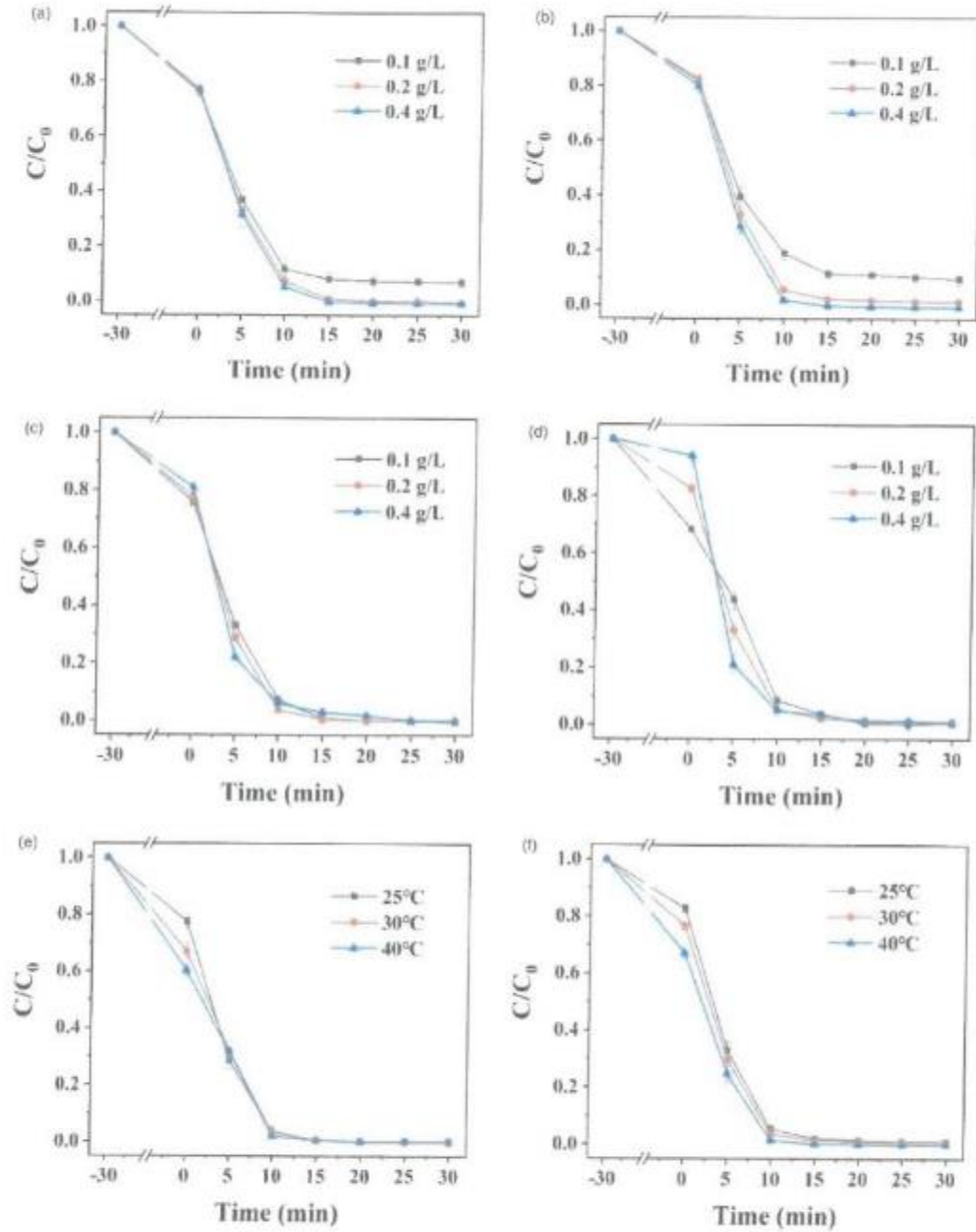
Figure 5 | Catalytic degradation of 2,4-DCP under different conditions. PMS dosage (a, b), catalyst dosage (c, d), temperature (e, f) of CoMn-LDH and CoFe-LDH, respectively. The diagram is the average value of triplicates and the error bars represent SD. Reaction conditions: [2,4-DCP]$_0$ = 20 mg/L, [PMS]$_0$ = 0.2 g/L, [catalyst]$_0$ = 0.2 g/L, pH$_0$ = 6.5 and T$_0$ = 25 °C.

106

DCP increased sequentially. When the amount of LDHs was increased from 0.1 g/L to 0.4 g/L (PMS concentration: 0.2 g/L), 2,4-DCP degradation by CoMn-LDH and CoFe-LDH increased from 66.9% to 77.6% and 56.2% to 78.7%, respectively, within 5 minutes. In fact, more catalyst provided more active sites for PMS activation, thereby further promoting the degradation of 2,4-DCP. However, the amount of catalyst only increased the initial degradation rate, but did not significantly affect the final degradation of 2,4-DCP. The results showed 0.1 g/L catalyst could provide enough active sites to activate PMS for degrading 2,4-DCP.

It can be seen from Figure 6(e) and 6(f) that when CoMn-LDH and CoFe-LDH were used as catalysts, increasing the reaction temperature can increase the degradation rate of 2,4-DCP. In the first 10 minutes, the increase of the reaction temperature had a more obvious increase in the degradation rate, because the PMS activation is an endothermic reaction. However, after 10 minutes, the degradation rate at different temperatures tended to be the same, indicating that the temperature was not the rate determining step of the catalytic reaction.

3.4. Degradation test of multiple pollutants

In order to further broaden the actual application value of MOF-derived LDHs, degradation tests of bisphenol A (BPA), ciprofloxacin (CIP) and 2,4-D were carried out. In the CoMn-LDH/PMS system, the degradation rates of BPA, CIP and 2,4-D reached 92.7%, 77.7% and 73.1% after 15 minutes of reaction, and 98.4%, 94.5% and 93.9% within 30 minutes, respectively. It can be seen that the pollutants have been basically removed. In CoFe-LDH/PMS system, the degradation rates of BPA, CIP and 2,4-D reached 96.8%, 93.7% and 92.3%, respectively, within 30 minutes. The above results indicated that MOF-derived LDHs manifested excellent catalytic performance for different organic pollutants, indicating that LDHs showed great potential in environmental fields.

3.5. Stability and reusability of LDHs

The reusability of the catalyst is one of the important factors to measure the stability and activity of the catalyst. Under the same reaction conditions, repeated experiments were set up to investigate the reusability of CoMn-LDH and CoFe-LDH catalysts. As shown in Figure 7(a) and 7(b), after three cycles, 2,4-DCP degradation by CoMn-LDH and CoFe-LDH was still as high as 99.5% and 97.2%, respectively. The results showed that the MOF-derived CoMn-LDH and CoFe-LDH catalysts exhibited extremely high activity, stability and practical application value.

3.6. Identification of reaction species and possible mechanism

MOF-derived CoMn-LDH and CoFe-LDH catalysts showed excellent catalytic performance for PMS activation to degrade 2,4-DCP and multiple pollutants. It is particularly important to understand the PMS activation mechanism by LDH catalysts. PMS can generate sulfate radical ($SO_4^{\bullet-}$), and can also react with H_2O or OH^- to generate hydroxyl radicals ($^{\bullet}OH$) (Equations (3) and (4)), which can also degrade 2,4-DCP. Furthermore, during the PMS activation process, singlet oxygen ($^1O_2$) and superoxide radicals ($O_2^{\bullet-}$) may be generated to degrade 2,4-DCP. In order to determine which kind of reaction
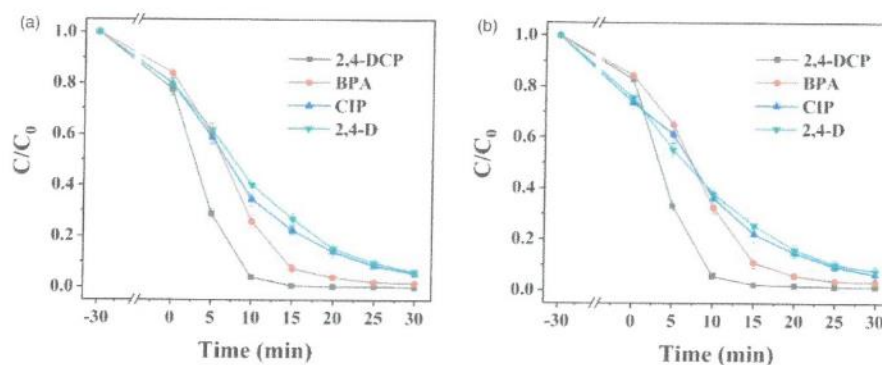

Figure 6 | The degradation of different pollutants by CoMn-LDH (a) and CoFe-LDH (b). The diagram is the average value of the triplicate and the error bars represent SD. Reaction conditions: [pollutants]$_0$ = 20 mg/L, [PMS]$_0$ = 0.2 g/L, [catalyst]$_0$ = 0.2 g/L, pH$_0$ = 6.5 and T$_0$ = 25 °C.
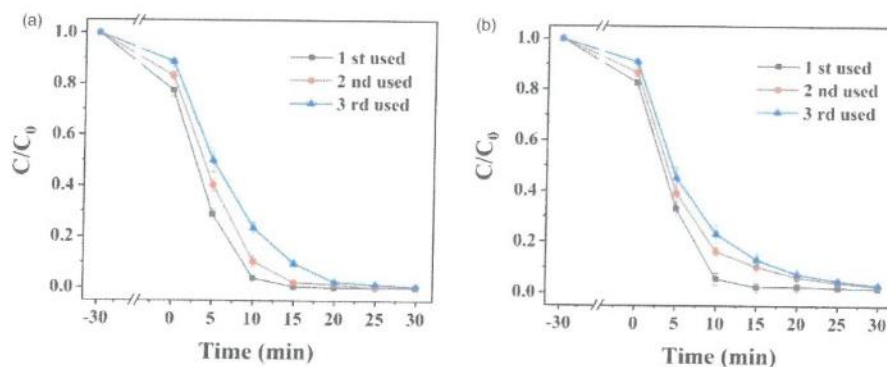
107

Figure 7 | Stability and reusability of CoMn-LDH (a) and CoFe-LDH (b) catalysts to activate PMS for 2,4-DCP degradation. The diagram is the average value of the triplicate and the error bars represent SD. Reaction conditions: $[2,4\text{-DCP}]_0 = 20$ mg/L, $[PMS]_0 = 0.2$ g/L, $[catalyst]_0 = 0.2$ g/L, $pH_0 = 6.5$ and $T_0 = 25$ °C.

species generated in the PMS/LDH system, active reaction species quenching experiments were carried out. TBA, ethanol, L-Histidine and p-benzoquinone were used as alternative active species scavengers to detect the existence of $^\bullet OH$, $SO_4^{\bullet-}$, $^1O_2$ and $O_2^{\bullet-}$. Ethanol can fast react with $^\bullet OH$ and $SO_4^{\bullet-}$ to quench free radicals. TBA can react quickly with $^\bullet OH$ radical, but hardly reacts with $SO_4^{\bullet-}$. In addition, the generated singlet oxygen ($^1O_2$) and superoxide radicals ($O_2^{\bullet-}$) can be scavenged by l-histidine and p-benzoquinone:

$$SO_4^{\bullet-} + H_2O \rightarrow SO_4^{2-} + {}^\bullet OH + H^+ \tag{3}$$

$$SO_4^{\bullet-} + OH^- \rightarrow SO_4^{2-} + {}^\bullet OH \tag{4}$$

As shown in Figure 8(a) and 8(b), addition of ethanol and l-histidine significantly reduced 2,4-DCP degradation by the CoMn-LDH/PMS system and the CoFe-LDH/PMS system, while the system with TBA and p-benzoquinone had relatively small reduction in the removal rate of pollutants. In the system with CoMn-LDH as the catalyst, after adding 10 mM TBA, 10 mM ethanol, 10 mM l-histidine and 10 mM p-benzoquinone, the removal rate of 2,4-DCP dropped from 99.9% to 99.1%, 40.2%, 15.9% and 92.5% within 30 minutes, respectively. At the same time, in the system with CoFe-LDH as the catalyst, the removal rate of 2,4-DCP declined from 99.1% to 97.9%, 42.9%, 34.0% and 94.6% within 30 minutes, correspondingly. In the CoMn-LDH/PMS system and the CoFe-LDH/PMS system with addition TBA and p-benzoquinone, 2,4-DCP was almost completely degraded within 30 minutes, but the degradation rate decreased significantly. It can be clearly seen that the inhibitory effect of l-histidine and ethanol on 2,4-DCP removal was significantly greater than TBA and p-benzoquinone, and the inhibitory effect of l-histidine on 2,4-DCP degradation was most obvious. Therefore, it can be concluded that $^\bullet HO$, $SO_4^{\bullet-}$, $^1O_2$ and $O_2^{\bullet-}$ also can be generated by the activation of LDH catalysts, but non-radical pathways ($^1O_2$) and free radical pathways ($SO_4^{\bullet-}$) played significant roles in 2,4-DCP degradation.

In order to further demonstrate the types of reaction species involved in the degradation reaction, electron paramagnetic resonance experiments were performed using spin-trapping agents DMPO and TEMP, which are shown in Figure 8(c)–8(f). When only 2,4-DCP and PMS were added to the system, no signal was observed using TEMP and DMPO, which indicated that reaction species can only be produced in large quantities after catalyst activation. TEMP can be used as trapping agents for detecting $^1O_2$ (Luo *et al.* 2020). When CoMn-LDH and CoFe-LDH were added to the system with TEMP as the trapping agent, a representative signal with a signal intensity ratio of 1:1:1 was detected (Figure 8(c) and 8(d)), which showed that the PMS was activated and produced a large amount of $^1O_2$. In the system with DMPO as the trapping agent, when CoMn-LDH and CoFe-LDH were added, a weak signal was detected in the CoMn-LDH system and no reaction species signal was detected in the reaction with CoFe-LDH as catalyst (Figure 8(e) and 8(f)). According to the above results, both $SO_4^{\bullet-}$ and
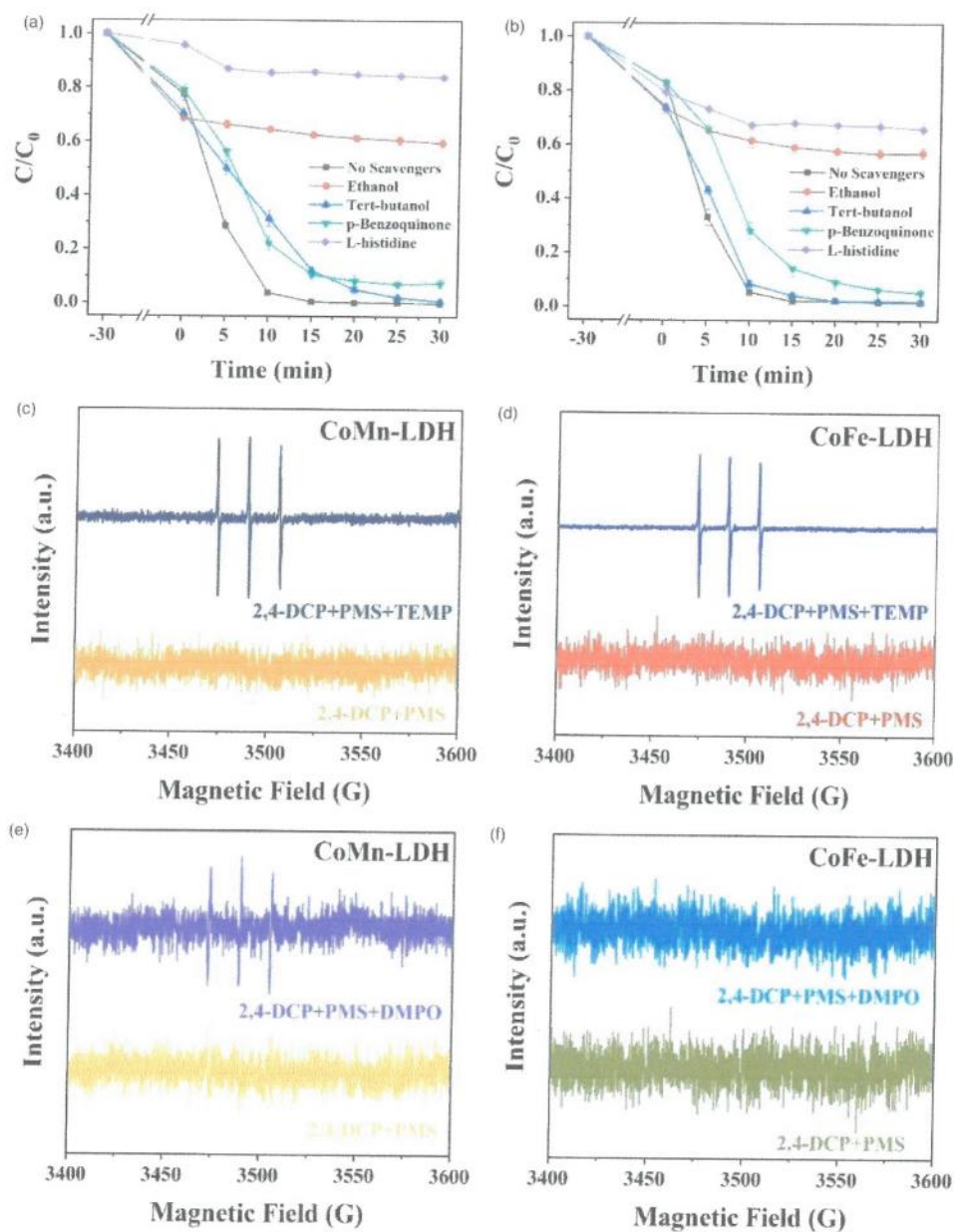
Figure 8 | Scavenger quenching on 2,4-DCP degradation by ethanol, tert-butyl alcohol l-histidine, p-benzoquinone of CoMn-LDH (a) and CoFe-LDH (b); EPR spectra of CoMn-LDH catalyst in TEMP solutions (c) and in DMPO solutions (d); EPR spectra of CoFe-LDH catalyst in TEMP solutions (e) and in DMPO solutions (f). The diagram is the average value of the triplicates and the error bars represent SD. Reaction conditions: $[2,4\text{-DCP}]_0 = 20$ mg/L, $[PMS]_0 = 0.2$ g/L, $[catalyst]_0 = 0.2$ g/L, $pH_0 = 6.5$ and $T_0 = 25$ °C.

$^1O_2$ participated and played more important roles in the PMS activation reaction, which was consistent with the results shown in Figure 8(a) and 8(b).

In order to explain the production of $^1O_2$ and the reason why $SO_4^{\bullet-}$ were only detected in small amounts, the production pathway of $SO_4^{\bullet-}$ and $^1O_2$ was further studied. Under normal circumstances, $^1O_2$ can be slowly generated by the self-decomposition of PMS, but the production of $^1O_2$ can be significantly promoted in the presence of carbon-based PMS activation catalysts. The C–O bond, as sp2 carbon electron-rich oxides, was identified as the active sites for PMS activation to generate non-radical reaction species (Li et al. 2020b). In addition, the presence of N atoms in CoMn-LDH and CoFe-LDH catalysts can attract the electrons of surrounding C atoms, and the positively charged C can increase the production of $^1O_2$ (Du et al. 2021). In addition, the electron-rich N group can also provide the electrons to break the O–O bond of PMS to generate $^1O_2$.

Based on the above research results, a possible reaction mechanism for the catalytic activation of PMS by MOF-derived LDH was proposed. The activation of PMS was mainly completed by the non-radical ($^1O_2$) pathway and the free radical ($SO_4^{\bullet-}$) pathway (Geng et al. 2021). For CoFe-LDH system, PMS reacted with Co^{2+} to generate sulfate radicals ($SO_4^{\bullet-}$) and hydroxyl radicals ($^\bullet HO$), accompanied by one electron loss of Co^{2+} to form Co^{3+} (Equation (5)). Fe^{2+} also lost an electron and reacted with PMS to generated $SO_4^{\bullet-}$ and $^\bullet HO$ (Equation (7)). The transformation between Co^{2+} and Co^{3+} can be realized through Equations (5) and (6) and $SO_5^{\bullet-}$ can be formed at the same time. Then under the conditions of MOF-derived LDH, large amounts of HSO_5^- and $SO_5^{\bullet-}$ were converted to $^1O_2$ (Equation (8)). Therefore, because large amounts of $SO_4^{\bullet-}$ were converted into non-radical species $^1O_2$ through the above-mentioned pathways, the number of $SO_4^{\bullet-}$ radicals decreased which made it more difficult to detect. Finally, non-radicals ($^1O_2$) and free radicals ($SO_4^{\bullet-}$) attack the chemical bonds of 2, 4-DCP to form small molecules or other intermediates, which were further mineralized into CO_2, H_2O or Cl^- (Equation (9)). According to the standard reduction potentials of metals (Equations (10)–(12)), it can be considered that the redox between Co^{2+} and Fe^{3+} is thermodynamically favorable (Su et al. 2013):

$$Co^{2+} + HSO_5^- \rightarrow Co^{3+} + SO_4^{\bullet-} + OH^- \tag{5}$$

$$Co^{3+} + HSO_5^- \rightarrow Co^{2+} + SO_5^{\bullet-} + H^+ \tag{6}$$

$$Fe^{2+} + HSO_5^- \rightarrow Fe^{3+} + SO_4^{\bullet-} + OH^- \tag{7}$$

$$HSO_5^- + SO_5^{\bullet-} \rightarrow SO_4^{\bullet-} + H^+ + {}^1O_2 \tag{8}$$

$$SO_4^{\bullet-}/{}^1O_2 + 2,4\text{-}DCP \rightarrow [\text{intermediates}] \rightarrow CO_2 + H_2O + Cl^- \tag{9}$$

$$Fe^{3+} + e^- \rightarrow Fe^{2+}, E^0 = 0.77\ V \tag{10}$$

$$Co^{2+} + e^- \rightarrow Co^{3+}, E^0 = 1.83\ V \tag{11}$$

$$Fe^{3+} + Co^{2+} \rightarrow Fe^{2+} + Co^{3+}, E^0 = 1.04\ V \tag{12}$$
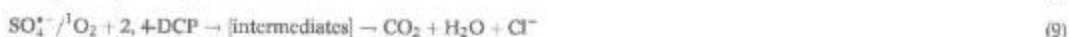
3.7. Phytotoxicity assessment

2,4-D is a chlorophenoxy herbicide (CPHs), which is widely used to control the growth of various broad-leaved weeds. In order to study the toxicity of 2,4-D and its degradation intermediates, mung bean seeds were cultured in degraded 2,4-D solution for 7 days by measuring its germination rate and radicle length. It can be seen from Figure 9(a) that the germination rate of mung bean seeds cultured in pure water exceeded 90% within 2 days, and the germination rate of mung in degraded 2,4-D solution by CoMn-LDH and CoFe-LDH decreased slightly. However, undegraded 2,4-D had a significant inhibitory effect on the germination rate of mung. Furthermore, as shown in Figures 9(b), 10 and 11, the average radicle length of mung bean seeds germinated in pure water, degraded 2,4-D solution (CoMn-LDH), degraded 2,4-D solution (CoMn-LDH) and undegraded 2,4-D solution were 10.5 cm, 7.4 cm, 7.0 cm and 1.1 cm. After degradation via PMS activation by LDH catalysts, the toxicity of the 2,4-D solution decreased greatly, but it still had certain inhibitory effects on the germination of mung bean, which may be due to the leakage of a small parts of metal ions or the degradation of 2,4-D intermediates affecting the growth of radicles (Kumar et al. 2021).

Figure 9 | The germination rate (a) and average radicle length (b) of mung beans cultivated in degraded 2,4-D solution by CoMn-LDH, degraded 2,4-D solution by CoFe-LDH, undegraded 2,4-D solution and ultrapure water. The diagram is the average value of the triplicate and the error bars represent SD.

Figure 10 | Phytotoxicity assessment of mung beans cultivated in degraded 2,4-D solution by CoMn-LDH, degraded 2,4-D solution by CoFe-LDH, undegraded 2,4-D solution and ultrapure water.

4. CONCLUSIONS

In this work, MOF-derived CoMn-LDH and CoFe-LDH catalysts with high activity and high specific surface area were successfully prepared through the pseudomorphic transformation process under alkaline conditions. SEM and TEM manifested that the two LDH catalysts have a stable layered structure, and the morphology basically did not change even after use. BET results showed that two LDHs have well developed porous structures and high specific surface area, which could provide more active sites to activate PMS. As a result, the two LDH samples demonstrated high catalytic performance to activate PMS for the degradation of 2,4-DCP and other organic pollutants. 2,4-DCP degradation by CoMn-LDH/PMS system and
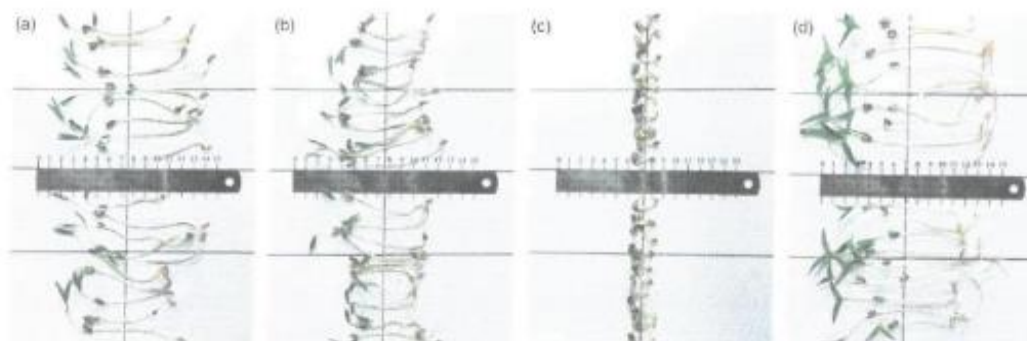
Figure 11 | The average radicle length of mung bean cultivated in degraded 2,4-D solution by CoMn-LDH (a), degraded 2,4-D solution by CoFe-LDH (b), undegraded 2,4-D solution (c) and ultrapure water (d).

CoFe-LDH/PMS system reached 99.3% and 99.2% within 20 minutes, respectively. The moderate increase in PMS concentration, catalyst dosage and reaction temperature all have a positive effect on the degradation of 2,4-DCP. After three cycles, CoMn-LDH and CoFe-LDH catalysts could still obtain 2,4-DCP degradation of 99.5% and 97.2%, indicating that MOF-derived LDH catalysts are stable and excellent candidates for PMS activation. In addition, these two LDH catalysts also showed excellent catalytic performance for the degradation of other different types of pollutants, such as BPA, CIP, 2,4-D. The high activity of the two LDH catalysts was attributed to the large specific surface area, hierarchical structure, and redox reaction. The scavenger experiments and EPR results showed that $^1O_2$ and $SO_4^{\cdot-}$ were the main active substance in 2,4-DCP degradation. In addition, phytotoxicity assessment of mung beans confirmed the significant enhancement in mineralization degree and reduction toxicity of the degraded 2,4-D solution by two LDH catalysts. In summary, this research provided a facile method to design transition metal-based LDH samples and expands the scope of MOF derivants for PMS activation in organic wastewater treatment.

ACKNOWLEDGEMENTS

DATA AVAILABILITY STATEMENT

All relevant data are included in the paper or its Supplementary Information.

REFERENCES

Ahsan, M. A., Imam, M. A., Puente Santiago, A. R., Rodriguez, A., Alvarado-Tenorio, B., Bernal, R., Luque, R. & Noveron, J. C. 2020a Spent tea leaves templated synthesis of highly active and durable cobalt-based trifunctional versatile electrocatalysts for hydrogen and oxygen evolution and oxygen reduction reactions. *Green Chemistry* 22 (20), 6967–6980.

Ahsan, M. A., Puente Santiago, A. R., Rodriguez, A., Maturano-Rojas, V., Alvarado-Tenorio, B., Bernal, R. & Noveron, J. C. 2020b Biomass-derived ultrathin carbon-shell coated iron nanoparticles as high-performance tri-functional HER, ORR and Fenton-like catalysts. *Journal of Cleaner Production* 275, 124141.

Ahsan, M. A., Santiago, A. R. P., Nair, A. N., Weller, J. M., Sanad, M. F., Valles-Rosales, D. J., Chan, C. K., Sreenivasan, S. & Noveron, J. C. 2020c Metal-Organic frameworks-derived multifunctional carbon nanocatalysts for catalytic peroxymonosulfate activation and electrochemical hydrogen generation. *Molecular Catalysis* 498, 111241.

Ahsan, M. A., Puente Santiago, A. R., Sanad, M. F., Mark Weller, J., Fernandez-Delgado, O., Barrera, L. A., Maturano-Rojas, V., Alvarado-Tenorio, B., Chan, C. K. & Noveron, J. C. 2021 Tissue paper-derived porous carbon encapsulated transition metal nanoparticles as advanced non-precious catalysts: Carbon-shell influence on the electrocatalytic behaviour. *Journal of Colloid and Interface Science* 581 (Pt B), 905–918.

Benselka-Hadj Abdelkader, N., Bentouami, A., Derriche, Z., Bettahar, N. & de Ménorval, L. C. 2011 Synthesis and characterization of Mg–Fe layer double hydroxides and its application on adsorption of Orange G from aqueous solution. *Chemical Engineering Journal* **169** (1–3), 231–238.

Biesinger, M. C., Payne, B. P., Grosvenor, A. P., Lau, L. W. M., Gerson, A. R. & Smart, R. S. C. 2011 Resolving surface chemical states in XPS analysis of first row transition metals, oxides and hydroxides: Cr, Mn, Fe, Co and Ni. *Applied Surface Science* **257** (7), 2717–2730.

Cao, J., Sun, S., Li, X., Yang, Z., Xiong, W., Wu, Y., Jia, M., Zhou, Y., Zhou, C. & Zhang, Y. 2020a Efficient charge transfer in aluminum-cobalt layered double hydroxide derived from Co-ZIF for enhanced catalytic degradation of tetracycline through peroxymonosulfate activation. *Chemical Engineering Journal* **382**, 122802.

Cao, Y., Guo, Q., Liang, M. & Sun, W. 2020b Sb(III) and Sb(V) removal from water by a hydroxyl-intercalated, mechanochemically synthesized Mg-Fe-LDH. *Applied Clay Science* **196**, 105766.

Chen, G., Nengzi, L. C., Li, B., Gao, Y., Zhu, G. & Cheng, X. 2019 Octadecylamine degradation through catalytic activation of peroxymonosulfate by FeMn layered double hydroxide. *Science of the Total Environment* **695**, 133963.

Daud, M., Kamal, M. S., Shehzad, F. & Al-Harthi, M. A. 2016 Graphene/layered double hydroxides nanocomposites: a review of recent progress in synthesis and applications. *Carbon* **104**, 241–252.

Du, N., Liu, Y., Li, Q., Miao, W., Wang, D. & Mao, S. 2021 Peroxydisulfate activation by atomically-dispersed Fe-Nx on N-doped carbon: mechanism of singlet oxygen evolution for nonradical degradation of aqueous contaminants. *Chemical Engineering Journal* **413**, 127545.

Geng, G., Cai, M., Fang, R., Luan, Q., Zhang, Z., Song, J. & Zhang, J. 2020 Metal-organic frameworks-derived perovskite catalysts for efficient degradation of 2,4-dichlorophenol via peroxymonosulfate activation. *Applied Surface Science* **534**, 147467.

Geng, G., Gao, Y., Zhang, Z., Gao, K., Zhang, W. & Song, J. 2021 Renewable and robust biomass waste-derived Co-doped carbon aerogels for PMS activation: catalytic mechanisms and phytotoxicity assessment. *Ecotoxicology and Environment Safety* **220**, 112381.

He, S., Li, Z., Wang, J., Wen, P., Gao, J., Ma, L., Yang, Z. & Yang, S. 2016 MOF-derived Ni$_x$Co$_{1-x}$(OH)$_2$ composite microspheres for high performance supercapacitors. *RSC Advances* **6** (55), 49478–49486.

Hou, C., Liu, H. & Li, Y. 2021a The preparation of three-dimensional flower-like TiO$_2$/TiOF$_2$ photocatalyst and its efficient degradation of tetracycline hydrochloride. *RSC Advances* **11** (25), 14957–14969.

Hou, C., Liu, H. & Mohammad, F. B. 2021b Preparation of ordered mesoporous F-H$_2$Ti$_5$O$_7$ nanosheets using orthorhombic HTiOF$_3$ as a precursor and their highly efficient degradation of tetracycline hydrochloride under simulated sunlight. *Journal of Solid State Chemistry* **300**, 122288.

Hu, P. & Long, M. 2016 Cobalt-catalyzed sulfate radical-based advanced oxidation: a review on heterogeneous catalysts and applications. *Applied Catalysis B: Environmental* **181**, 103–117.

Huang, G. X., Wang, C. Y., Yang, C. W., Guo, P. C. & Yu, H. Q. 2017 Degradation of Bisphenol A by Peroxymonosulfate Catalytically Activated with Mn$_{1.8}$Fe$_{1.2}$O$_4$ Nanospheres: synergism between Mn and Fe. *Environmental Science and Technology* **51** (21), 12611–12618.

Huang, C., Nie, J., Xu, Z., Zhang, X., Tang, J., Wang, B., Huang, J., Du, C. & Chen, J. 2021 One-step hydrothermal synthesized 3D P-MoO$_3$/FeCo LDH heterostructure electrocatalysts on Ni foam for high-efficiency oxygen evolution electrocatalysis. *International Journal of Hydrogen Energy* **46** (24), 12992–13000.

Ji, F., Li, C., Liu, Y. & Liu, P. 2014 Heterogeneous activation of peroxymonosulfate by Cu/ZSM5 for decolorization of Rhodamine B. *Separation and Purification Technology* **135**, 1–6.

Jiehu, C., Chunlei, W., Ming, Z., Jie, Z., Li, F., Xiuhong, D., Leiming, C. & Chunguang, L. 2020 2D to 3D controllable synthesis of three Zn-Co-LDHs for rapid adsorption of MO by TEA-assisted hydrothermal method. *Applied Surface Science* **534**, 147564.

Jin, M., Lu, S.-Y., Ma, L., Gan, M.-Y., Lei, Y., Zhang, X.-L., Fu, G., Yang, P.-S. & Yan, M.-F. 2017 Different distribution of in-situ thin carbon layer in hollow cobalt sulfide nanocages and their application for supercapacitors. *Journal of Power Sources* **341**, 294–301.

Kumar, A., Prasad, B. & Garg, K. K. 2021 Enhanced catalytic activity of series LaCu$_x$Fe$_{1-x}$O$_3$ (x = 0.2, 0.4, 0.6, 0.8) perovskite-like catalyst for the treatment of highly toxic ABS resin wastewater: phytotoxicity study, parameter optimization and reaction pathways. *Process Safety and Environmental Protection* **147**, 162–180.

Lai, Q., Zhao, Y., Liang, Y., He, J. & Chen, J. 2016 In situ confinement pyrolysis transformation of ZIF-8 to nitrogen-enriched meso-microporous carbon frameworks for oxygen reduction. *Advanced Functional Materials* **26** (45), 8334–8344.

Li, G.-C., Liu, M., Wu, M.-K., Liu, P.-F., Zhou, Z., Zhu, S.-R., Liu, R. & Han, L. 2016 MOF-derived self-sacrificing route to hollow NiS$_2$/ZnS nanospheres for high performance supercapacitors. *RSC Advances* **6** (105), 103517–103522.

Li, W., Li, Y., Zhang, D., Lan, Y. & Guo, J. 2020a CuO-Co$_3$O$_4$@CeO$_2$ as a heterogeneous catalyst for efficient degradation of 2,4-dichlorophenoxyacetic acid by peroxymonosulfate. *Journal of Hazardous Materials* **381**, 121209.

Li, Y., Li, J., Pan, Y., Xiong, Z., Yao, G., Xie, R. & Lai, B. 2020b Peroxymonosulfate activation on FeCo$_2$S$_4$ modified g-C$_3$N$_4$ (FeCo$_2$S$_4$-CN): mechanism of singlet oxygen evolution for nonradical efficient degradation of sulfamethoxazole. *Chemical Engineering Journal* **384**, 123361.

Li, M., Zhong, H., He, Z., Hu, L., Sun, W., Loganathan, P. & Xiong, D. 2021 Degradation of various thiol collectors in simulated and real mineral processing wastewater of sulfide ore in heterogeneous modified manganese slag/PMS system. *Chemical Engineering Journal* **413**.

Liu, G., Ma, J., Li, X. & Qin, Q. 2009 Adsorption of bisphenol A from aqueous solution onto activated carbons with different modification treatments. *Journal of Hazardous Materials* **164** (2–3), 1275–1280.

Liu, X., Zhou, Y., Zhang, J., Tang, L., Luo, L. & Zeng, G. 2017 Iron containing metal-organic frameworks: structure, synthesis, and applications in environmental remediation. *ACS Appl Mater Interfaces* **9** (24), 20255–20275.

Liu, M., Wang, L., Yu, X., Zhang, H., Zhang, H., Li, S. & Huang, F. 2022 Introducing oxygen vacancies for improving the electrochemical performance of Co_2S_4@NiCo-LDH nanotube arrays in flexible all-solid battery-capacitor hybrid supercapacitors. *Energy* **238**, 121761.

Luo, J., Bo, S., Qin, Y., An, Q., Xiao, Z. & Zhai, S. 2020 Transforming goat manure into surface-loaded cobalt/biochar as PMS activator for highly efficient ciprofloxacin degradation. *Chemical Engineering Journal* **395**, 125063.

Ma, R. Z., Liang, J. B., Takada, K. & Sasaki, T. 2011 Topochemical synthesis of Co-Fe layered double hydroxides at varied Fe/Co ratios: unique intercalation of triiodide and its profound effect. *Journal of the American Chemical Society* **133** (3), 613–620.

Ma, Q., Nengzi, L.-c., Li, B., Wang, Z., Liu, L. & Cheng, X. 2020 Heterogeneously catalyzed persulfate with activated carbon coated with CoFe layered double hydroxide (AC@CoFe-LDH) for the degradation of lomefloxacin. *Separation and Purification Technology* **235**, 116204.

Ma, Y., Gu, Y., Jiang, D., Mao, X. & Wang, D. 2021 Degradation of 2,4-DCP using persulfate and iron/E-carbon micro-electrolysis coupling system. *Journal of Hazardous Materials* **413**, 125381.

Mukherjee, A., Mullick, A., Moulik, S. & Roy, A. 2021 Oxidative degradation of emerging micropollutants induced by rotational hydrodynamic cavitating device: a case study with ciprofloxacin. *Journal of Environmental Chemical Engineering* **9** (4), 105652.

Nawaz, M., Khan, A. A., Hussain, A., Jang, J., Jung, H. Y. & Lee, D. S. 2020 Reduced graphene oxide-TiO_2/sodium alginate 3-dimensional structure aerogel for enhanced photocatalytic degradation of ibuprofen and sulfamethoxazole. *Chemosphere* **261**, 127702.

Oh, W.-D., Dong, Z. & Lim, T.-T. 2016 Generation of sulfate radical through heterogeneous catalysis for organic contaminants removal: current development, challenges and prospects. *Applied Catalysis B: Environmental* **194**, 169–201.

Olmez-Hanci, T., Arslan-Alaton, I. & Genc, B. 2013 Bisphenol A treatment by the hot persulfate process: oxidation products and acute toxicity. *Journal of Hazardous Materials* **263 Pt 2**, 283–290.

Pan, X., Yan, L., Qu, R. & Wang, Z. 2018 Degradation of the UV-filter benzophenone-3 in aqueous solution using persulfate activated by heat, metal ions and light. *Chemosphere* **196**, 95–104.

Peng, J., Zhang, C., Zhang, Y., Shao, S., Wang, P., Liu, G., Dong, H., Liu, D., Shi, J., Cao, Z., Liu, H. & Gao, S. 2020 Efficient removal of triclosan via peroxymonosulfate activated by a ppb level dosage of Co(II) in water: reaction kinetics, mechanisms and detoxification. *Ecotoxicology and Environment Safety* **198**, 110676.

Qin, Y., Ding, W. & Zhao, R. 2021 ZIF-8-derived ZnTi-LDHs with unique self-supported architecture and corresponding LDHs/rGO hybrid for gas sensor applications. *Chemical Physics Letters* **781**, 138965.

Shakeel, M., Arif, M., Yasin, G., Li, B. & Khan, H. D. 2019 Layered by layered Ni-Mn-LDH/g-C_3N_4 nanohybrid for multi-purpose photo/electrocatalysis: morphology controlled strategy for effective charge carriers separation. *Applied Catalysis B: Environmental* **242**, 485–498.

Shen, M., Li, W., Chen, L., Chen, Y., Ren, S. & Han, D. 2021 NiCo-LDH nanoflake arrays-supported Au nanoparticles on copper foam as a highly sensitive electrochemical non-enzymatic glucose sensor. *Analytica Chimica Acta* **1177**, 338787.

Soltani, R., Pelalak, R., Pishnamazi, M., Marjani, A., Sarkar, S. M., Albadarin, A. B. & Shirazian, S. 2021 Novel bimodal micro-mesoporous Ni_50Co_50-LDH/UiO-66-NH_2 nanocomposite for Tl(I) adsorption. *Arabian Journal of Chemistry* **14** (4), 103058.

Su, S., Guo, W., Leng, Y., Yi, C. & Ma, Z. 2013 Heterogeneous activation of oxone by $Co_xFe_{(1-x)}O_4$ nanocatalysts for degradation of rhodamine B. *Journal of Hazardous Materials* **244–245**, 736–742.

Sun, J., Li, Y., Chen, C., Qi, T., Xia, D., Mao, W., Yang, T., Chen, L., Shen, W. & Tang, S. 2018 Magnetic Ni/Fe layered double hydroxide nanosheets as enhancer for DNA hairpin sensitive detection of miRNA. *Talanta* **187**, 265–271.

Tian, N., Tian, X., Nie, Y., Yang, C., Zhou, Z. & Li, Y. 2019 Enhanced 2,4-dichlorophenol degradation at pH 3–11 by peroxymonosulfate via controlling the reactive oxygen species over Ce substituted 3D Mn_2O_3. *Chemical Engineering Journal* **355**, 448–456.

Wang, J. & Wang, S. 2018 Activation of persulfate (PS) and peroxymonosulfate (PMS) and application for the degradation of emerging contaminants. *Chemical Engineering Journal* **334**, 1502–1517.

Wang, F., Wang, W., Yuan, S., Wang, W. & Hu, Z.-H. 2017 Comparison of UV/H_2O_2 and UV/PS processes for the degradation of thiamphenicol in aqueous solution. *Journal of Photochemistry and Photobiology A: Chemistry* **348**, 79–88.

Wang, Y., Wang, L., Zhang, Y., Mao, X., Tan, W., Zhang, Y., Wang, X., Chang, M., Guo, R. & Xi, B. 2021 Perdisulfate-assisted advanced oxidation of 2,4-dichlorophenol by bio-inspired iron encapsulated biochar catalyst. *Journal of Colloid and Interface Science* **592**, 358–370.

Wang, Q., Xu, Z., Cao, Y., Chen, Y., Du, X., Yang, Y. & Wang, Z. 2022 Two-dimensional ultrathin perforated Co_3O_4 nanosheets enhanced PMS-Activated selective oxidation of organic micropollutants in environmental remediation. *Chemical Engineering Journal* **427**, 131953.

Wu, X., Feng, Y., Liu, X., Liu, L., Du, Y. & Li, Z. 2019 Redox & acidity optimizing of LDHs-based CoMnAl mixed oxides for enhancing NH_3-SCR performance. *Applied Surface Science* **495**, 143513.

Xiao, R., Luo, Z., Wei, Z., Luo, S., Spinney, R., Yang, W. & Dionysiou, D. D. 2018 Activation of peroxymonosulfate/persulfate by nanomaterials for sulfate radical-based advanced oxidation technologies. *Current Opinion in Chemical Engineering* **19**, 51–58.

Xiao, Z., Mei, Y., Yuan, S., Mei, H., Xu, B., Bao, Y., Fan, L., Kang, W., Dai, F., Wang, R., Wang, L., Hu, S., Sun, D. & Zhou, H. C. 2019 Controlled hydrolysis of metal-organic frameworks: hierarchical Ni/Co-layered double hydroxide microspheres for high-performance supercapacitors. *ACS Nano* **13** (6), 7024–7030.

Xie, M., Tang, J., Fang, G., Zhang, M., Kong, L., Zhu, F., Ma, L., Zhou, D. & Zhan, J. 2020 Biomass Schiff base polymer-derived N-doped porous carbon embedded with CoO nanodots for adsorption and catalytic degradation of chlorophenol by peroxymonosulfate. *Journal of Hazardous Materials* **384**, 121345.

Yaghi, O. M., Li, G. & Li, H. 1995 Selective binding and removal of guests in a microporous metal–organic framework. *Nature* **378** (6558), 703–706.

Yang, Q., Choi, H., Al-Abed, S. R. & Dionysiou, D. D. 2009 Iron–cobalt mixed oxide nanocatalysts: heterogeneous peroxymonosulfate activation, cobalt leaching, and ferromagnetic properties for environmental applications. *Applied Catalysis B: Environmental* **88** (3–4), 462–469.

Yang, Z., Li, X., Huang, Y., Chen, Y., Wang, A., Wang, Y., Li, C., Hu, Z. & Yan, K. 2021a Facile synthesis of cobalt-iron layered double hydroxides nanosheets for direct activation of peroxymonosulfate (PMS) during degradation of fluoroquinolones antibiotics. *Journal of Cleaner Production* **310**, 127584.

Yang, Z., Yan, X., Tang, Z., Peng, W., Zhang, J., Tong, Y., Li, J. & Zhang, J. 2021b Facile synthesis of hemin-based Fe-N-C catalyst by MgAl-LDH confinement effect for oxygen reduction reaction. *Applied Surface Science* **573**, 151505.

Ye, Q., Wu, J., Wu, P., Wang, J., Niu, W., Yang, S., Chen, M., Rehman, S. & Zhu, N. 2020 Enhancing peroxymonosulfate activation of Fe-Al layered double hydroxide by dissolved organic matter: performance and mechanism. *Water Research* **185**, 116246.

Yin, X., Ma, X., He, Y., Li, H., Fan, Y., He, T., Guo, X. & Chen, L. 2021 Robust self-cleaning urchin-like Ni/Co LDH stainless steel mesh for gravity-driven oil/water emulsion separation and catalytic degradation of aromatic dyes. *Colloids and Surfaces A: Physicochemical and Engineering Aspects* **627**, 127186.

Yu, D., Wu, B., Ge, L., Wu, L., Wang, H. & Xu, T. 2016 Decorating nanoporous ZIF-67-derived NiCo$_2$O$_4$ shells on a Co$_3$O$_4$ nanowire array core for battery-type electrodes with enhanced energy storage performance. *Journal of Materials Chemistry A* **4** (28), 10878–10884.

Yu, X., Cabooter, D. & Dewil, R. 2018 Effects of process variables and kinetics on the degradation of 2,4-dichlorophenol using advanced reduction processes (ARP). *Journal of Hazardous Materials* **357**, 81–88.

Yuan, J., Liu, Q., Li, S., Lu, Y., Jin, S., Li, K., Chen, H. & Zhang, H. 2017 Metal organic framework (MOF)-derived carbonaceous Co$_3$O$_4$/Co microframes anchored on RGO with enhanced electromagnetic wave absorption performances. *Synthetic Metals* **228**, 32–40.

Yusuf, S., Dinari, M. & Moheb, A. 2021 Facial synthesis of V-containing CuMgAl-LDHs as a new catalyst for the phenol hydroxylation. *Chemical Physics* **546**, 111183.

Zhang, P., Sun, F., Xiang, Z., Shen, Z., Yun, J. & Cao, D. 2014 ZIF-derived in situ nitrogen-doped porous carbons as efficient metal-free electrocatalysts for oxygen reduction reaction. *Energy & Environmental Science* **7** (1), 442–450.

Zhang, B., Qi, Z., Wu, Z., Lui, Y. H., Kim, T.-H., Tang, X., Zhou, L., Huang, W. & Hu, S. 2018 Defect-rich 2D material networks for advanced oxygen evolution catalysts. *ACS Energy Letters* **4** (1), 328–336.

Zhang, G., Xing, J., Zhao, Y. & Yang, F. 2021 Hierarchical N,P co-doped graphene aerogels framework assembling vertically grown CoMn-LDH nanosheets as efficient bifunctional electrocatalyst for rechargeable zinc-air battery. *Journal of Colloid and Interface Science* **590**, 476–486.

115